

(NASA-CR-176471) DEVELOPMENT OF THE
VARIATIONAL SEASAT DATA ANALYSIS TECHNIQUE
Final Report (Oklahoma Univ.) 80 p
HC A05/MF A01

N86-16697

CSCI 05B

Unclas
G3/43 05247

National Aeronautics and Space Administration
Goddard Space Flight Center

FINAL REPORT

Research Grant No. NAG 5-289

Development of the Variational SEASAT Data Analysis Technique

submitted by

Dr. Yoshi K. Sasaki
Director, Cooperative Institute for Mesoscale Meteorological Studies

and

Dr. Lang-Ping Chang
Research Scientist, Cooperative Institute for Mesoscale Meteorological Studies

and

Dr. James S. Goerss
Research Scientist, Cooperative Institute for Mesoscale Meteorological Studies

from

The University of Oklahoma
Office of Research Administration
1000 Asp Avenue, Room 314
Norman, OK 73019

December 1985



TABLE OF CONTENTS

	PAGE
I. Introduction.....	1
II. Retrieval of the Sea Surface Wind from the SEASAT-A Satellite Observations.....	2
III. Variational SEASAT Data Analysis Technique.....	5
a. Estimate of the surface geostrophic wind.....	6
b. Variational adjustment technique.....	8
IV. Results of Numerical Experiments.....	12
a. Determination of weights.....	12
b. Influence of the boundary condition.....	15
c. Effect of data density of surface pressure.....	17
d. Effect of quality of SEASAT-derived wind data.....	19
e. Influence of the surface temperature field.....	20
V. Concluding Remarks.....	21
Tables.....	23
Figure Captions.....	27
Figures.....	30
References.....	78

I. Introduction

Approximately 70% of earth's surface is covered by oceans. In terms of conventional meteorological observations, oceans are data-sparse areas. With the development of weather satellites in the 1960's, a vast amount of remotely sensed asynoptic data has since become available. Among various satellite weather data, the temperature soundings are of great potential use in determining the mass distribution of the entire atmosphere. In order to enter these satellite-derived temperature soundings into an atmospheric prediction system, one needs to obtain the geopotential height field for many different isobaric surfaces. The success of this task, however, crucially depends upon the quality of the sea-level pressure analysis. It thus follows that an improved sea-level pressure analysis in data-sparse areas over the oceans is vital for improved accuracy of the geopotential height information derived from the satellite soundings, which will in turn, result in a better representation of the entire mass field in an atmospheric prediction system. Since the surface wind is closely associated with the surface pressure gradient, insertion of satellite-derived surface wind into the conventional weather data is expected to considerably improve the sea-level pressure analysis in the data-sparse ocean areas. The variational SEASAT data analysis technique is specifically designed for this purpose.

Stated in a brief manner, the working principle of the SEASAT-A satellite sensing of the surface wind over the sea is as follows: The microwave radar scatterometer carried by the SEASAT-A satellite is very sensitive to the backscatter of the centimeter length ocean waves created by the action of the surface wind over the oceans. As a result, one can derive the vector wind over the sea surface by analyzing the backscatter of radar waves. Jones et al. (1982) compared the SEASAT-derived surface wind data with observations from the Joint Air Sea

Interaction Experiment (JASIN) and concluded that the satellite-derived sea surface wind has an accuracy of up to ± 2 m/s in speed and $\pm 20^\circ$ in direction. These numbers will be considered characteristic of the retrieved SEASAT wind field. By combining the densely spaced SEASAT-derived wind data with the sparsely distributed sea-level pressure observations via a variational adjustment technique subject to some appropriate physical constraint(s), an improvement in the sea-level pressure analysis is expected. Such an improvement will certainly be very helpful in upgrading the model forecasts of the atmospheric prediction systems in view of the large areal coverage of the earth's surface by the oceans.

In the following sections, we shall demonstrate how a simple marine boundary layer scheme in conjunction with a variational adjustment technique can be developed to help improve the sea-level pressure analysis by using the SEASAT-derived wind of a limited-area domain in the ocean.

II. Retrieval of the Sea Surface Wind from the SEASAT-A Satellite Observation

The SEASAT-A satellite was launched on June 28, 1978 by the National Aeronautics and Space Administration. It was the first satellite dedicated to establishing the usefulness of microwave sensors for remote sensing of the oceans. After just a little more than three months of operation, it failed to operate in its orbit due to a massive short circuit in its electrical power system. In spite of its short operational life, it was fortunate that enough data had been collected before its operation came to an end.

The most important microwave sensor the SEASAT-A satellite carried was a radar scatterometer for detecting the surface wind over the ocean. The physical basis of this lies in the sensitivity of the microwave radar backscatter to the centimeter length ocean waves created by the action of the surface wind. This is known as the Bragg scattering (Wright, 1966; Moore and Fung, 1979). The strength

of the radar backscattering cross section, σ^0 , is proportional to the capillary wave amplitude which is assumed to be in equilibrium with the wind friction speed u_* . The wind direction can be determined because the radar backscatter is anisotropic. Once the friction speed u_* is given, the wind at 19.5 m above the sea level under a neutral stability condition can be obtained. This wind is defined as the satellite-derived wind that would result if the atmosphere were neutrally stratified with a dry adiabatic lapse rate.

The history and details of the development of a geophysical algorithm to compute the 19.5 m neutral stability wind speed and direction from radar backscatter measurements are given by Jones et al. (1982). Three candidate algorithms were developed by researchers from the University of Kansas (Dome et al., 1977), the City University of New York (Pierson et al., 1974), and by the Remote Sensing System (Jones et al., 1978). A review of their work is given by Schroeder et al. (1982). The official wind vector algorithm known as SASS-I (SEASAT-A Satellite Scatterometer), described in Jones et al. (1982), represents a cooperative effort by the algorithm developers to incorporate the desirable features of its predecessors into a single algorithm.

The SASS-I model function is expressed by

$$F(\theta, x, \epsilon, w) = \log_{10} \sigma^0 = G(\theta, x, \epsilon) + H(\theta, x, \epsilon) \log_{10} w \quad (2.1)$$

where w is the windspeed. The values of functions G and H are tabulated for incidence angles θ from 0° to 70° , for relative azimuth angle x (antenna azimuth minus wind direction) from 0° to 180° , and for horizontal and vertical polarization, $\epsilon = H$ or V . This lookup table, called the SASS-I Table, is given by Schroeder et al. (1982).

Given the model function, estimates of the wind speed, W , and direction, α ,

are found which produce local minima for the following sum of squares:

$$S(W, \alpha) = \sum_{i=1}^N \{ \log_{10} \sigma_i^0 - F(\theta_i, x_i, \epsilon_i, W) \}^2 / \delta_i^2 \quad (2.2)$$

where

$$x_i = \phi_i - \alpha.$$

The sum is over the N observations in a data group. The instrument parameters σ_i^0 , θ_i , ϕ_i , and ϵ_i are the radar backscatter cross section, the incidence angle, the antenna azimuth angle, and the polarization for the i-th observation, respectively. The sum is weighted by $1/\delta_i^2$ where δ_i is the expected standard deviation between the σ^0 measurement and the model function. Unfortunately, the number of candidate wind vectors (called aliases) varies from two to four (with four being most common). One alias will correspond to the solution for the true wind vector, and the others will be false solutions. Given that the proper alias has been determined, Jones et al. (1982) reported that comparisons of SASS-derived winds with high quality withheld surface truth at the JASIN-SEASAT workshop show better agreement than the SASS specification $\pm 2\text{m/s}$ for wind speed and $\pm 20^\circ$ for wind direction. We will assume that the alias removal problem will have been eliminated or greatly reduced before the next instrument is launched, and that these figures are representative of the data quality one might expect from satellite-derived surface wind observations.

Using a large-scale marine planetary boundary layer model (Brown and Liu, 1982), Brown et al. (1982) calculated synoptic scale wind fields for comparison with surface data collected during JASIN and the Gulf of Alaska Experiment

(GOASEX). Synoptic scale pressure and temperature fields were input into the model in order to obtain the wind field. These analyses did not use satellite-derived wind observations. They found that the model-derived wind fields, when compared with the JASIN and GOASEX platform wind values, yielded a maximum error of $\pm 2\text{m/s}$ and $\pm 20^\circ$. This is only equal to the SASS specification accuracies. Brown and Liu (1982) reported that at mid-latitudes, a 1 mb error in 400 km grid pressures would contribute a 20% or 2m/s error to a 10m/s wind. The implication of this is that we may expect (at least in the higher latitudes) to obtain very accurate pressure gradient information from satellite-derived surface wind measurements.

III. Variational SEASAT Data Analysis Technique

In this section, we will discuss how the SEASAT-derived wind data can be utilized in a variational adjustment technique to help improve the sea-level pressure analysis.

On the average, the stability conditions for the marine boundary layer can be assumed to be nearly neutral (Gray, 1972). It is therefore reasonable to assume that the SEASAT-derived wind field well approximates the neutral stability vector wind at 19.5 m above sea level with an accuracy up to $\pm 2\text{m/s}$ in speed and $\pm 20^\circ$ in direction. Thus, it is expected that by using a simple marine planetary boundary layer scheme such as the geostrophic drag law, one may extract the surface pressure gradient information (equivalently but more conveniently the surface geostrophic wind) from the satellite-derived wind. After the surface geostrophic wind components have been estimated from the satellite wind, then together with the sparsely distributed observations of the surface pressure, a variational adjustment technique using as a weak constraint the geostrophic relation may yield the best estimate of the surface pressure and wind fields in the least squares

sense. In Section IIIa, we shall discuss the procedure of estimating the surface geostrophic wind from the SEASAT-derived wind. Details of the variational adjustment technique will be examined in Section IIIb.

IIIa. Estimate of the surface geostrophic wind

The SEASAT-derived wind can be regarded as an approximation to the wind at 19.5 m above sea level under a neutral stability stratification. Consequently, the simplest way to estimate the surface geostrophic wind from the SEASAT-derived wind field is perhaps to make use of the geostrophic drag law together with an empirically established relationship between the surface stress and the surface wind. The geostrophic drag law for the neutrally stratified atmospheric boundary layer is given by (Tennekes, 1973):

$$\frac{ku_g}{U_*} = \ln \frac{u_*}{fz_0} - B, \quad (3.1)$$

$$\frac{kv_g}{u_*} = -A. \quad (3.2)$$

In these equations, $A=5$ and $B=2$ (Blackadar and Tennekes, 1968), which are experimentally determined similarity constants; f is the Coriolis parameter; u_* is the frictional speed, z_0 is the roughness length; u_g and v_g are the components of the surface geostrophic wind respectively parallel and perpendicular to the direction of the surface stress (see Fig. 1); and k is the von Karman constant 0.35 (Businger et al., 1971).

By denoting the magnitude of the surface geostrophic wind as G and the angle between the surface stress and the surface geostrophic wind as α (see Fig. 1), (3.1) and (3.2) may be combined to give

$$\ln \frac{G}{fz_0} = B + \ln \frac{G}{U_*} + \left(\frac{k^2 G^2}{U_*^2} - A^2 \right)^{1/2}, \quad (3.3)$$

$$\sin \alpha = \frac{u_* A}{kG} \quad (3.4)$$

It is reasonable to use the well known logarithmic wind profile relation to describe the wind in the lowest say, 20 m of the atmospheric boundary layer:

$$k u_z = u_* \ln \frac{z}{z_0} \quad (3.5)$$

In order to close our marine boundary layer scheme, we shall make use of the following empirical formula for the neutral drag coefficient

$$C_{DN} \equiv \frac{u_*^2}{u_{10}^2} = 10^{-3} (0.75 + 0.067 u_{10}) \quad (3.6)$$

after Garratt (1977), where u_{10} is the wind speed in m/s at 10 m above the sea level.

Thus, with the help of (3.3) through (3.6), we may compute the vector surface geostrophic wind from any given satellite-derived wind (with speed $u_{19.5}$ in the direction of the surface stress). The zonal component of this wind will be denoted as u_s and the meridional component denoted as v_s in notation. Similarly, (3.3) through (3.6) can also be used to find the wind at 19.5 m above sea level if the vector surface geostrophic wind is given.

The purpose of the current study is to develop a useful variational technique to help determine more accurately the sea-level pressure field by making use of the SEASAT-derived wind data in data-sparse areas over the oceans. Consequently, in order to assess the accuracy of this variational adjustment technique, we follow the procedures given below to create assimilated SEASAT wind data:

- (i) For a given field of sea-level pressure of a selected target area over the sea, compute the associated geostrophic wind components.
- (ii) Compute the vector wind field at 19.5 m using (3.3) through (3.6).
- (iii) Add a normally distributed random error of zero mean and standard deviation 2 m/s to the wind speed and add another normally distributed random error of zero mean and standard deviation 20° to the wind direction of the vector wind resulted in (ii). This new wind field shall be regarded as the assimilated SEASAT-derived wind field.
- (iv) The assimilated SEASAT-derived wind at each grid point is converted to the surface geostrophic wind using (3.3) through (3.6). After the zonal and the meridional components of the surface geostrophic wind have been obtained, they will be employed in the variational adjustment procedure discussed in the next section.

IIIb. Variational adjustment technique

The variation adjustment of the SEASAT data starts with the minimization of the following functional

$$J \equiv \int_{\lambda_1}^{\lambda_2} \int_{\theta_1}^{\theta_2} \{ (u - u_s)^2 + (v - v_s)^2 + A (P - P_s)^2 + B \left[(fv - \frac{RT}{P} \frac{1}{a \cos \theta} \frac{\partial P}{\partial \lambda})^2 + (-fu - \frac{RT}{P} \frac{1}{a} \frac{\partial P}{\partial \theta})^2 \right] \} d\theta d\lambda, \quad (3.7)$$

where u_s and v_s represent the known surface geostrophic wind components derived from the assimilated SEASAT wind; P_s is the sparsely located surface (sea-level) pressure; a the earth's radius; λ the longitude; θ the latitude; A and B are the weights; and all the other variables carry their conventional meaning.

Essentially (3.7) means that we request the wind and pressure fields to be as close to the "observed" values as possible subject to the weak-form constraint of the geostrophic relation.

By letting the first variation of J vanish and by dropping the boundary integral terms arisen from application of integration by parts, the following three partial differential equations are yielded:

$$A(P-P_s) + \frac{1}{P} \frac{\partial}{\partial \lambda} \left[\frac{BRT}{a \cos \theta} \left(fv - \frac{RT}{a \cos \theta} \frac{\partial \ln P}{\partial \lambda} \right) \right] - \frac{1}{P} \frac{\partial}{\partial \theta} \left[\frac{BRT}{a} \left(fu + \frac{RT}{a} \frac{\partial \ln P}{\partial \theta} \right) \right] = 0 , \quad (3.8)$$

$$u - u_s + f \left(fu + \frac{RT}{a} \frac{\partial \ln P}{\partial \theta} \right) = 0 , \quad (3.9)$$

$$v - v_s + f \left(fv - \frac{RT}{a \cos \theta} \frac{\partial \ln P}{\partial \lambda} \right) = 0 . \quad (3.10)$$

Since we dropped the boundary terms in the above derivation, we have tacitly assumed that the geostrophic wind relation holds on the boundary when solving the P -equation.

In practice, Equations (3.8), (3.9) and (3.10) are solved in discretized form. The computational mesh used is a staggered one as shown schematically in Fig. 2. The outermost boundary grids are the pressure grids except for the four corners where additional velocity grids are present. The grid interval is taken to be 4° longitude and 4° latitude, the same grid resolution as the CIMMS Global model.

The finite-difference equations for (3.8), (3.9), and (3.10) are

$$\begin{aligned}
& A_{i,j} (P_{i,j} - P_{si,j}) + \frac{1}{P_{i,j}} \left\{ \frac{R f_{2i-1}}{\Delta \lambda a \cos \theta_{2i,j}} \left[\left(\frac{B_{i,j+1} + B_{i,j}}{2} \right) \left(\frac{T_{i,j+1} + T_{i,j}}{2} \right) \right. \right. \\
& \left. \left(\frac{v_{i-1,j} + v_{i,j}}{2} \right) - \left(\frac{B_{i,j} + B_{i,j-1}}{2} \right) \left(\frac{T_{i,j} + T_{i,j-1}}{2} \right) \left(\frac{v_{i-1,j} + v_{i,j-1}}{2} \right) \right] \\
& - \frac{R^2}{\Delta \lambda a^2 \cos^2 \theta_{2i-1}} \left[\frac{(B_{i,j+1} + B_{i,j})}{(P_{i,j+1} + P_{i,j+1})} \left(\frac{T_{i,j} + T_{i,j+1}}{2} \right)^2 \left(\frac{P_{i,j+1} - P_{i,j}}{\Delta \lambda} \right) \right. \\
& \left. - \frac{(B_{i,j} + B_{i,j-1})}{(P_{i,j} + P_{i,j-1})} \left(\frac{T_{i,j} + T_{i,j-1}}{2} \right)^2 \left(\frac{P_{i,j} - P_{i,j-1}}{\Delta \lambda} \right) \right] \left. \right\} - \frac{1}{P_{i,j}} \left\{ \frac{R}{\Delta \theta a} \right. \\
& \left[\left(\frac{B_{i-1,j} + B_{i,j}}{2} \right) \left(\frac{T_{i-1,j} + T_{i,j}}{2} \right) (f_{2i-2}) \left(\frac{u_{i-1,j} + u_{i-1,j-1}}{2} \right) \right. \\
& \left. - \left(\frac{B_{i,j} + B_{i+1,j}}{2} \right) \left(\frac{T_{i,j} + T_{i+1,j}}{2} \right) (f_{2i-1}) \left(\frac{u_{i,j} + u_{i,j-1}}{2} \right) \right] \\
& + \frac{R^2}{\Delta \theta a^2} \left[\frac{(B_{i-1,j} + B_{i,j})}{(P_{i-1,j} + P_{i,j})} \left(\frac{T_{i-1,j} + T_{i,j}}{2} \right)^2 \left(\frac{P_{i-1,j} - P_{i,j}}{\Delta \theta} \right) \right. \\
& \left. - \frac{(B_{i,j} + B_{i+1,j})}{(P_{i,j} + P_{i+1,j})} \left(\frac{T_{i,j} + T_{i+1,j}}{2} \right)^2 \left(\frac{P_{i,j} - P_{i+1,j}}{\Delta \theta} \right) \right] \left. \right\} = 0, \quad (3.11)
\end{aligned}$$

$$\begin{aligned}
& u_{i,j} - u_{si,j} + \left(\frac{B_{i,j} + B_{i,j+1} + B_{i+1,j} + B_{i+1,j+1}}{4} \right) (f_{2i}) [f_{2i} u_{i,j} \\
& + \frac{R}{a \Delta \theta} \left(\frac{T_{i,j} + T_{i,j+1} + T_{i+1,j} + T_{i+1,j+1}}{P_{i,j} + P_{i,j+1} + P_{i+1,j} + P_{i+1,j+1}} \right) \left(\frac{P_{i,j+1} + P_{i,j}}{2} - \frac{P_{i+1,j+1} + P_{i+1,j}}{2} \right)] = 0, \quad (3.12)
\end{aligned}$$

$$v_{i,j} - v_{s1,j} + \left(\frac{B_{i,j} + B_{i,j+1} + B_{i+1,j} + B_{i+1,j+1}}{4} \right) (f_{21}) [f_{21} v_{i,j} - \frac{R}{a \cos \theta_{21} \Delta \lambda} \left(\frac{T_{i,j} + T_{i,j+1} + T_{i+1,j} + T_{i+1,j+1}}{P_{i,j} + P_{i,j+1} + P_{i+1,j} + P_{i+1,j+1}} \right) \left(\frac{P_{i,j+1} + P_{i+1,j+1}}{2} - \frac{P_{i+1,j} + P_{i,j}}{2} \right)] = 0 \quad (3.13)$$

For a P-grid point on the boundary, the pressure gradient in the direction normal to the boundary is related to the u- or v-component through the finite-difference form of the geostrophic relation. For a corner point on the boundary, the pressure is computed by averaging the two pressure values respectively obtained from the u- and v-geostrophic components.

The finite-difference equations (3.11) through (3.13) are solved one at a time in a cyclic manner. The initial guess for u and v is the surface geostrophic wind components computed from the satellite-derived wind. The initial P field is obtained by averaging the three pressure fields individually computed from the geostrophic wind equations with the pressure observation at any three grid points (assuming that at least three grid points will have observed surface pressure). The iterative process is terminated when the difference in u and v between two successive iterations is no greater than 0.1 cm/s and that in P is no greater than 0.01 mb. Different initial guesses for P should only slightly influence the rate of convergence of the iterative procedure, not the final result.

IV. Results of Numerical Experiments

A number of numerical experiments were designed to investigate the following aspects of the variational SEASAT data analysis technique:

(i) determination of the weights, (ii) influence of the boundary condition, (iii) effect of data density of pressure, (iv) effect of quality of the SEASAT-derived wind data, and (v) influence of the surface temperature field.

In all the numerical experiments we ran, the target area was chosen to be the region bounded by Latitudes 16°N and 32°N and by Longitudes 152°W and 168°E in the Pacific Ocean. For each case of the numerical experiments, the true solution against which results of the variational SEASAT data analysis technique was compared was a certain FGGE IIIB surface pressure field and its associated geostrophic wind field expressed in a mesh of 4° grid resolution.

IVa. Determination of weights

The first problem we face in developing the SEASAT variational adjustment technique is to determine Weights A and B in (3.7). Even though we know of no clearcut way to choose these weights without making numerical experiments, a close look at Equations (3.8), (3.9), and (3.10) would more or less shed some light on how to determine them.

To begin with, we notice that the density of surface pressure observations is rather low over the ocean areas. Thus, values of p_s are known only at a few grid points in the entire domain. The surface pressure at all other grid points needs to be determined by the satellite-derived surface wind data. In order for this to hold, Weight A has to take on a very large value at those grid points where surface observations of pressure are available, and A has to be small enough (effectively zero) at all the other P-grids. For any given assignment of the A values at all grid points, a vanishing value of B would mean no adjustment of the wind. I.e., u and v would take on the surface geostrophic wind components u_s and v_s computed from the SEASAT wind data. As the value of B gradually increases, the adjustment of wind is also allowed to increase. If a larger and larger value of B is used, then we would suspect that since the adjusted surface geostrophic wind will have less and less to do with the original surface geostrophic wind, the adjustment may eventually become unsoundly large. When this takes place, the

resultant pressure field will become meaningless so that it may bear no resemblance to the true pressure field. Thus, by defining the target area to be the smallest area bounded by two meridians and two parallels and containing all the known P_g points, we may determine the best value of B that results in the smallest RMS error of the target area.

In order to obtain numerical values of A and B, we chose to use the mesh shown in Fig. 3 as the computational domain. The dots in the mesh indicate that observed surface pressure values at those points were given. This domain is certainly larger than the target area defined above. The presence of a buffer zone surrounding the target area as shown in Fig. 3 is intended to prevent the boundary condition from contaminating the solution in the target area. An extensive discussion of this subject will be presented in Section VIb.

In making numerical experiments to determine values of A and B, we first ran our variational code with the February 25, 00z, 1979 data in 4° grid resolution. We found that by assigning an A value of $0.25 \text{ E-4 m}^3/\text{g}$ or larger to those grid points with observed surface pressure, the resultant surface pressure values at these points remained unchanged from the observations P_g . Thus, by fixing A to be $0.25 \text{ E-4 m}^3/\text{g}$ at the grid points of known P_g , we list in Table 1 the RMS errors of the target area for three values of B versus six values of A at the grid points of unknown P_g . The range expanded by those A and B values was chosen to be wide enough to reveal a general trend. We remark in here that because the surface pressure field is what we are interested in getting, when the term RMS error is used, it refers to the RMS error of surface pressure in the target area. This convention will hold throughout the entire discussion of this study. It can be seen from Table 1 that the smallest RMS error appears when $A=0.25\text{E-13 m}^3/\text{g}$ and $B=1.\text{E7 s}^2$, although other combinations of A and B may result in RMS errors that

are only slightly larger. Table 1 also reveals that a monotonic reduction of the value of A does not always yield a smaller RMS error. Thus, we decided to choose A to be $0.25 \text{ E-4 m}^3/\text{g}$ for the grid points of known P_s , $0.25 \text{ E-13 m}^3/\text{g}$ for all other P-grids, and B equal to $1. \text{E7 s}^2$ as the most reasonable choice. In an attempt to find out whether or not $B = 1. \text{E7 s}^2$ was also a reasonable value for other data sets, we also included the March 01 and March 09, 00z, 1979 data sets in the numerical study. The RMS errors computed for six B values using the three data sets are presented in Table 2. It can be seen that when B falls in the range between 1.0 E6 and 1.0 E8 s^2 , the RMS error of the target area reaches a general low-value region. The fluctuation of the RMS error is small within this range of B, indicating that any value of B in this range can be considered acceptable. When B falls out of this range, however, the RMS error drastically increases. Thus for all three data sets tested, $A=0.25 \text{ E-4 m}^3/\text{g}$ or larger for known P_s grids, $A=0.25 \text{ E-13 m}^3/\text{g}$ or smaller for unknown P_s grids and $B=1.0 \text{ E7 s}^2$ for all grid points is a reasonable choice. If a value other than 1.0 E7 s^2 is to be used for B, then as long as B lies in the range between 1.0 E6 s^2 and 1.0 E8 s^2 the choice will be considered acceptable, too. From this point on, all the numerical experiments to be discussed were conducted with the specification of A and B described above.

Plots of the true solution of P, u and v on February 25, 00z, 1979 are shown in Fig. 4. Figs. 5a, 6a and 7a give plots of the computed P-, u- and v- fields for $B= 1. \text{E5}$, $1. \text{E7}$ and $1. \text{E10 s}^2$. The difference fields of P, u and v between the true solutions shown in Fig. 4 and the numerical solutions shown in Figs. 5a, 6a and 7a are respectively plotted in Figs. 5b, 6b and 7b for easy comparison. In all the pressure plots, two longitudes and two latitudes are drawn to mark out the target area, and dots are used to denote locations of the input pressure

observations. It is obvious that the error is generally smaller inside the target area, but it may become very large away from the target area. This point will be discussed in detail in the next section. A comparison of Figs. 5b, 6b and 7b verifies our previous conclusion drawn from examination of Table 1 that $B=1.E7 \text{ s}^2$ produces the least RMS error compared with $B=1.E5$ and $1.E10 \text{ s}^2$. Similar plots for data sets of March 01 and March 09, 00z, 1979 are respectively shown in Figs. 8, 9a,b, 10a,b, 11a,b and Figs. 12, 13a,b, 14a,b, 15a,b. A close examination of these figures shows that our previous choice of B in the range of $1.E6$ and $1.E8 \text{ s}^2$ based on the February 25 data set is also supported by using the two additional data sets.

VIb. Influence of the boundary condition

In the previous section, we discussed employment of a computational domain larger than the target area in running numerical experiments. The reason for that will be made clear in this section.

When surface pressure observations are located near or on the boundary of the domain, one might suspect that discretization of the boundary condition could create inaccuracies that would enter into the interior part of the domain in the computation. And if this would indeed turn out to be true care must be taken to alleviate this difficulty.

As was mentioned in the previous section, the target area is the smallest area bounded by two meridians and two parallels containing all the grid points with surface pressure observations. Therefore, in order to determine the effect of the boundary condition, computational domains of sizes the same as and larger than the target area with identical surface pressure observations were used to suit our purpose. We actually employed four different domains in running numerical experiments. Domain A was identical with the target area. Domain B

exceeded the target area by one grid interval in each of the four directions. Domain C was larger than Domain B by one grid distance in the four directions. Domain D was an extension of one grid interval of Domain C in the longitudinal direction only. Actually, Domain D was the same as the computational domain used in the numerical experiments discussed in the previous section, and the same set of the five surface pressure observations used in the computations in Section VIa was also used for Domains A, B and C. The February 25, 00z, 1979 data set was used as input data to run numerical experiments on these three domains. The resultant RMS errors of the target area for the four computational meshes A, B, C and D are listed in Table 3. This table clearly shows that the closer the surface pressure observations are located near the domain boundary, the larger is the RMS error of the target area as we suspected earlier. It is also clear that an expanded computational domain may advantageously be used to alleviate the difficulty associated with the boundary condition. The RMS error decreases when grid points with pressure observation are farther removed from the domain boundary. Moreover, the RMS errors obtained on Mesh C and Mesh D are seen to be not too different from each other, which indicates that a buffer zone at least two grid intervals long and wide as shown in Mesh C will be required to prevent the boundary condition from contaminating the interior domain. This will be used as a general rule. The best way to determine the appropriate computational domain, however, is to conduct a series of numerical experiments with an increasing size of the buffer zone. When there is no further change in RMS error due to change in the size of buffer zone, the appropriate computational domain is thus decided.

The true solution of u , v and P is shown in Fig 4. The u -, v - and P -fields computed on Meshes A, B, C, D and their difference from the true solutions are shown in Figs. 16a,b, 17a,b, 18a,b and 6a,b, respectively. As before, two longi-

tudes and two latitudes were drawn in each of these plots to mark out the target area. It can be seen by comparing Figs. 6b, 16b, 17b and 18b that when an expanded computational domain is used, the error is extremely large outside the target area, whereas inside the target area the error is significantly smaller. This finding justifies our use of Grid D in conducting the numerical experiments presented in Section VIa.

VIc. Effect of data density of surface pressure

The essence of the current SEASAT data analysis technique is to use the dense wind data obtained by the SEASAT observation to help improve the surface pressure analysis in the data-sparse area over the oceans. Thus, it is straightforward to expect that the denser the surface pressure observation is, the more accurate will be the result of the variational SEASAT data analysis. In order to verify this speculation by making numerical experiments, we chose to analyze the February 25, 00Z, 1979 data set on the D grid using A and B values found in Section VIa. Three cases were run: (i) Case 1 used only three of the five P_s grid points appeared in the numerical experiments discussed in the previous two sections; (ii) Case 2 used the same five P_s grids as before; (iii) Case 3 used seven grid points of known P_s with five of these points identical with the P_s points in Case 2. Table 4 gives the RMS error of the target area for all three cases. As expected, the RMS error for Case 3 is the smallest whereas the RMS error for Case 1 is the largest. Plots of the computed P , u and v fields and their difference from the true solution are respectively shown in Figs. 19a,b, 6a,b, and 20a,b. It is informative to note that when too few surface pressure observations are available, the result of the variational SEASAT data analysis is rather inaccurate as evidenced by Figs. 19a,b. A comparison of the difference fields plotted in Figs. 19b, 6b and 20b shows a persistent increase in accuracy of the resultant pressure

analysis as a greater number of surface pressure observations became available. However, this was the case simply because the input pressure data in Case 1 formed a subset of the pressure data in Case 2, which themselves formed a subset of the pressure data in Case 3. In general, a greater number of pressure observations do not necessarily lead to a more accurate pressure analysis. It is expected that when more observations of surface pressure are available in regions of strong pressure gradient, will we get a better pressure analysis. In order to verify this point, two additional runs were made on the same computational domain using the same A and B values. Six pressure data points were used in both runs, but the locations of those pressure data were different. In the first run, three pressure observations were located equidistantly on the eastern boundary of the target area, and another three pressure data were regularly spaced on the western boundary of the target area. In the second run, however, the pressure data points were chosen such that three regularly spaced data points appeared on each of the northern and southern boundaries of the target area. RMS errors computed for the target area are respectively 0.647 and 1.084 mb for the two cases, and contour plots of P-, u-, v- and the difference fields are respectively shown in Fig. 21 and Fig. 22. It is obvious that a much better accuracy was obtained in the former run when compared with the latter. The reason for this is not very difficult to explain: An examination of the pressure field shown in Fig. 4 reveals that regions of strong pressure gradient are located more close to the eastern and western boundaries than the northern and southern boundaries of the target area. Consequently, because more data points were available in regions of strong pressure gradient, a better accuracy was thus resulted in the former run when compared with the latter. By the same token, because regions of strong pressure gradient in Fig. 4 are closer to the boundary than to the interior of the target

area, if the two pressure data points located in the middle of the eastern and western boundaries of the target area in Fig. 21 were respectively shifted inward for two grid intervals, then a decrease in accuracy would be expected. An additional run was made to clarify this speculation. The resultant RMS error in this case is 1.2 mb, much larger than the RMS error of 0.65 mb associated with Fig. 21. The graphical results of this additional run are shown in Fig. 23 for ease of comparison.

VId. Effect of quality of SEASAT-derived wind data

When a new SEASAT satellite is launched into space in the future to provide sea surface wind data through remote sensing, it is expected to carry refined sensing devices. Consequently, the wind data derived from the satellite observation should more accurately represent the true surface wind over ocean areas. A reasonable question to ask in this regard is, "If the speed and direction errors associated with the SEASAT-derived wind data can be reduced by introduction of new devices, what impact will it have on the accuracy of the SEASAT pressure analysis?". In an attempt to assess the consequence of this, we performed the following numerical experiment: We reduced the standard deviation of the windspeed error from ± 2 to ± 1 m/s, and reduced the standard deviation of the error in wind direction from $\pm 20^\circ$ to $\pm 10^\circ$ in assimilating the satellite-derived wind data. The same data set and computational specification used in obtaining Fig. 6 were employed. The resultant RMS error of the target area is found to be 0.86 mb which is less than the RMS error of 0.89 mb associated with Fig. 6. A simple comparison of these two numbers does not reveal how the RMS error gets a little smaller, so we examine the P-, u- and v-fields and their difference from the true solution as plotted in Fig. 24. By comparing the two pressure difference fields in Figs. 6b and 24b, we observe that the RMS error is

almost halved near the central part of the target area, although the reduction in error quickly falls flat toward the boundary of the target area, where larger errors appear and dominate the total RMS error. This result reflects two things of different nature: (i) Effort to improve the quality of the SEASAT-derived wind data is worth seeking, because it tends to significantly reduce the pressure error near the central part of the target area; and (ii) Except for the error imbedded in the SEASAT-derived wind data, other factors such as the total number of surface pressure observations, where they are located in relation to regions of strong pressure gradient, and what computational domain is in use, as have been discussed in the previous sections may all influence the outcome of the SEASAT data analysis technique. Thus without enough number of surface pressure observations in the region of interest, there is an upper limit on the accuracy of the SEASAT pressure analysis technique even with upgraded SEASAT-derived wind data.

V1e. Influence of the surface temperature field

In all the previous numerical experiments discussed, we have tacitly assumed that the surface temperature field is completely known at every grid point. However, unless the sea surface temperature field is already obtained elsewhere, say by blending the satellite temperature observations into the conventional data, the temperature can only be known at those same grid points where surface pressure is observed. When this is not the case, a convenient alternative is to use a constant temperature field in the SEASAT data analysis. This constant temperature can be taken as, for instance, a representative mean temperature of the entire domain. Thus, we made three numerical runs to find out how much influence this may have on the outcome of the SEASAT pressure analysis. The control case was chosen to be the one shown in Fig. 6. In the three runs we made, the constant temperature was respectively chosen to be 300, 283 and 290 °K, the last one being

the average of the five given surface temperature observations. The 300 and 283 °K temperatures were used to represent more extreme cases. The resultant RMS errors were found to be 0.91, 0.89 and 0.87 mb, respectively for the 283, 290 and 300 °K temperatures. By comparing it with the RMS error of 0.89 mb of the control case, we see that the use of a representative mean temperature obtained by averaging the given surface temperature observations almost produced an identical result to the control case. Use of the two extreme temperatures yielded somewhat different surface pressure fields from the control case, yet the difference is not too distinctive. Graphical comparisons of these results can be made by examining plots of the velocity and surface pressure fields and their difference from the true solutions as shown in Figs. 25, 26 and 27. We consequently determined that a fairly good surface pressure field can be obtained by the SEASAT data analysis technique without knowing the complete surface temperature field.

V. Concluding Remarks

The SEASAT-derived wind can be considered as the neutral stability vector wind at 19.5 m above sea level with an accuracy up to ± 2 m/s and $\pm 20^\circ$ respectively in speed and direction. These errors are considered characteristic and were used in assimilating the SEASAT-derived wind data from the geostrophic wind field of a chosen surface pressure field. With the help of the geostrophic drag law and an empirical formula of the neutral stability drag coefficient, the assimilated SEASAT-derived wind data could be converted to the corresponding surface geostrophic wind at 10 m above the sea level. A variational problem with the geostrophic wind relation as the weak constraint was then formed to combine the sparse surface pressure data with the dense SEASAT-derived wind data together. After this variational problem was solved numerically, the resultant adjusted pressure field was compared with the input true pressure field. In conducting

this study, we have reached the following conclusions:

- (1) Weight A that appears in the computation of the variational problem can be reasonably chosen to be $0.25\text{E-}4 \text{ m}^3/\text{g}$ at those grid points where surface pressure observation is available. For all other grid points without the pressure data, a reasonable value of A is $0.25\text{E-}13 \text{ m}^3/\text{g}$. Weight B can be assigned a uniform value of $1.\text{E}7 \text{ s}^2$ over the entire domain, however, any value between $1.\text{E}6\text{s}^2$ and $1.\text{E}8 \text{ s}^2$ is also considered acceptable.
- (2) In order to avoid possible contamination of the region of interest (target area) by the boundary condition, it is recommended that a computational domain larger than the target area by at least two grid intervals in each of the four directions be employed. Any domain smaller than this will likely lead to very inaccurate result. A more appropriate way to determine the size of the computational domain is through conducting a series of numerical experiments with increasing buffer zones. When no more change in RMS error with increasing size of the buffer zone is observed, the proper computational domain is thus determined.
- (3) The greater the number of surface pressure observations there is, the higher the accuracy of the resultant pressure field will be. This is especially true in regions of strong pressure gradient.
- (4) An upgrade in quality of the SEASAT-derived wind data will result in an improvement in accuracy of the SEASAT pressure analysis technique. However, the extent to which the accuracy can be improved has an upper limit. Beyond that limit, further improvement can be expected only if more surface pressure observations become available.
- (5) The surface temperature field is usually not available at each mesh grid. However, in the current SEASAT data analysis technique, the employment of a constant temperature can result in a fairly reasonable surface pressure field.

Table 1. List of pressure RMS errors in mb for determining Weights A and B.

		Weight A (m^3/g) for grid points without surface pressure observation					
		0.25 E-10	0.25 E-11	0.25 E-12	0.25 E-13	0.25 E-15	0.25 E-22
Weight B (s^2)	1.0 E5	5.1	4.8	3.5	1.3	0.909	0.914
	1.0 E7	3.6	1.4	0.9	0.891	0.896	0.896
	1.0 E9	2.0	1.786	1.760	1.759	1.759	1.759

Table 2. List of pressure RMS errors in mb for determining Weight B for three different data sets

		Weight B (s^2)					
		1.0 E5	1.0 E6	1.0 E7	1.0 E8	1.0 E9	1.0 E10
Set Data	Feb 25 00Z 1979	1.3	0.9	0.9	0.9	1.8	3.6
	Mar 1 00Z 1979	2.0	0.9	1.0	0.9	1.1	4.4
	Mar 9 00Z 1979	1.3	1.0	1.0	1.0	³ 1.4	2.2

Table 3. List of pressure RMS errors in mb for determining the boundary effect

	Computational Domain			
	A	B	C	D
RMS error	2.6	1.1	0.9	0.9

Table 4. List of Pressure RMS errors in mb for different data densities of surface pressure observation

No. of Pressure Observations in domain												
3					5				7			
Weight B (s ²)					Weight B (s ²)				Weight B (s ²)			
1.E6	1.E7	1.E8	1.E9		1.E6	1.E7	1.E8	1.E9	1.E6	1.E7	1.E8	1.E9
RMS error	2.0	2.1	1.9	1.9	0.9	0.9	0.9	1.8	0.7	0.7	0.8	1.8

Figure Captions

- Fig. 1 Schematic representation of the geostrophic drag law. α is the angle between the surface stress and the geostrophic wind.
- Fig. 2 Schematic of the staggered mesh used in conducting the SEASAT variational data analysis. $P_{1,j}$ is the grid point at which the $(1,j)$ -th surface pressure and weights A, B are located. $(u,v)_{1,j}$ represents the grid point where the $(1,j)$ -th u_g and v_g are located. The Coriolis parameter f_{21} is associated with the i -th row of u,v ; f_{21-1} is associated with the i -th row of p .
- Fig. 3 Schematic illustration of the computational domain, the target area, and the buffer zone. The dots in the mesh indicate locations of the surface pressure observations.
- Fig. 4 True solution of the surface pressure and geostrophic wind fields on February 25, 00z, 1979. From top to bottom: Contour plot of P in 2 mb intervals, contours of the field in 2 m/s, and contours of v_g in 2 m/s.
- Fig. 5a Variationally adjusted fields of P , u_g and v_g in 2 mb and 2 m/s contour intervals for $A = 0.25E13 m^3/g$ and $B^g = 1.E5 s^2$. Dots in the p -plot indicate locations of given surface pressure observations.
- Fig. 5b Contour plots of the difference between the fields shown in Figs. 4 and 5a in 0.5 mb and 2 m/s intervals. Dots in the δp plot indicate locations of given surface observations.
- Fig. 6a Same as in Fig. 5a except $B = 1.E7 s^2$.
- Fig. 6b Same as in Fig. 5b except $B = 1.E7 s^2$.
- Fig. 7a Same as in Fig. 5a except $B = 1.E10 s^2$.
- Fig. 7b Same as in Fig. 5b except $B = 1.E10 s^2$.
- Fig. 8 Same as in Fig. 4 except for using the March 1, 00z, 1979 data set.
- Fig. 9a Same as in Fig. 5a except for the March 1, 00z, 1979 data set.
- Fig. 9b Same as in Fig. 5b except for the March 1, 00z, 1979 data set.
- Fig. 10a Same as in Fig. 6a except for the March 1, 00z, 1979 data set.
- Fig. 10b Same as in Fig. 6b except for the March 1, 00z, 1979 data set.
- Fig. 11a Same as in Fig. 7a except for the March 1, 00z, 1979 data set.
- Fig. 11b Same as in Fig. 7b except for the March 1, 00z, 1979 data set.
- Fig. 12 Same as in Fig. 4 except for using the March 9, 00z, 1979 data set.

Fig. 13a Same as in Fig. 5a except for the March 9, 00Z, 1979 data set.

Fig. 13b Same as in Fig. 5b except for the March 9, 00Z, 1979 data set.

Fig. 14a Same as in Fig. 6a except for the March 9, 00Z, 1979 data set.

Fig. 14b Same as in Fig. 6b except for the March 9, 00Z, 1979 data set.

Fig. 15a Same as in Fig. 7a except for the March 9, 00Z, 1979 data set.

Fig. 15b Same as in Fig. 7b except for the March 9, 00Z, 1979 data set.

Fig. 16a Same as in Fig. 6a except for the use of Grid A (see text).

Fig. 16b Same as in Fig. 6b except for the use of Grid A (see text).

Fig. 17a Same as in Fig. 6a except for the use of Grid B (see text).

Fig. 17b Same as in Fig. 6b except for the use of Grid B (see text).

Fig. 18a Same as in Fig. 6a except for the use of Grid C (see text).

Fig. 18b Same as in Fig. 6b except for the use of Grid C (see text).

Fig. 19a Same as in Fig. 6a except that only three of the five pressure observations used in Fig. 6a were employed as the input data.

Fig. 19b Same as in Fig. 6b except that only three of the five pressure observations used in Fig. 6a were employed as the input data.

Fig. 20a Same as in Fig. 6a except two additional pressure observations were included in the input data.

Fig. 20b Same as in Fig. 6b except two additional pressure observations were included in the input data.

Fig. 21a Same as in Fig. 6a except that the input pressure observations used were different.

Fig. 21b Same as in Fig. 6b except that the input pressure observations used pressure observations.

Fig. 22a Same as in Fig. 6a except that the input pressure observations used pressure observations.

Fig. 22b Same as in Fig. 6b except that the input pressure observations used pressure observations.

Fig. 23a Same as in Fig. 6a except that the input pressure observations used pressure observations.

- Fig. 23b Same as in Fig. 6b except that the input pressure observations used pressure observations.
- Fig. 24a Same as in Fig. 6a except that the errors in the assimilated SEASAT wind data were reduced from ± 2 m/s and 20° to ± 1 m/s and 10° .
- Fig. 24b Same as in Fig. 6b except that the errors in the assimilated SEASAT wind data were reduced from ± 2 m/s and 20° to ± 1 m/s and 10° .

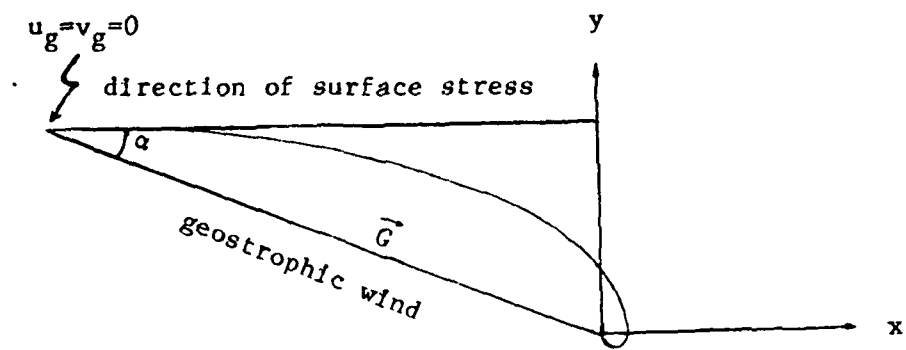


Fig 1

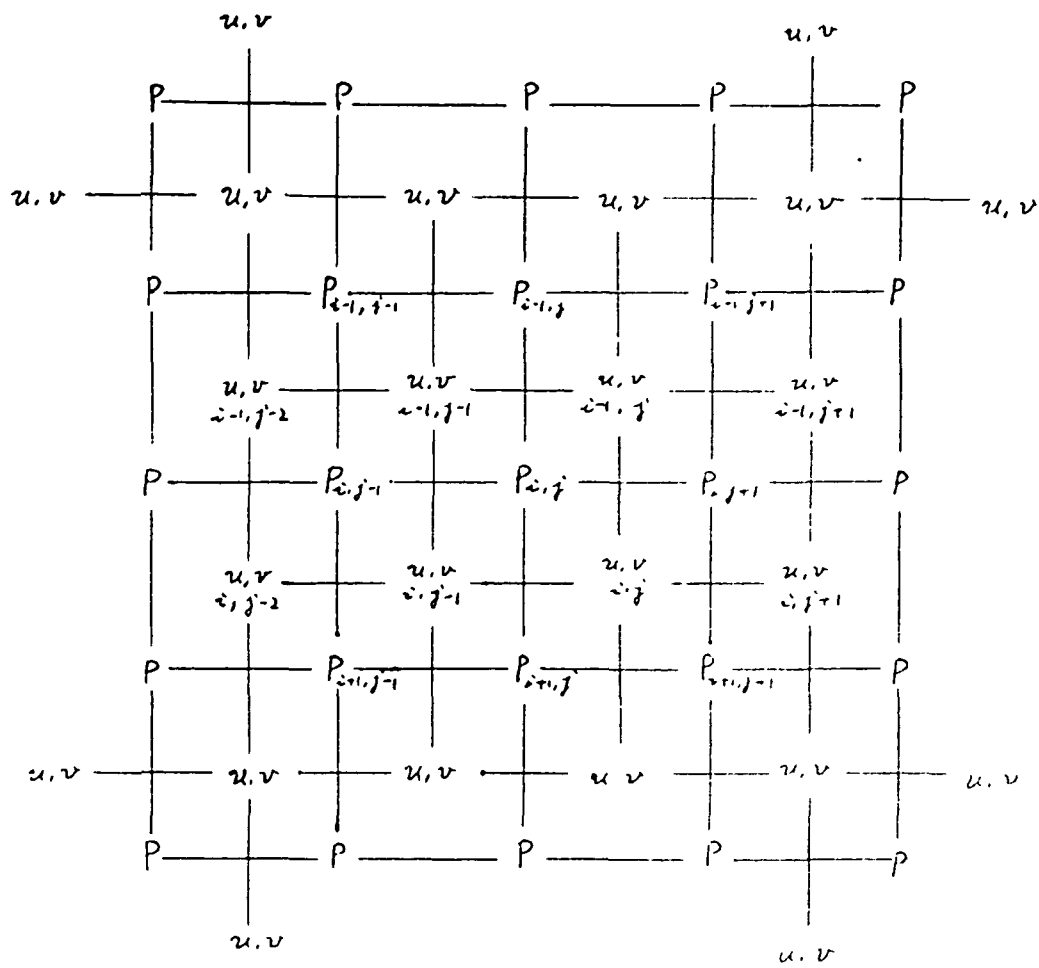


Fig. 2

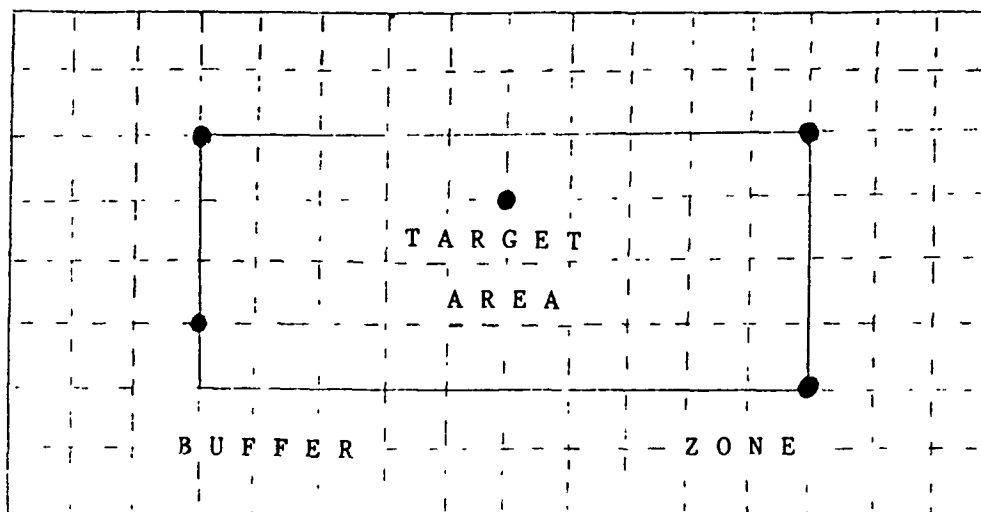


Fig 3

ORIGINAL PAGE IS
OF POOR QUALITY

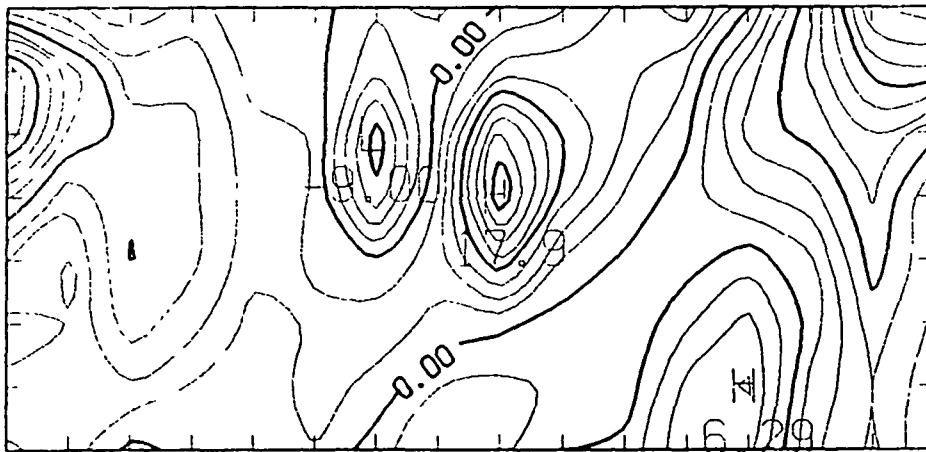
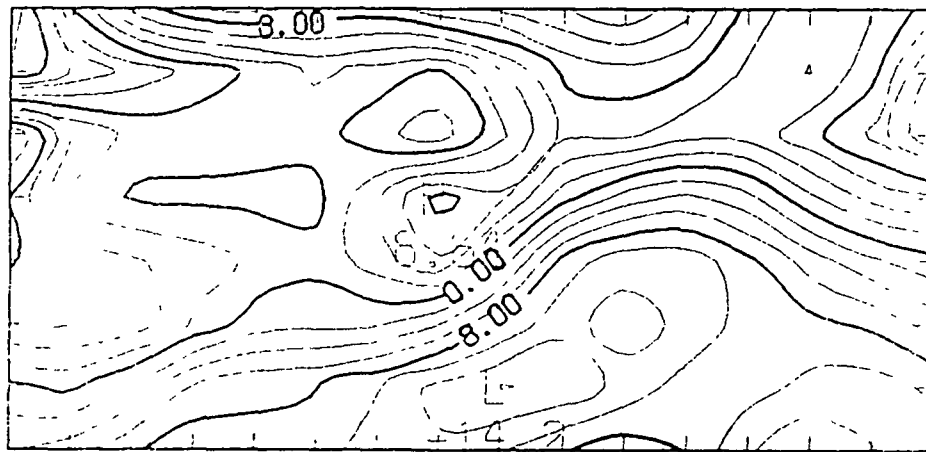
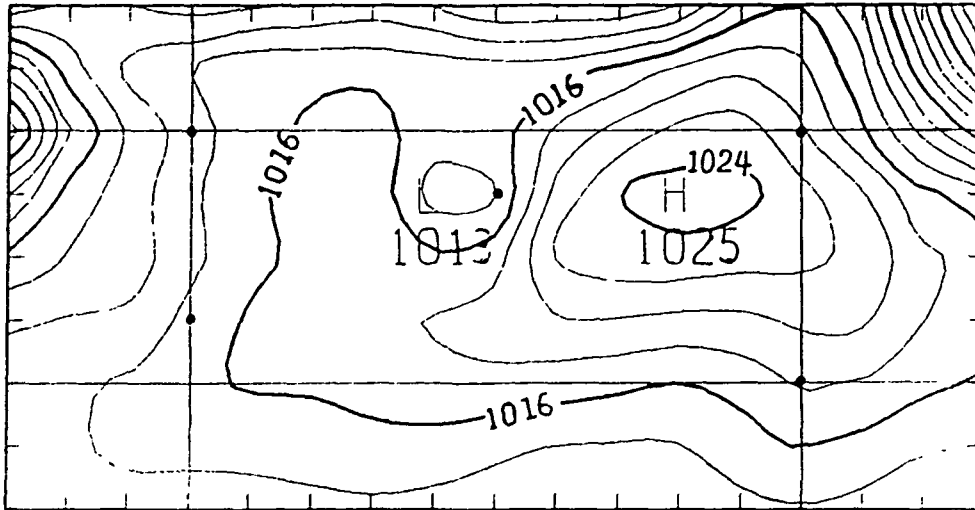


Fig 4

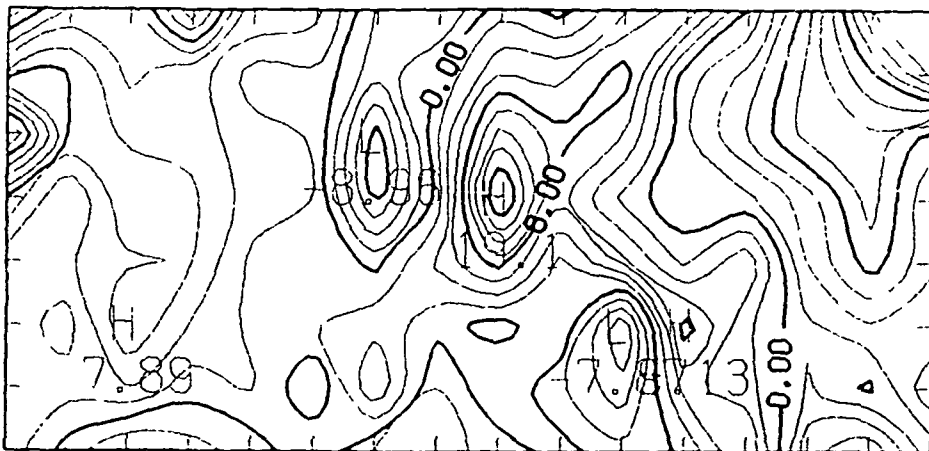
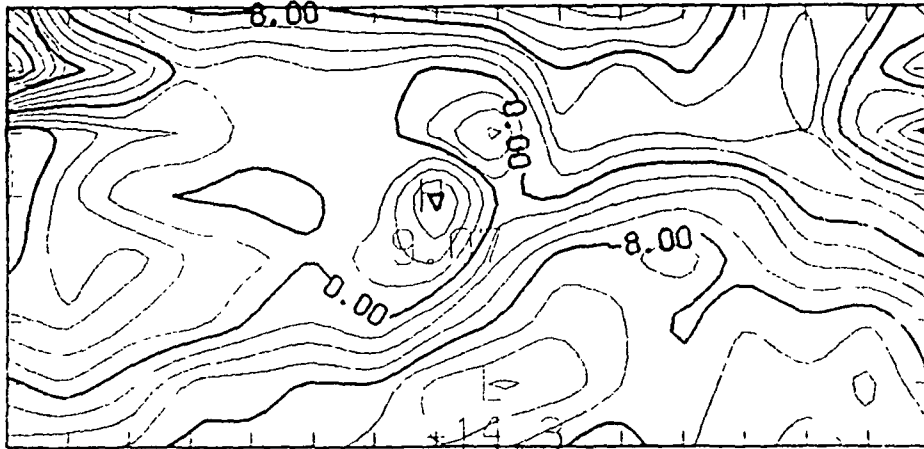
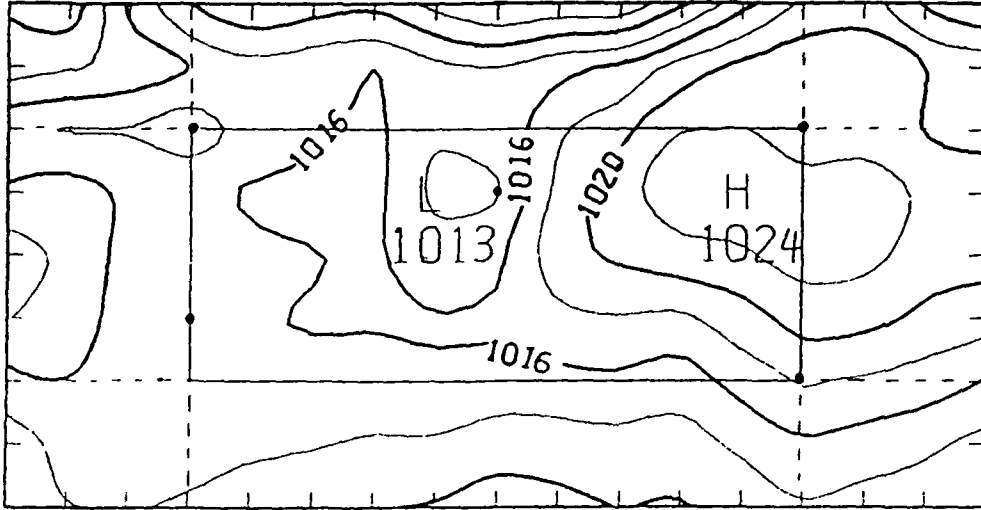


Fig. 5a

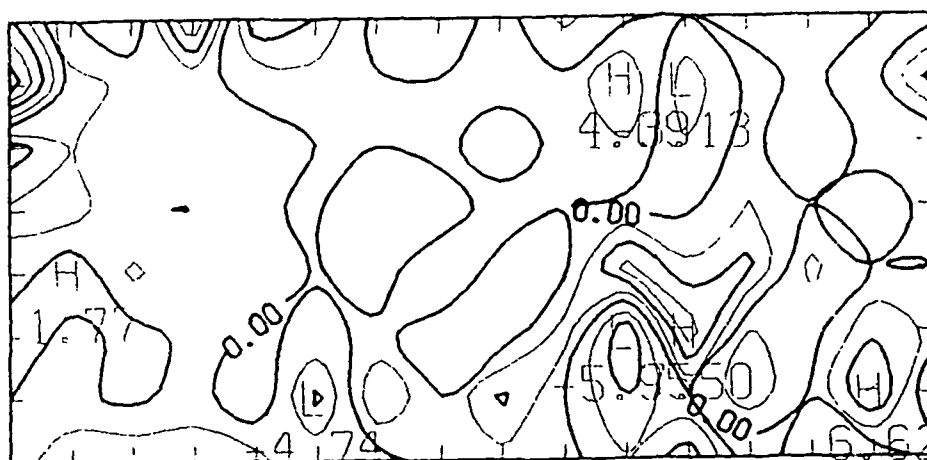
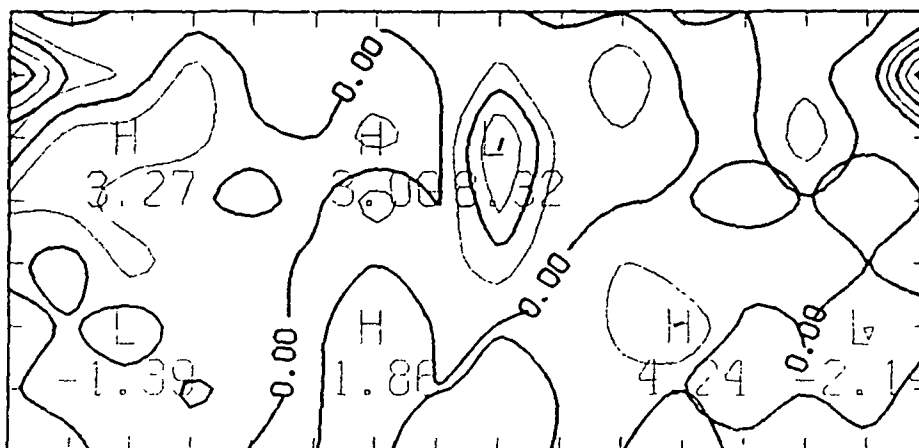
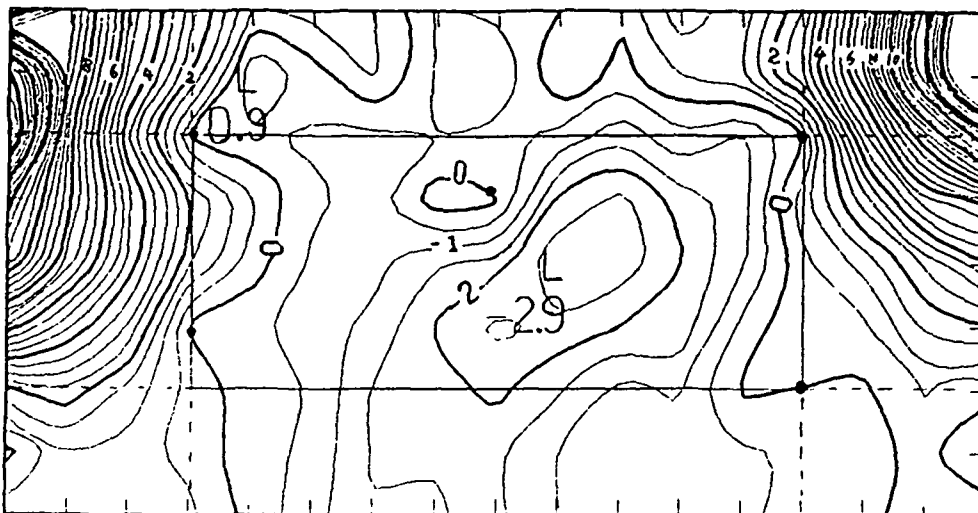


Fig. 5b

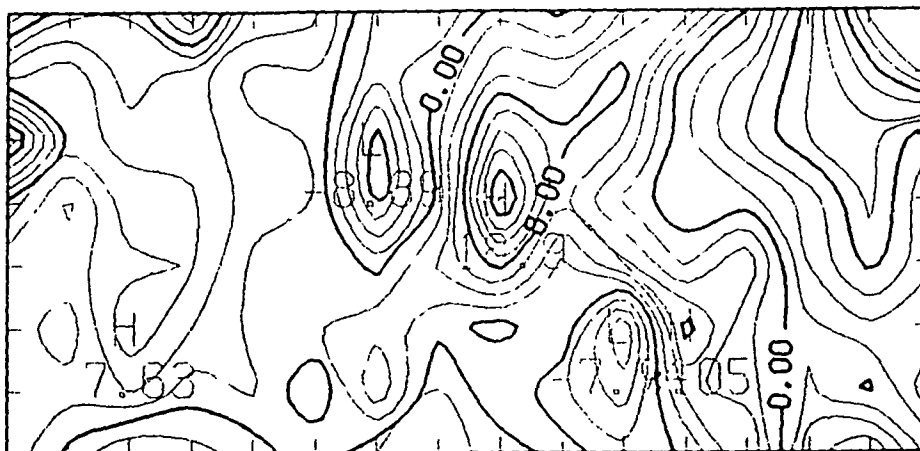
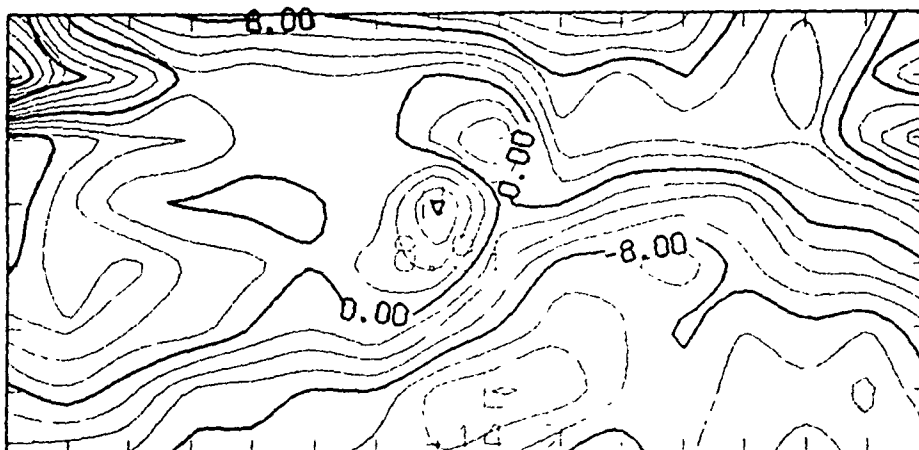
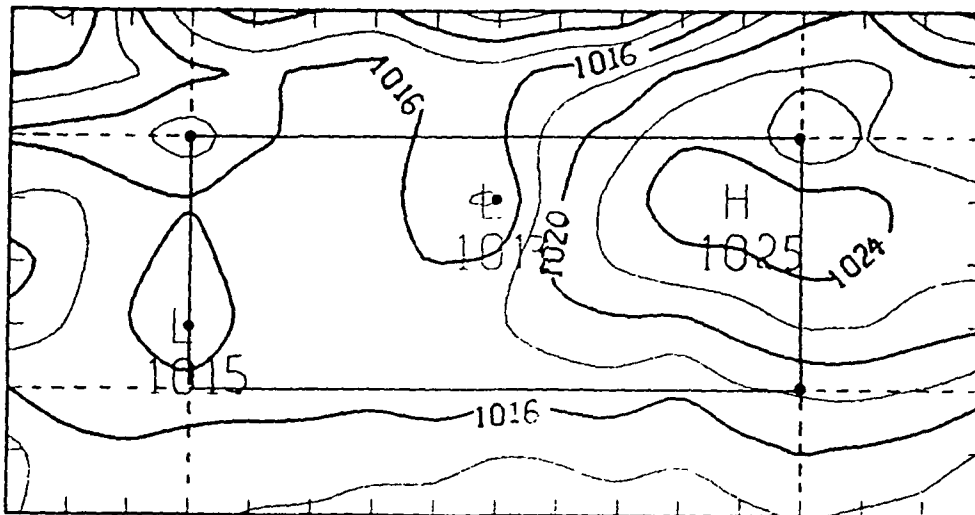
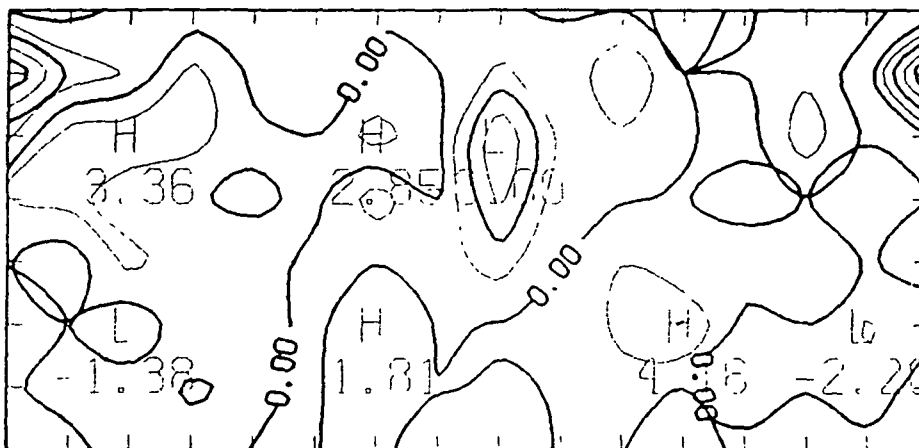


Fig. 6a



-37-

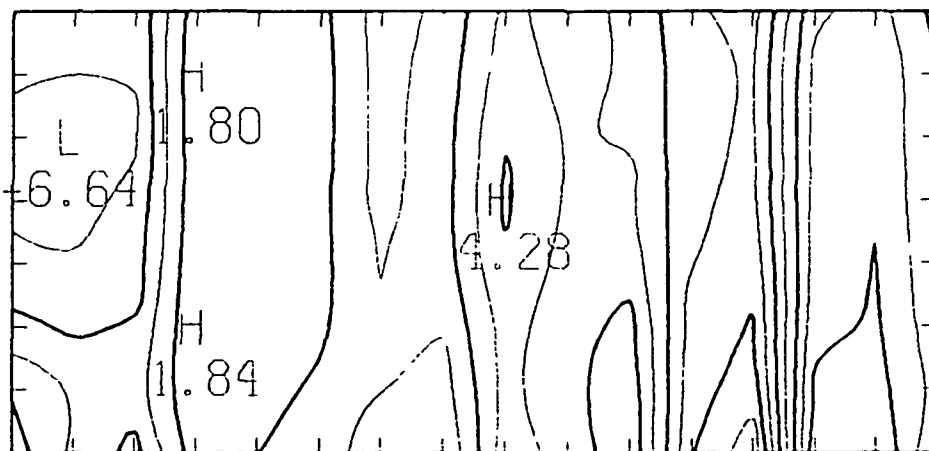
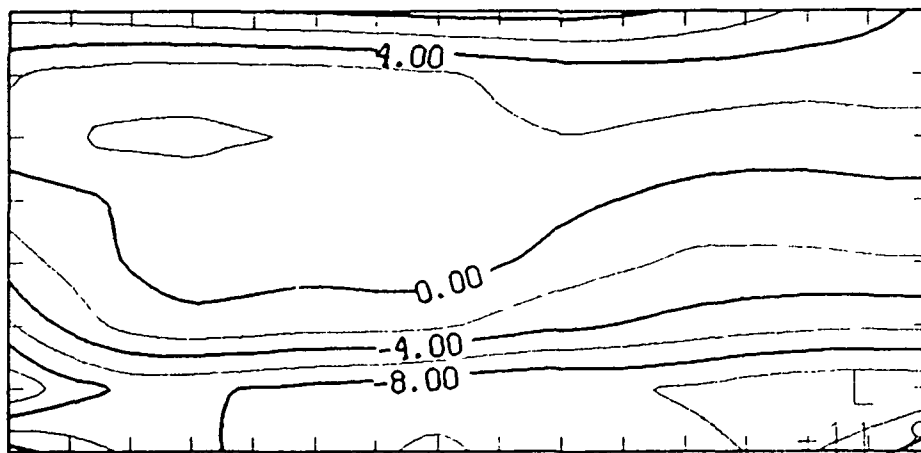
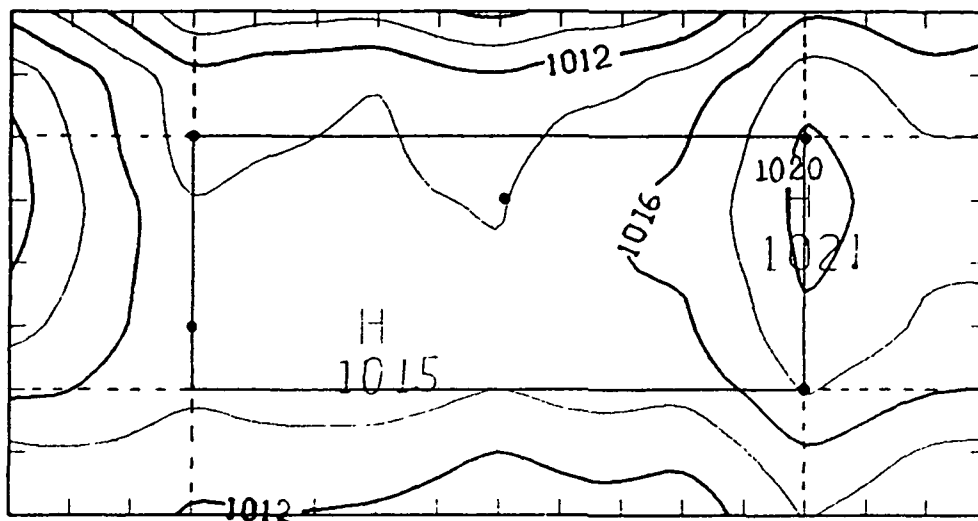


Fig. 7a

ORIGINAL PAGE IS
OF POOR QUALITY

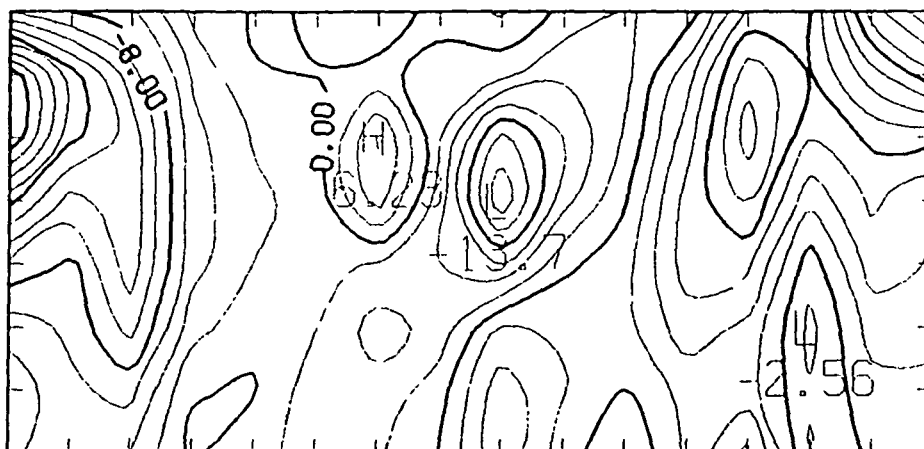
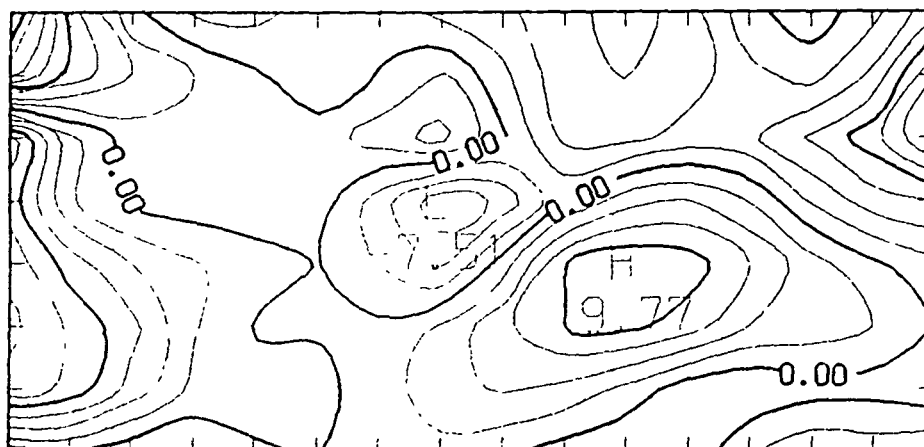
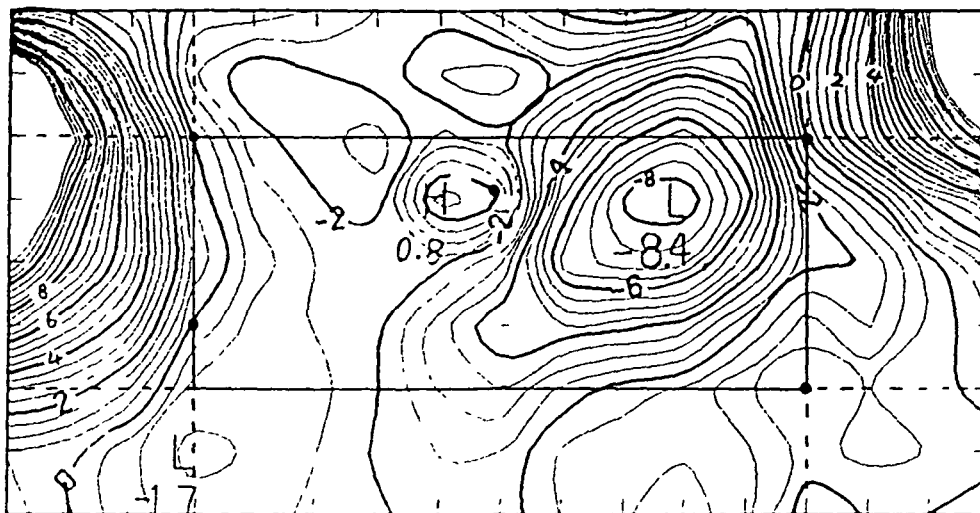


Fig. 7b

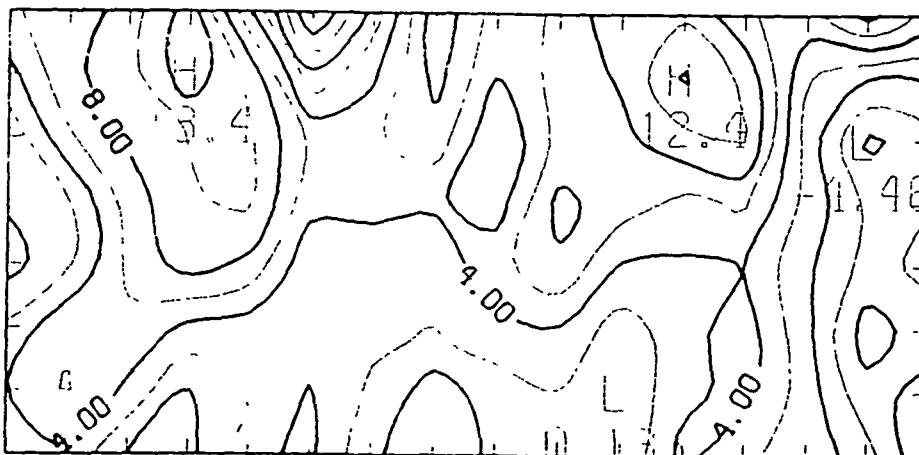
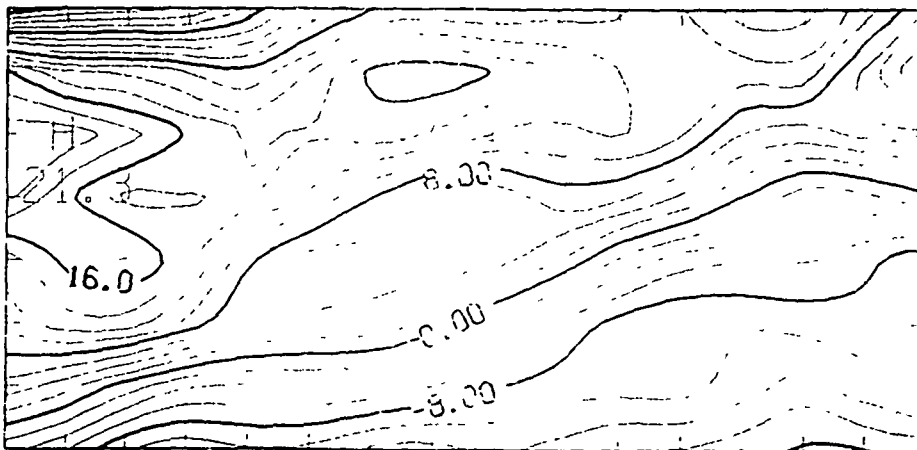
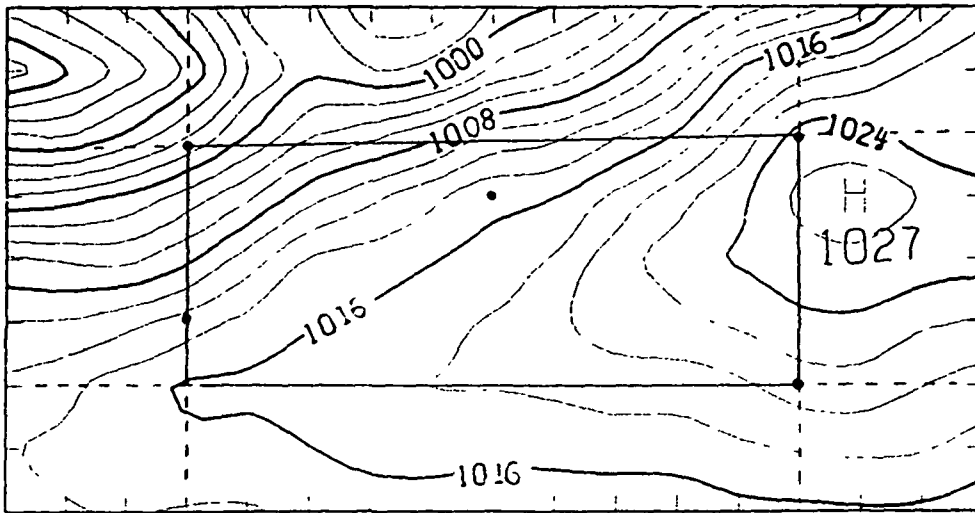


Fig. 8

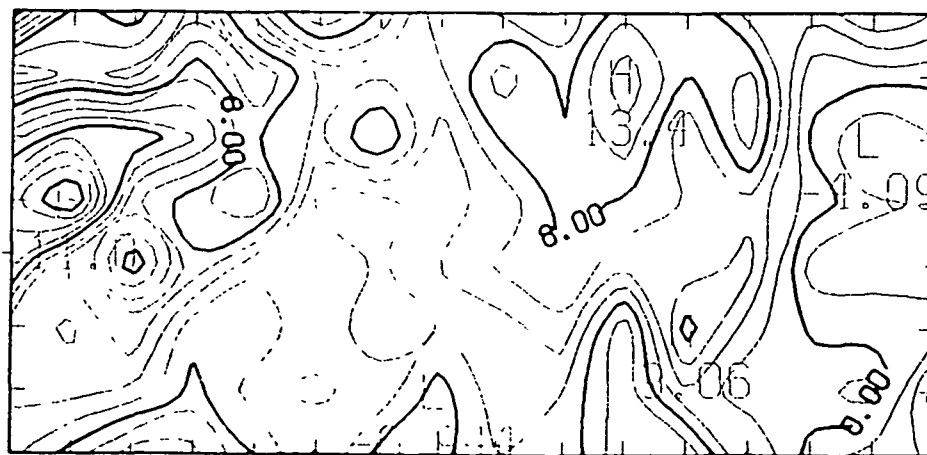
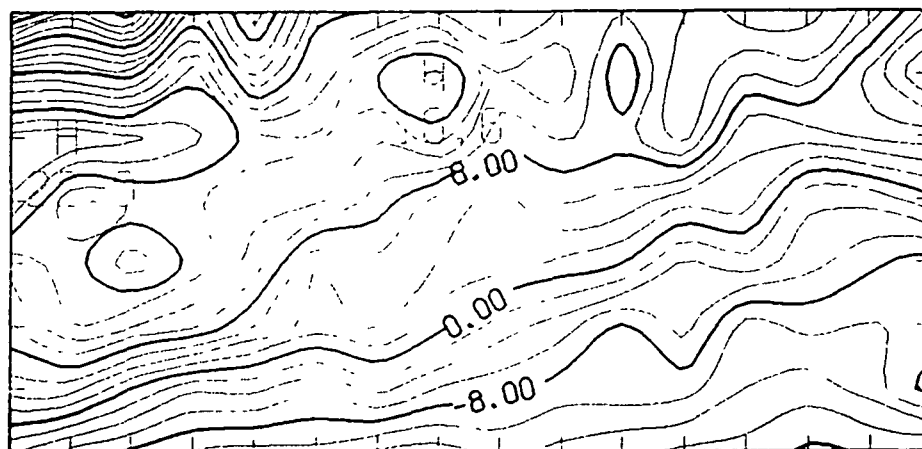
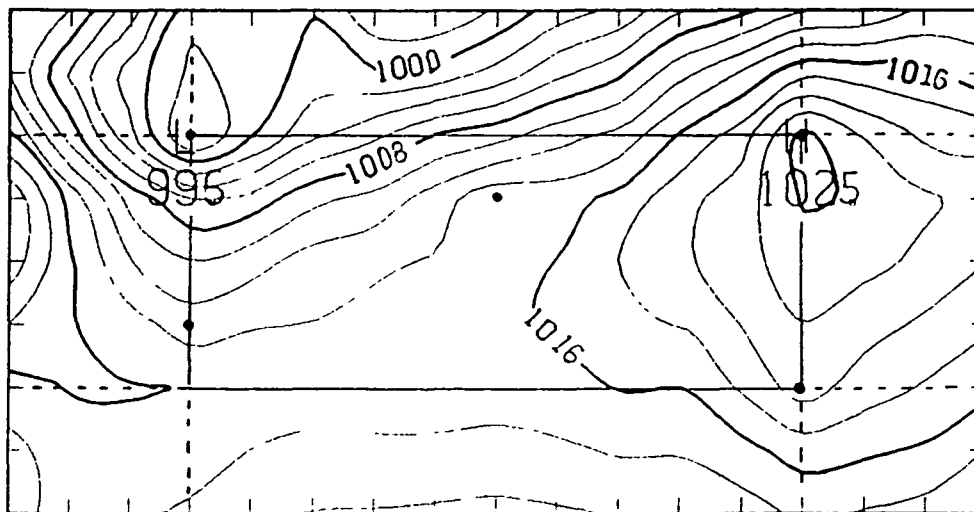


Fig. 9a

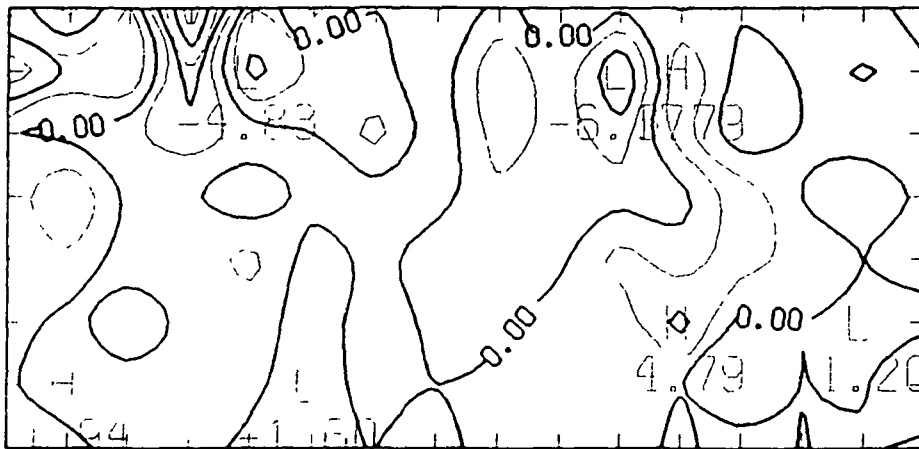
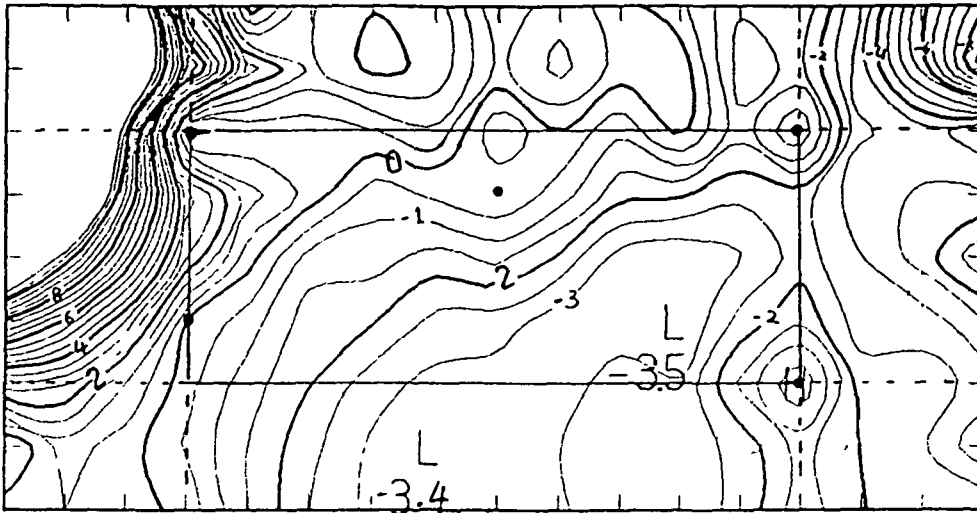


Fig. 9b

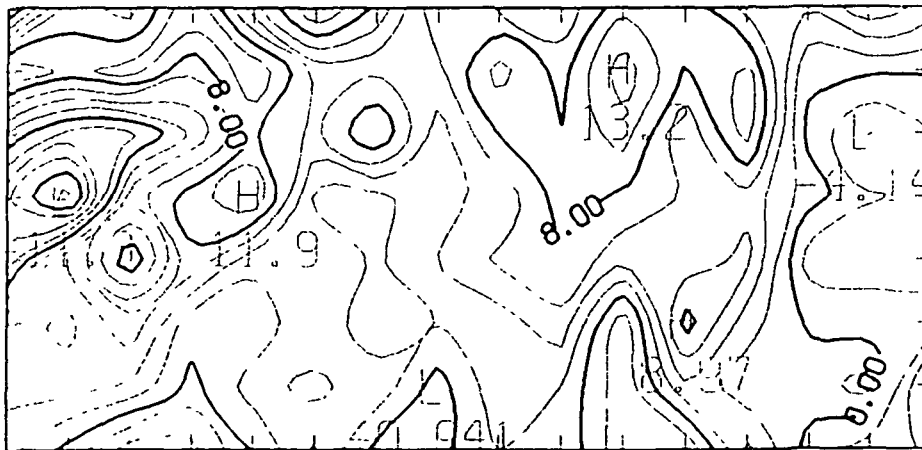
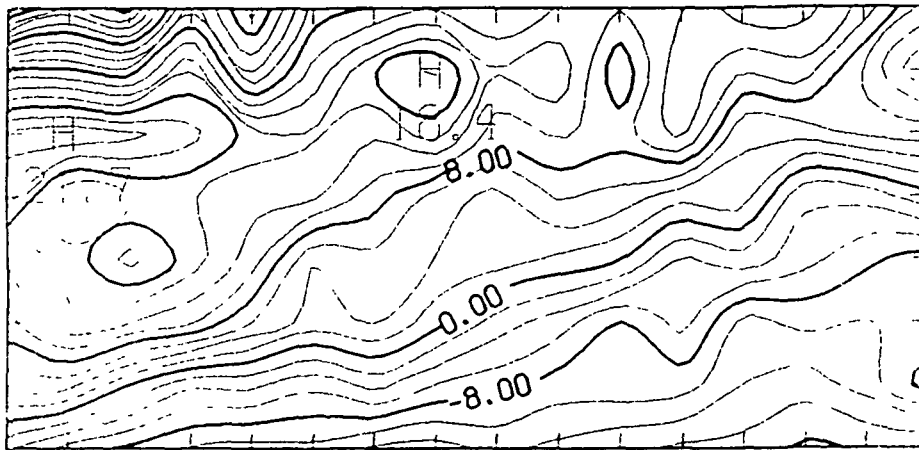
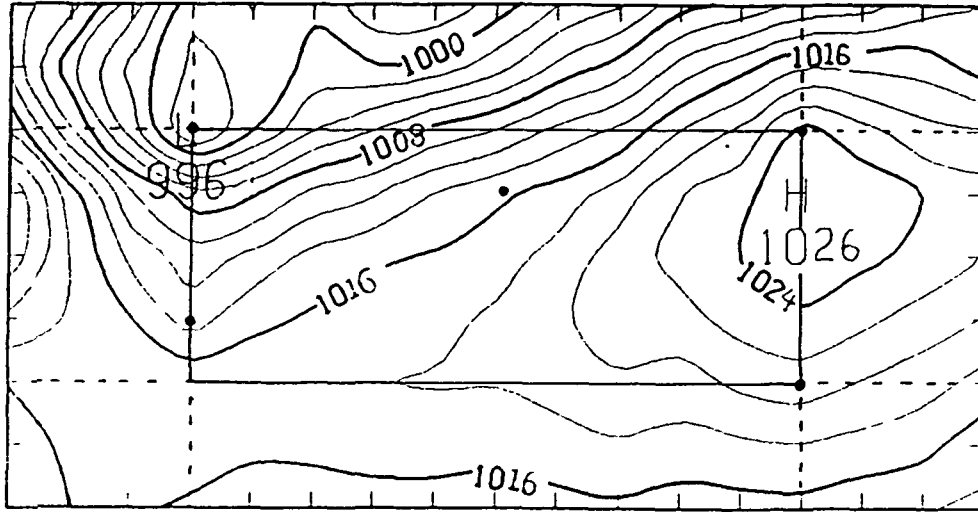


Fig. 10a

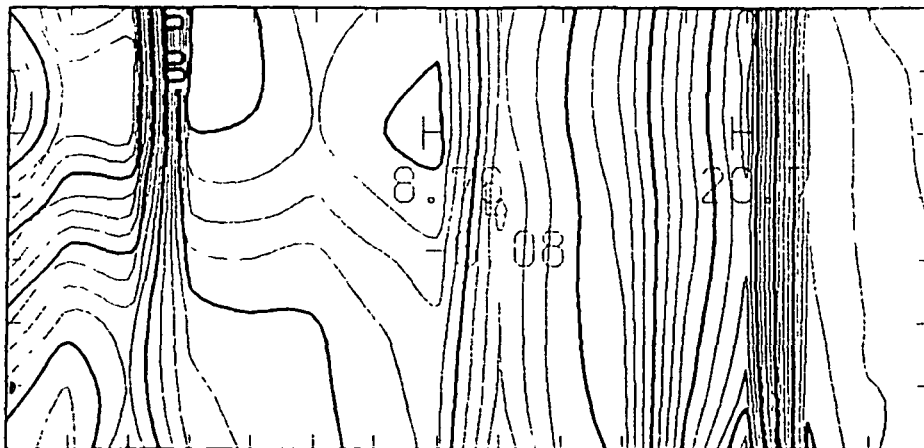
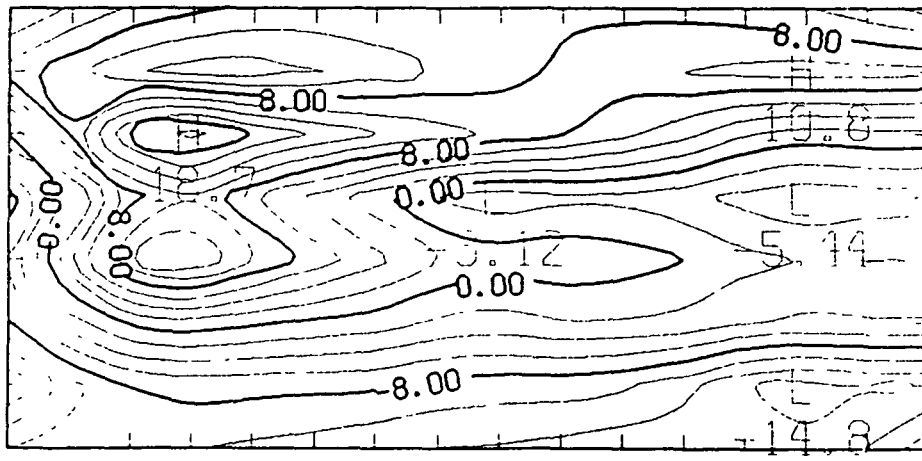
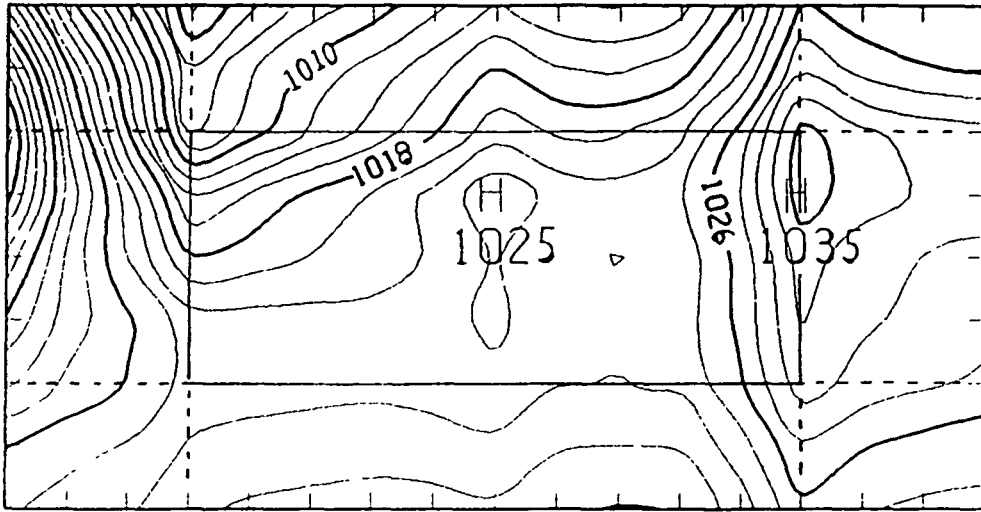


Fig. 11a

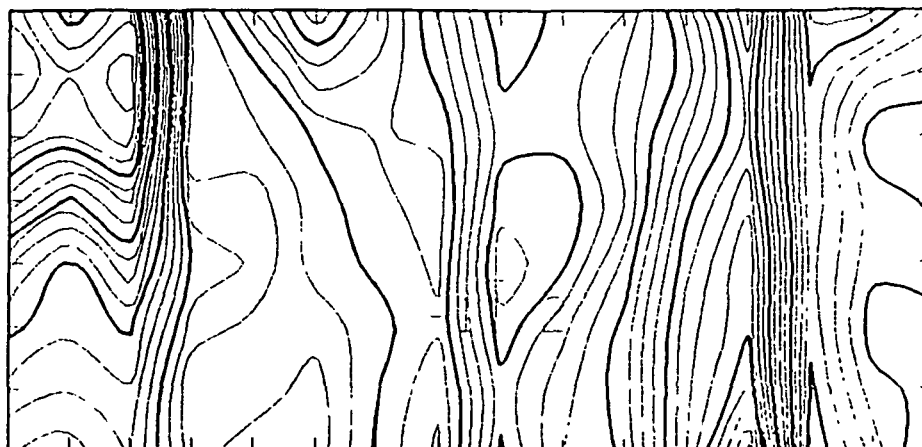
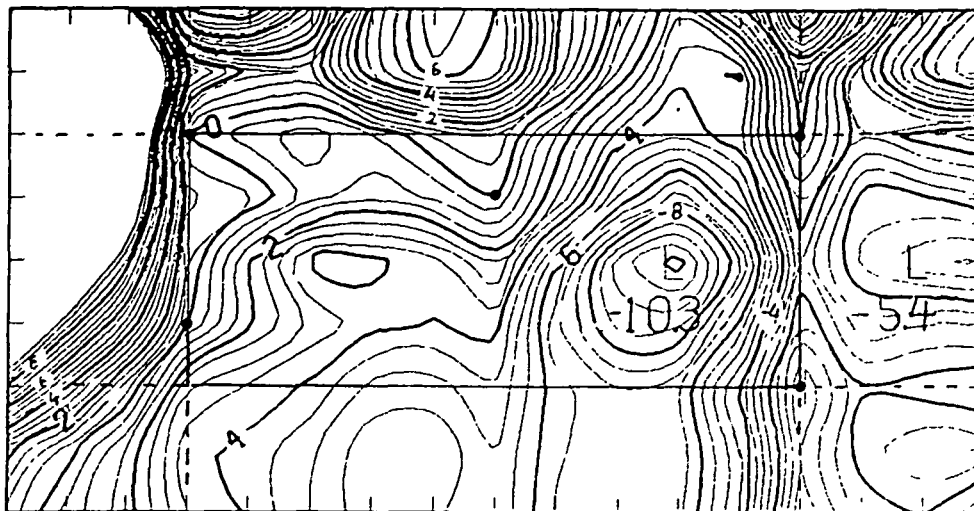


Fig. 11b

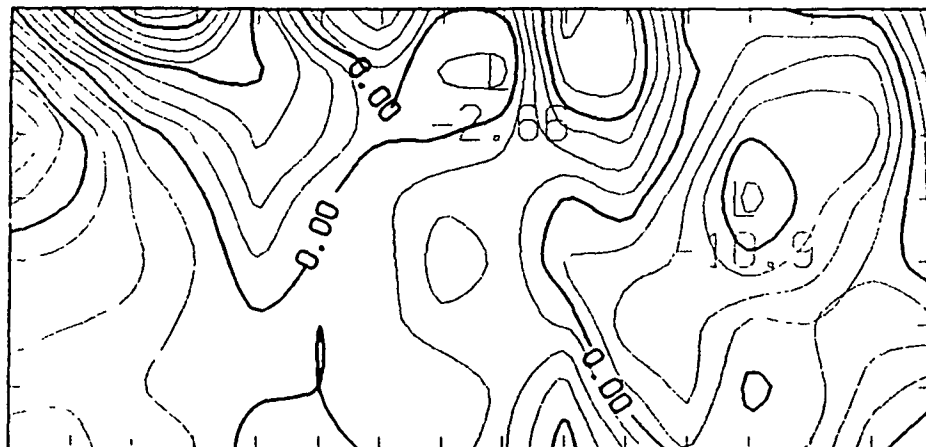
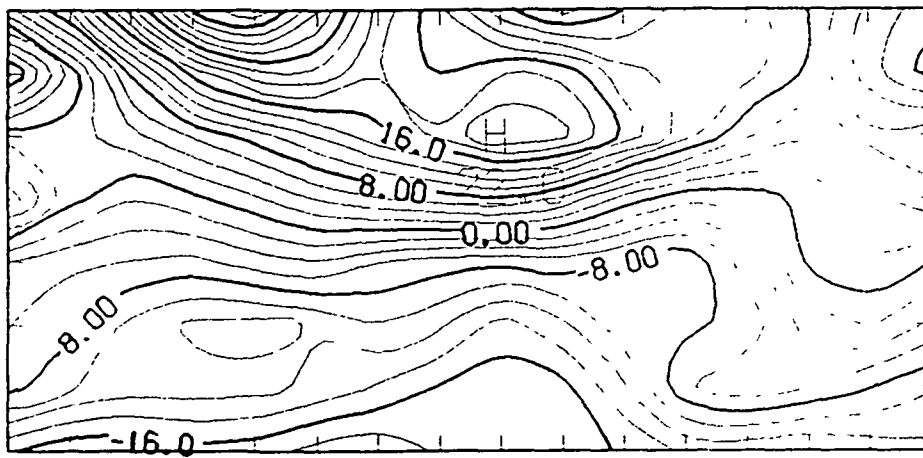
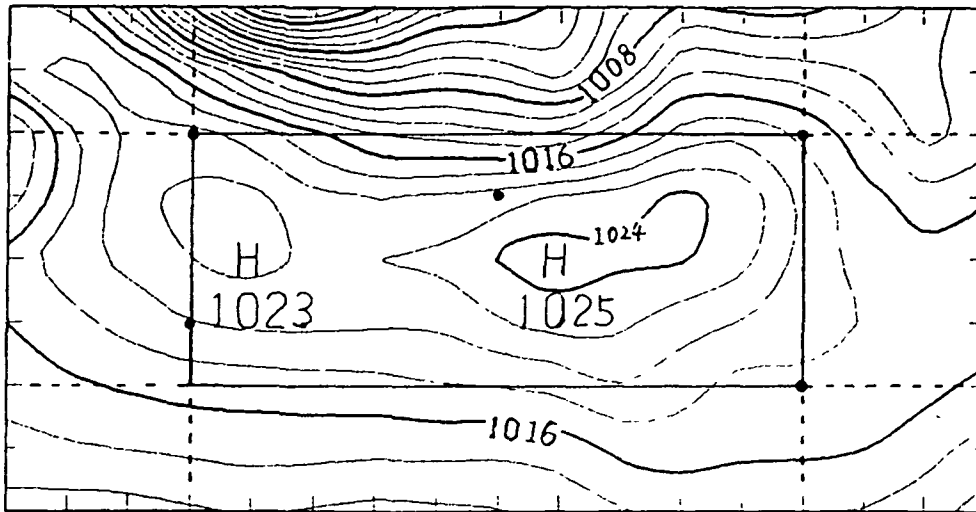


Fig. 12

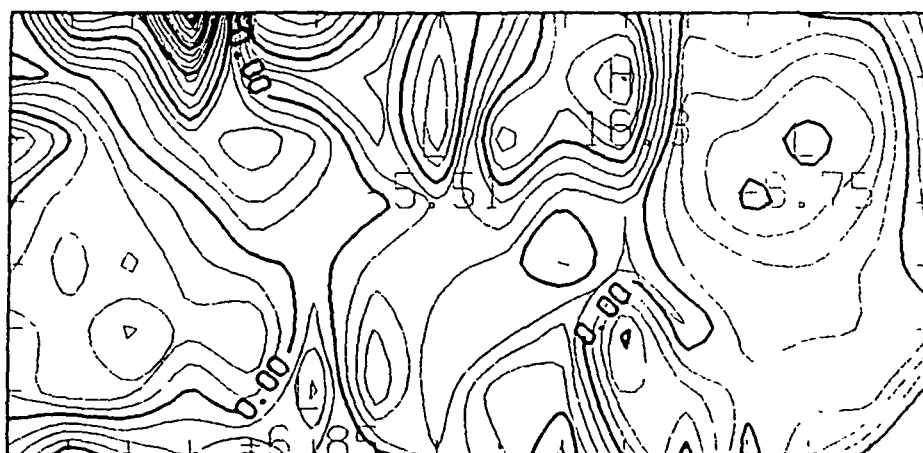
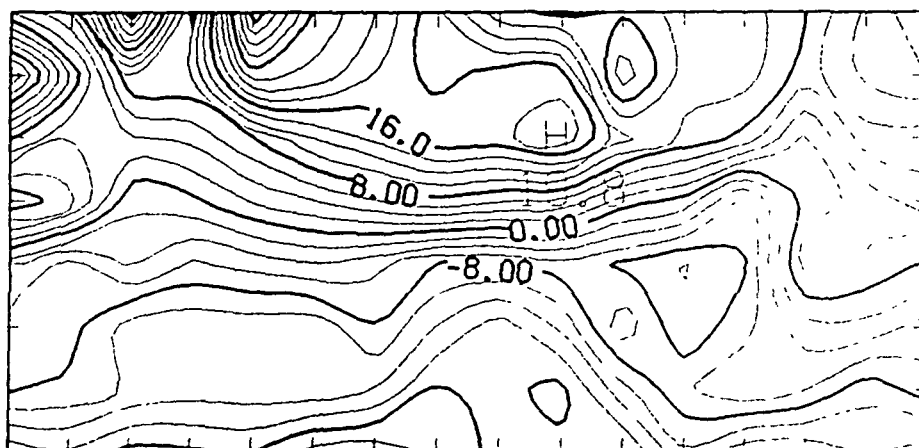
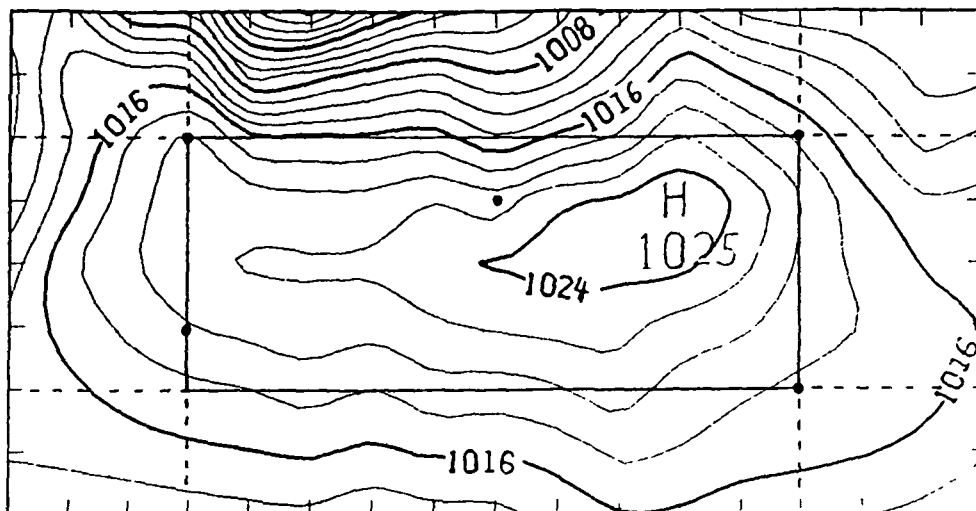


Fig. 13a

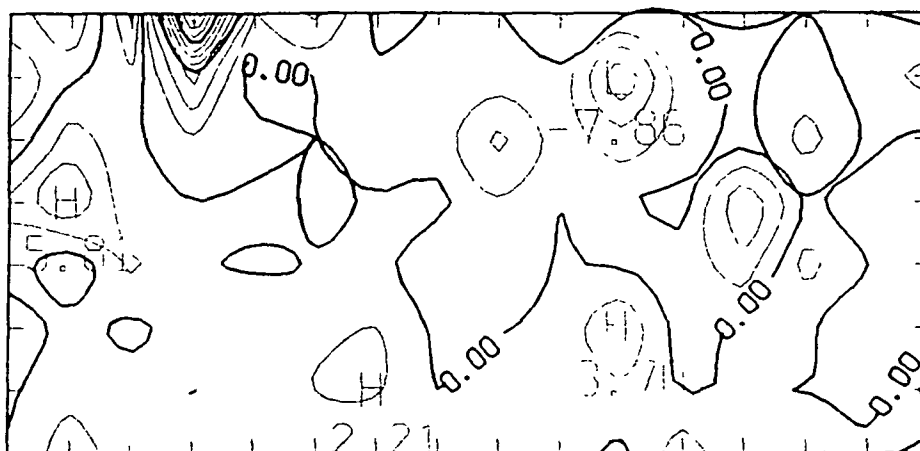
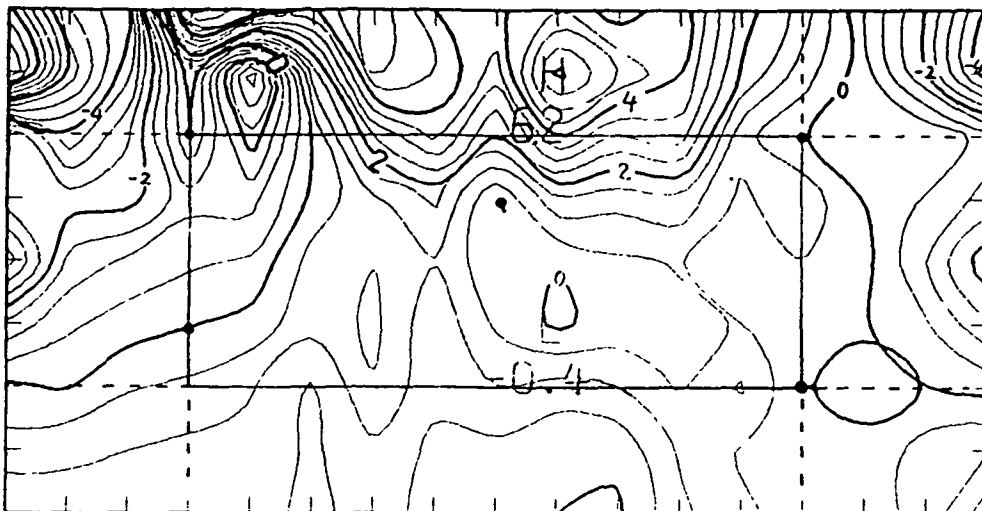


Fig. 13b

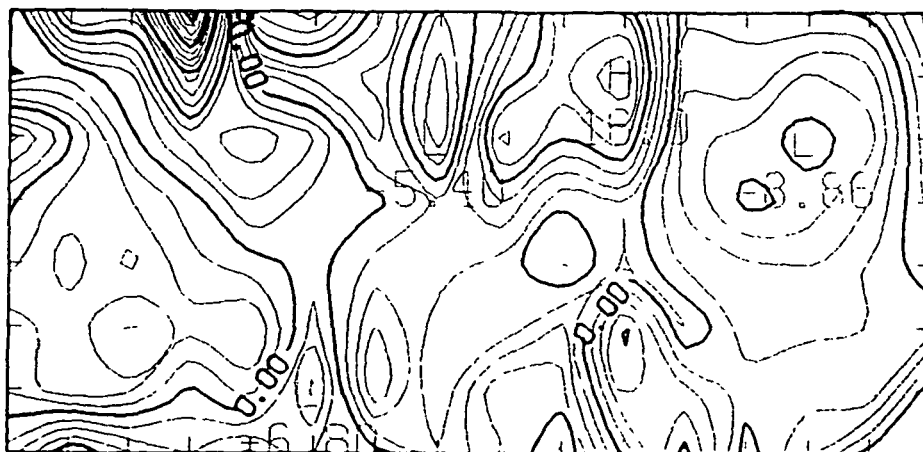
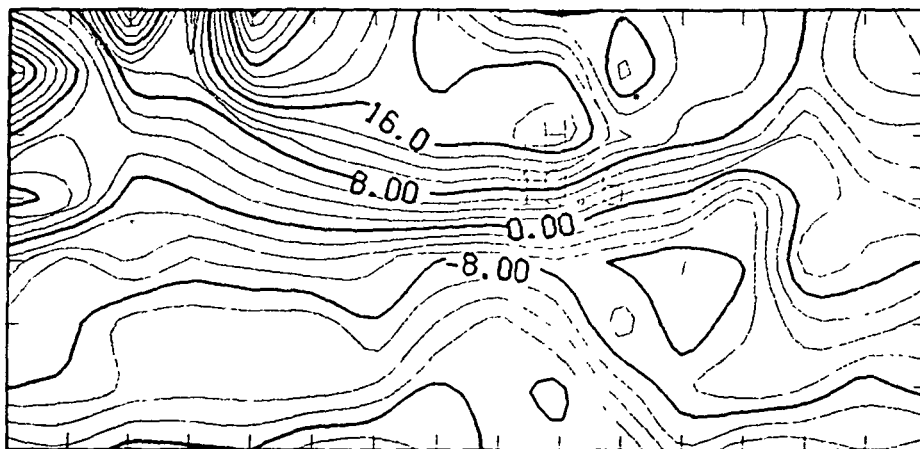
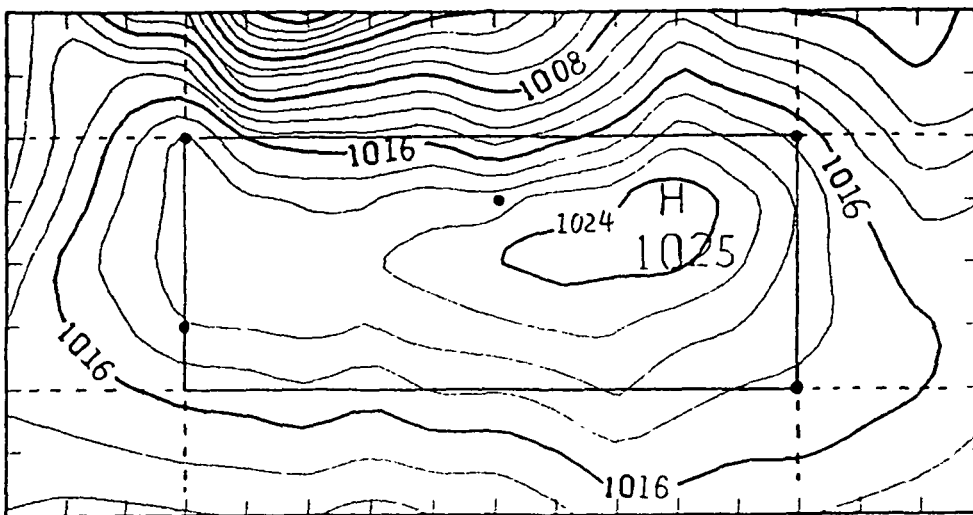


Fig. 14a

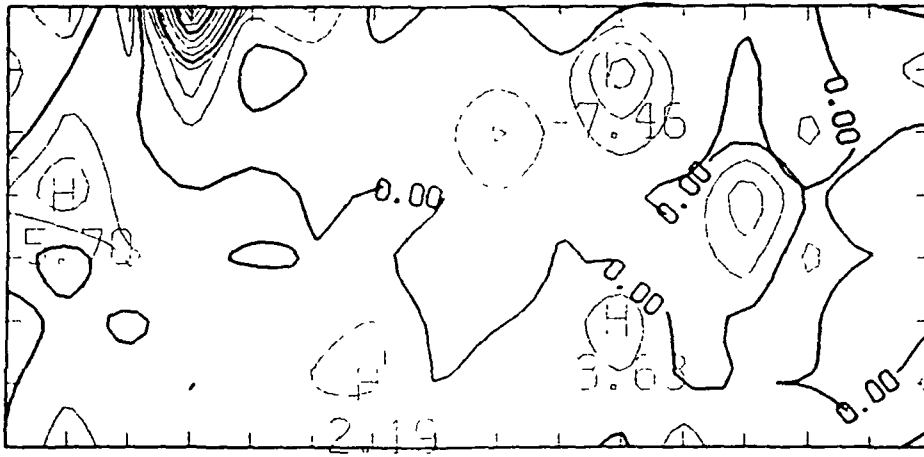
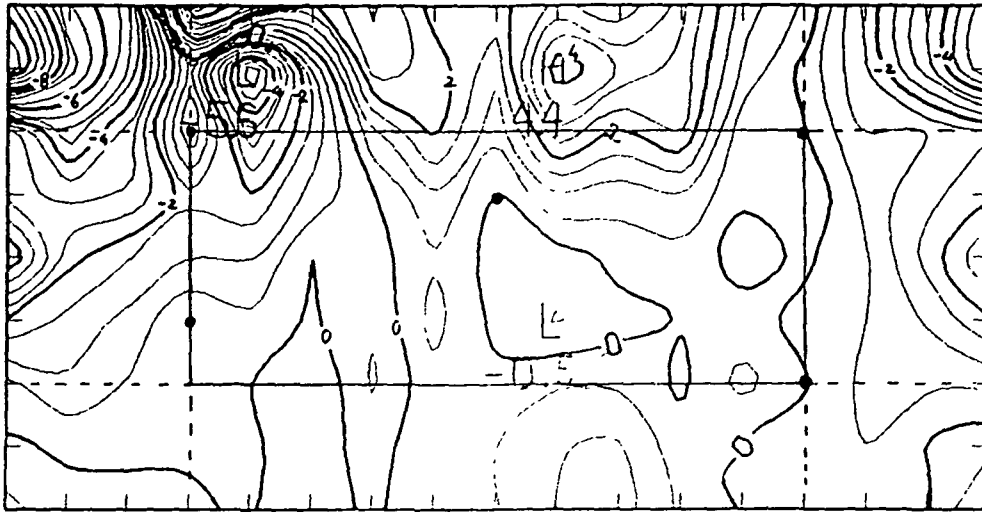


Fig. 14b

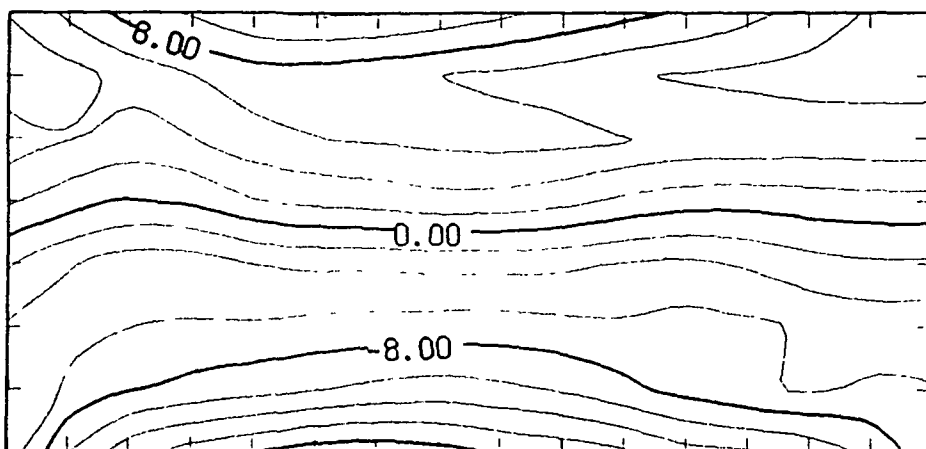
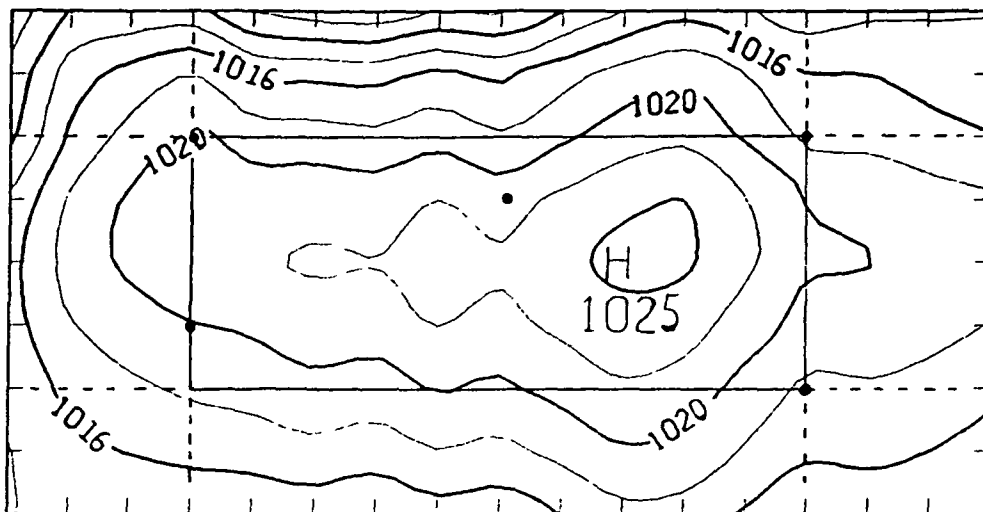


Fig. 15a

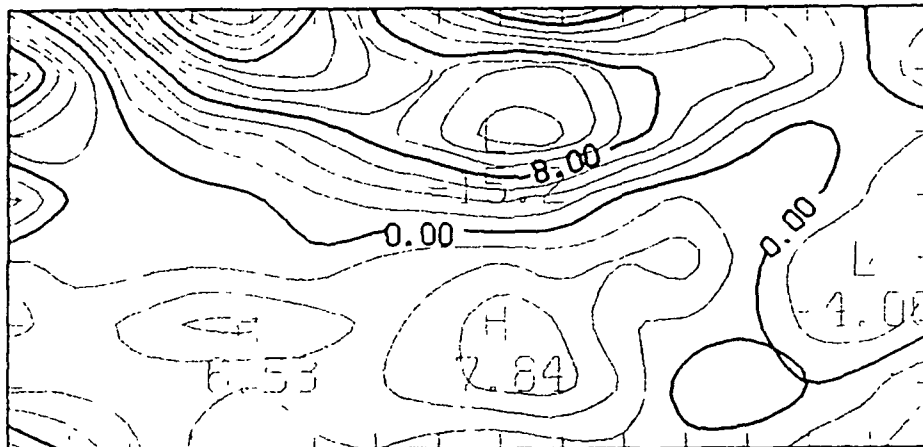
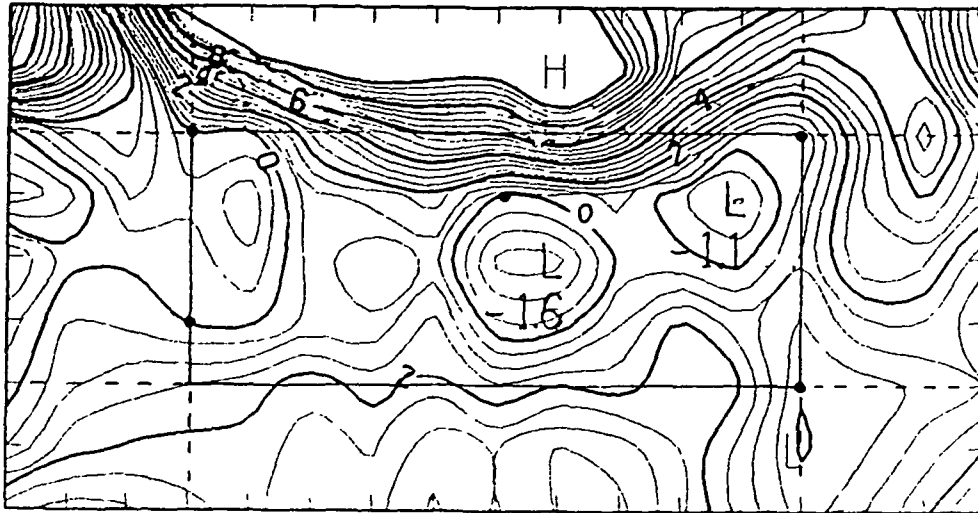


Fig. 15b

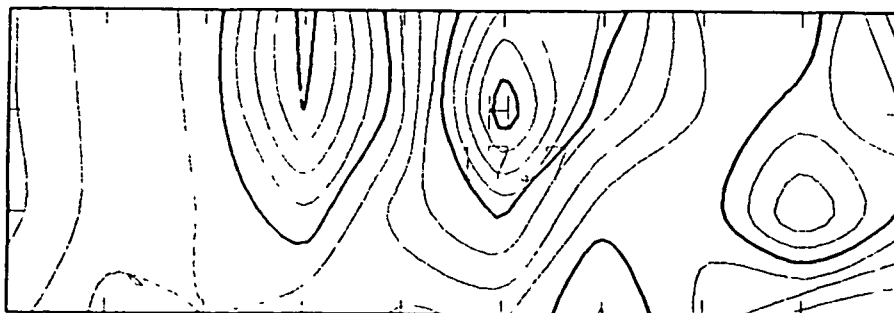
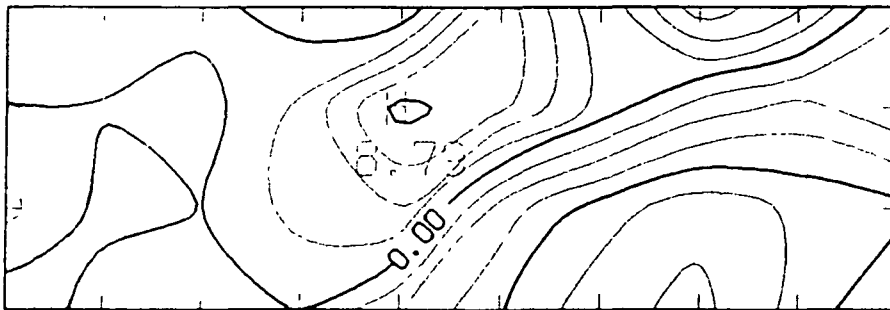
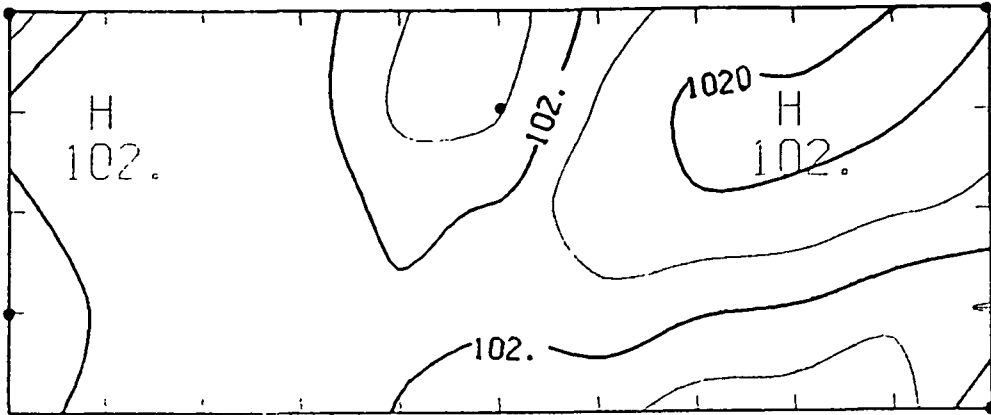


Fig. 16a

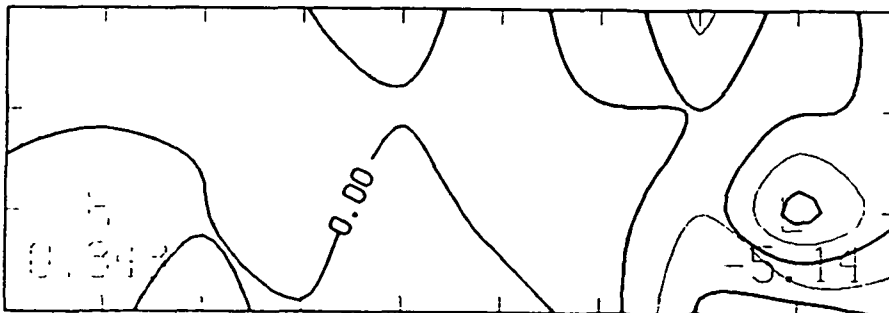
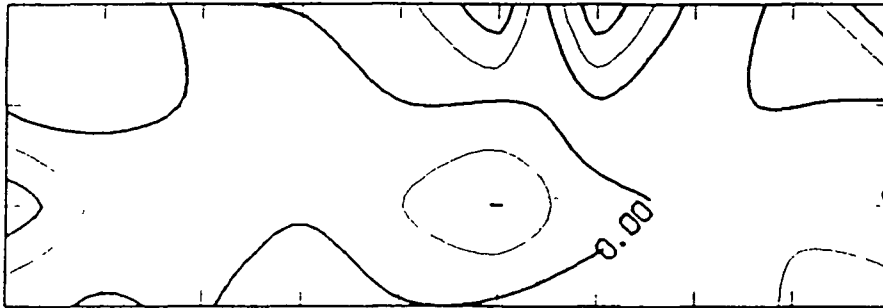
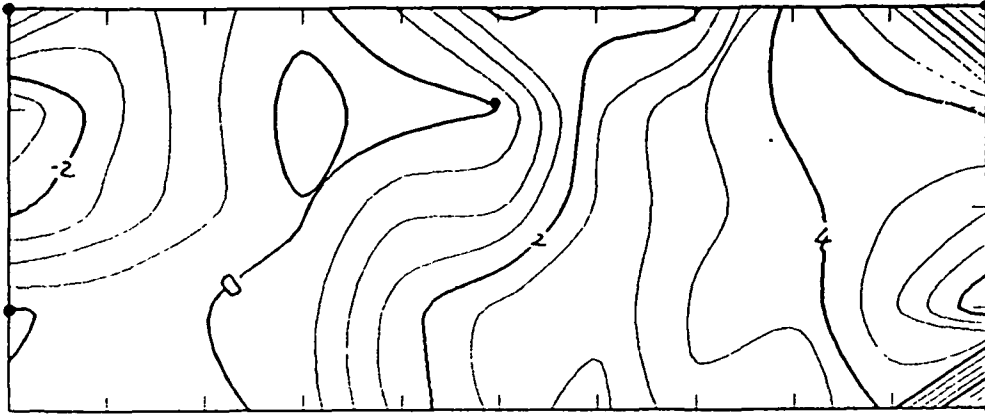


Fig. 16b

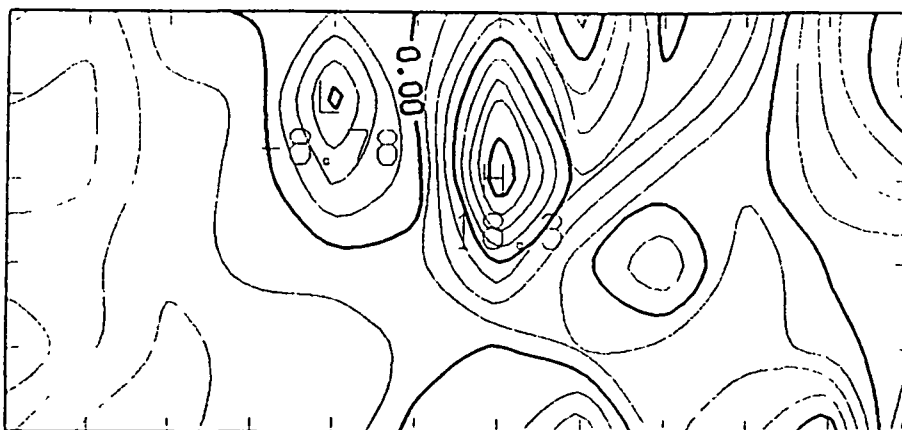
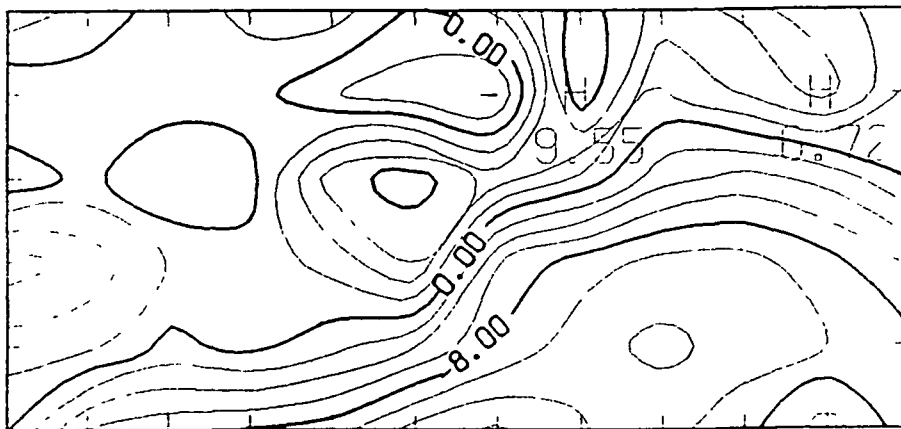
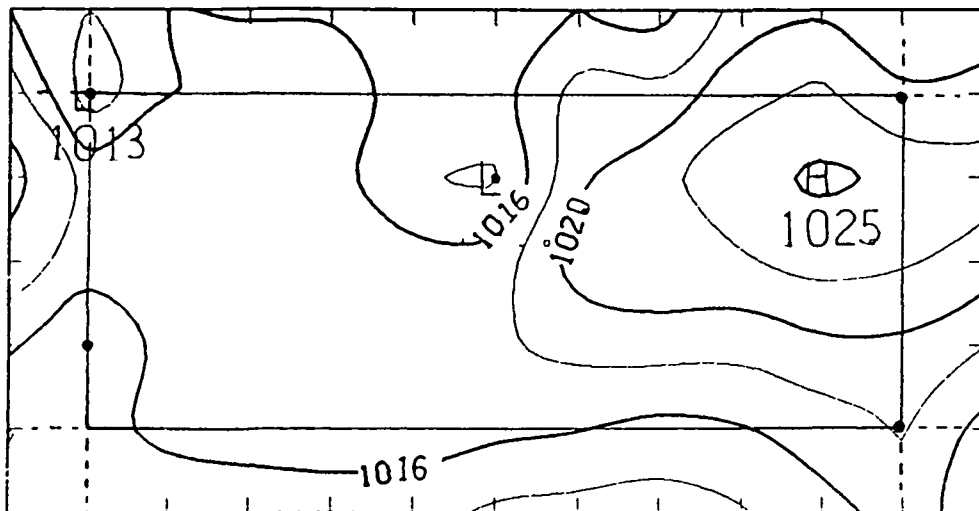


Fig. 17a

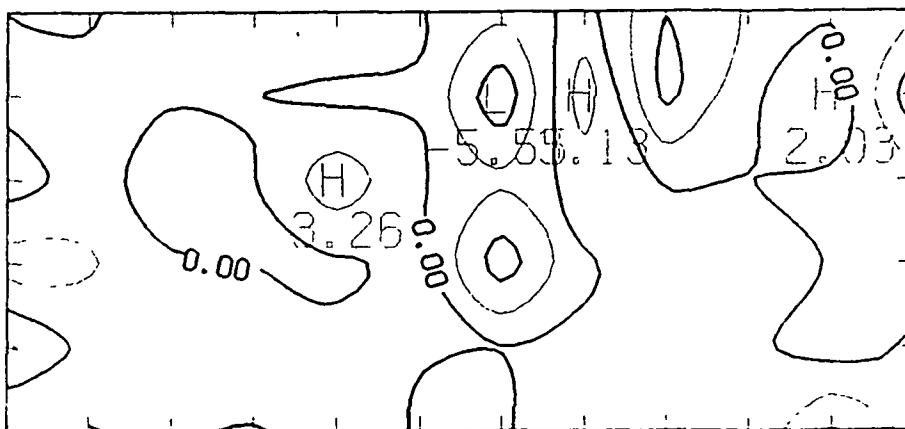
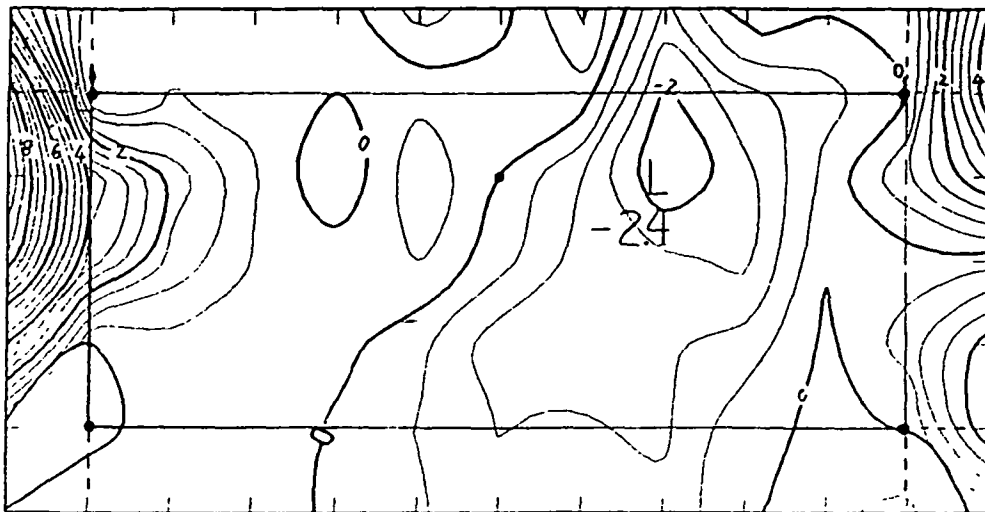


Fig. 17b

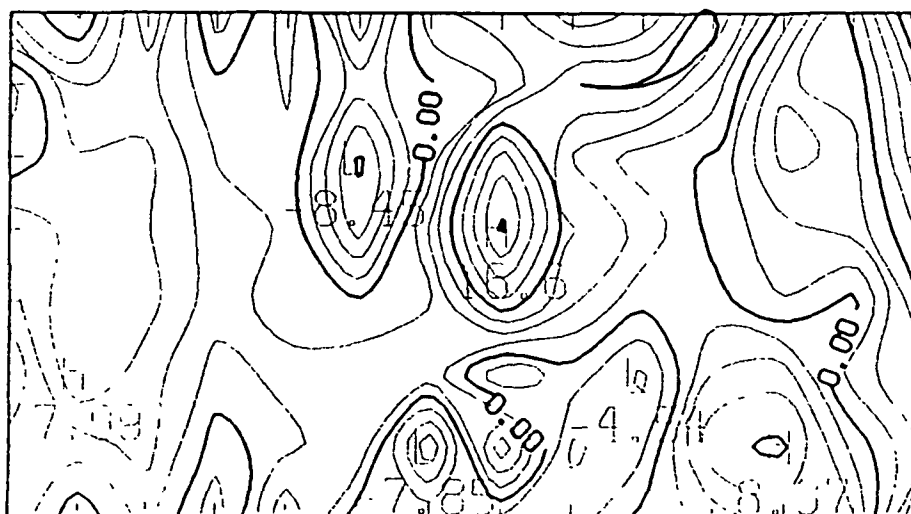
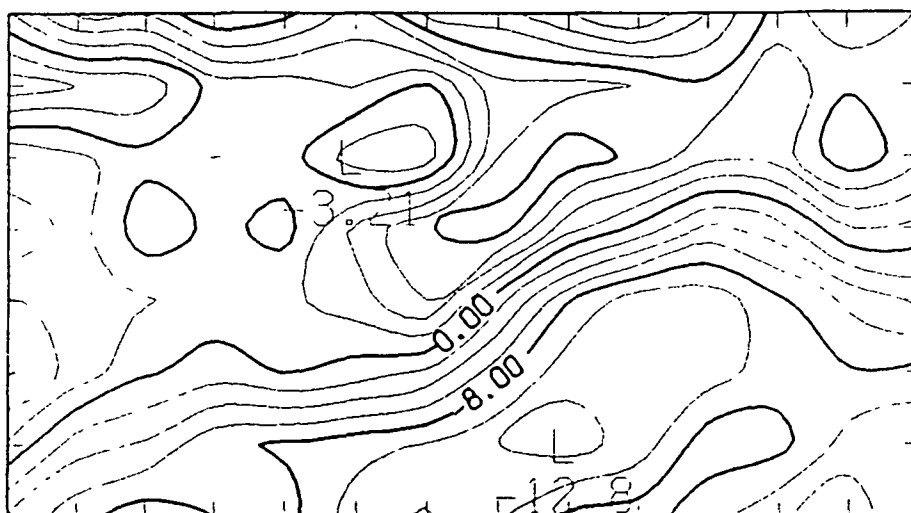
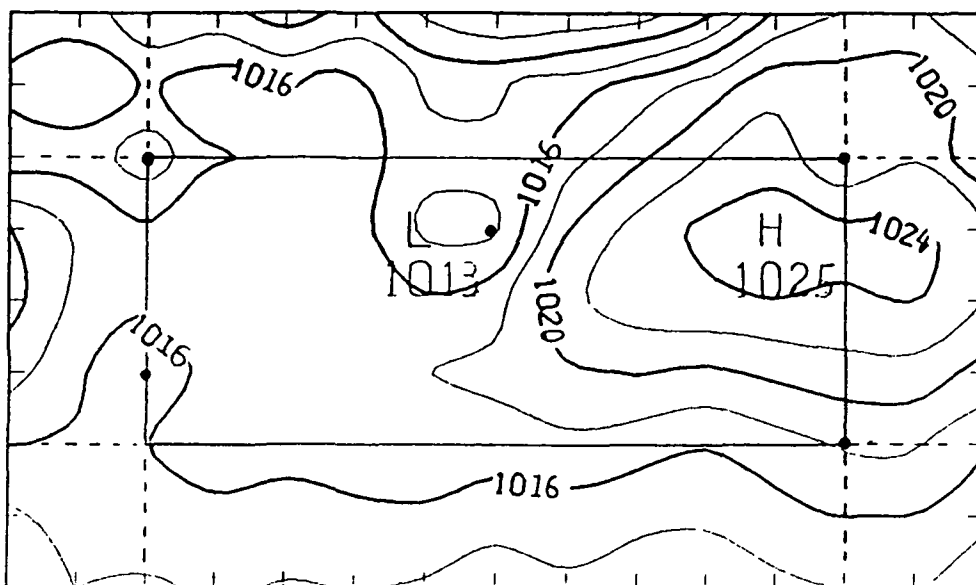


Fig. 18a

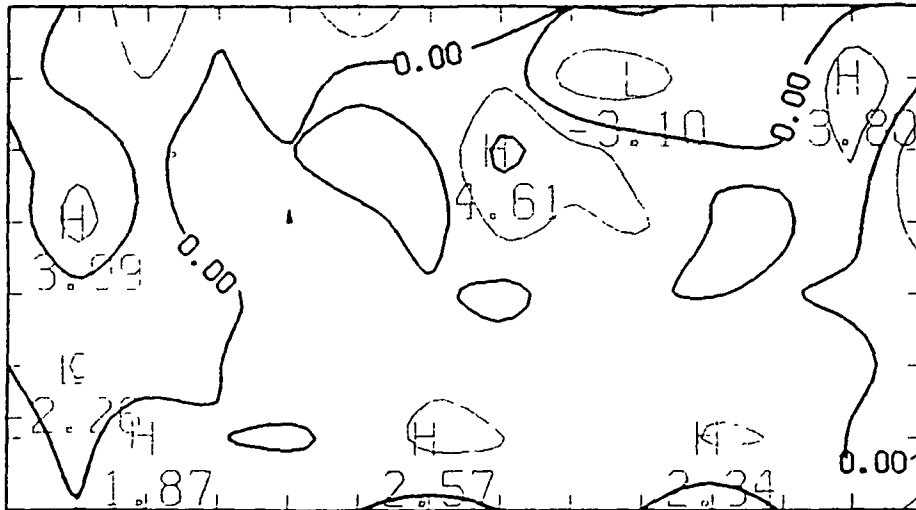


Fig. 18b

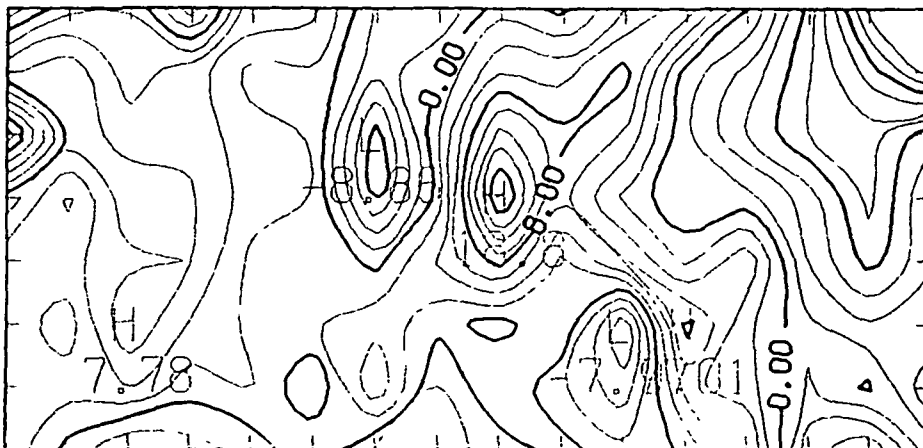
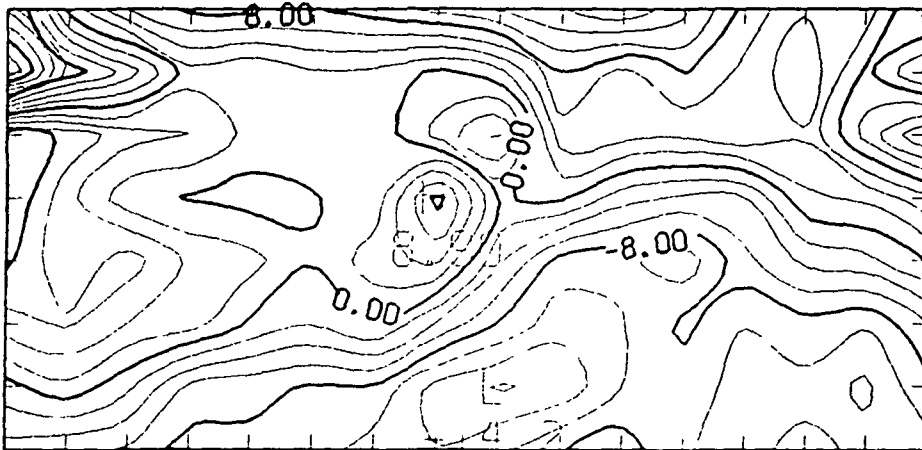
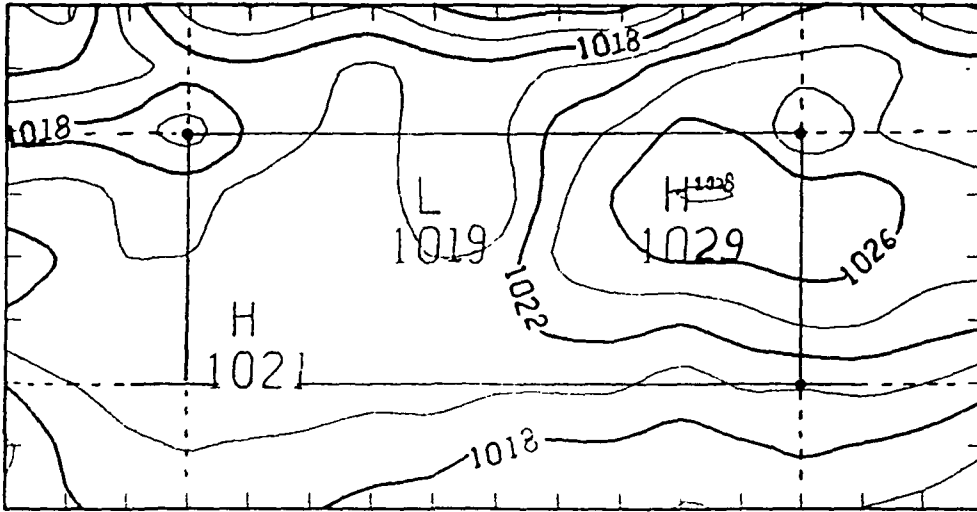


Fig. 19a

ORIGINAL PAGE IS
OF POOR QUALITY

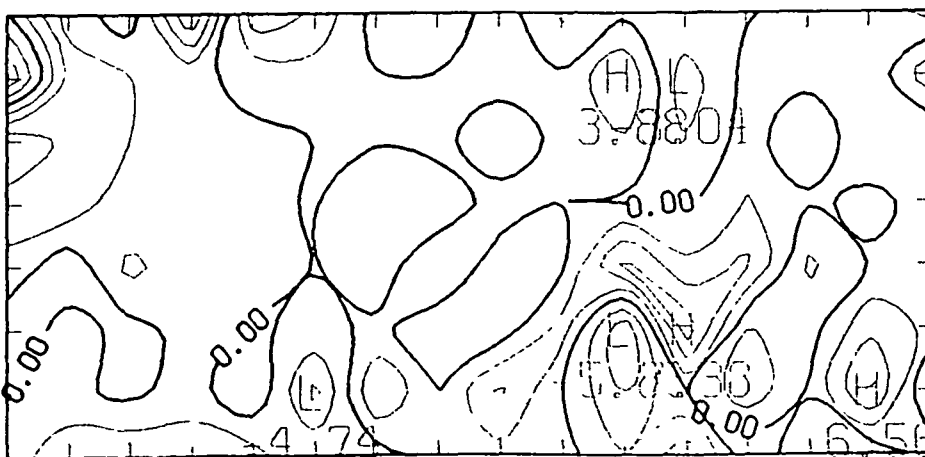
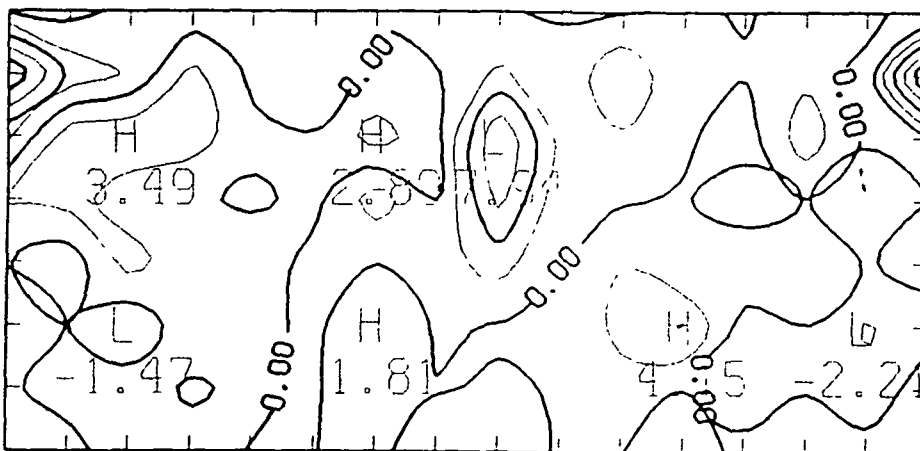
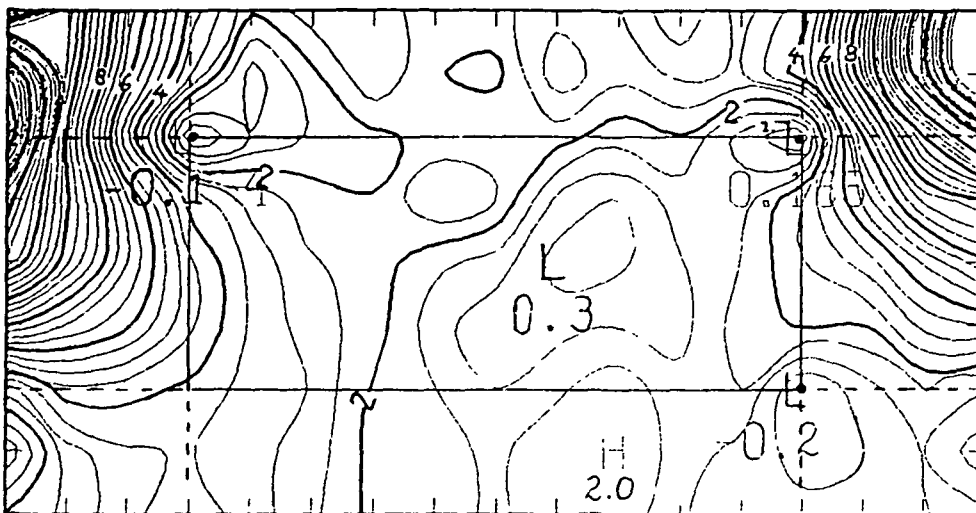


Fig. 19b

ORIGINAL PAGE IS
OF POOR QUALITY

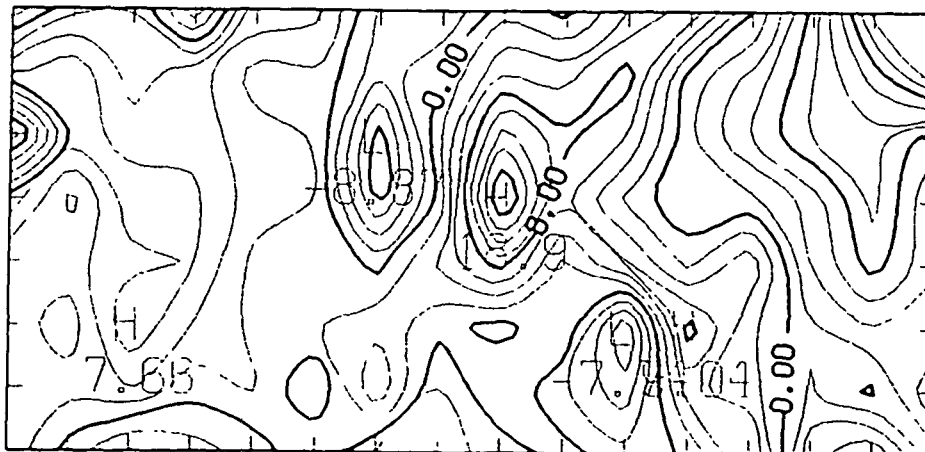
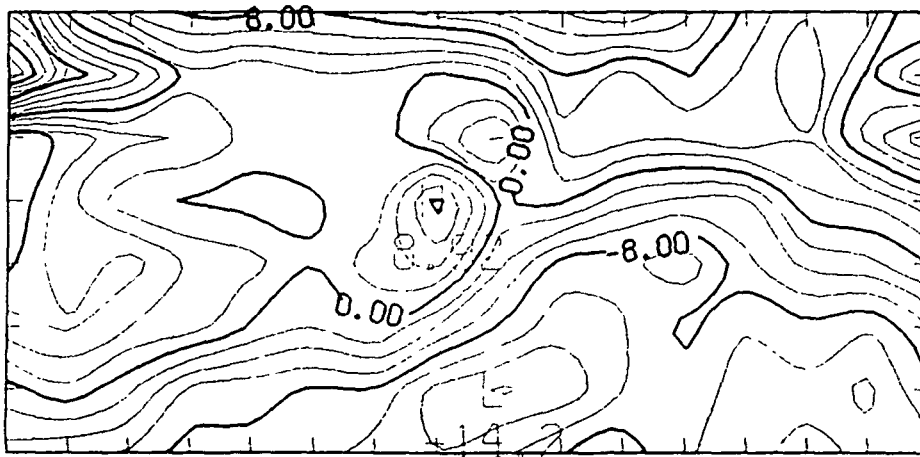
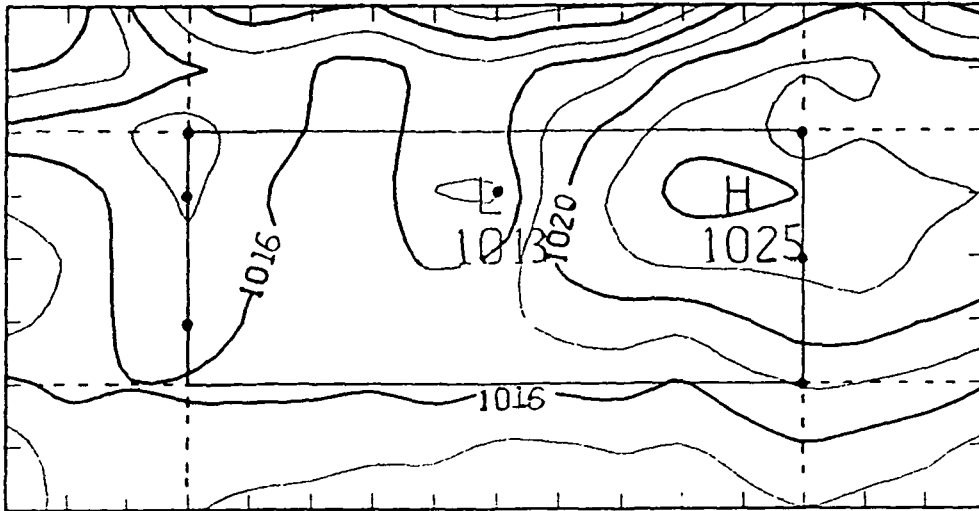


Fig. 20a

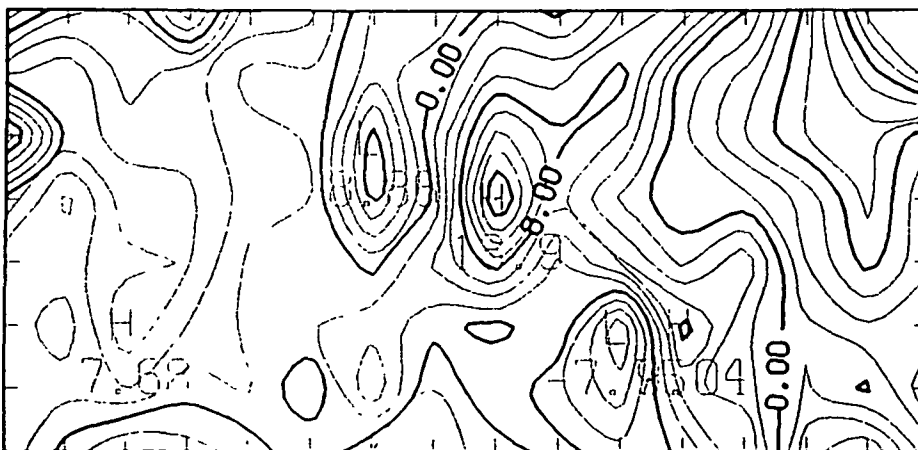
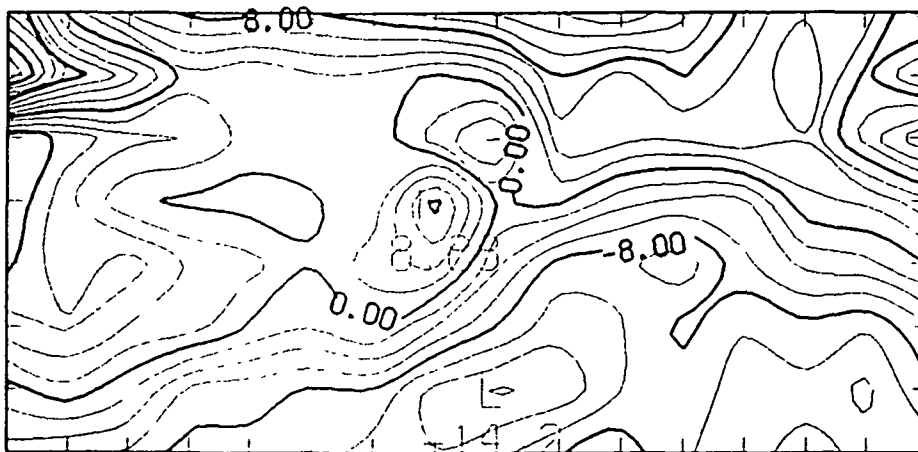
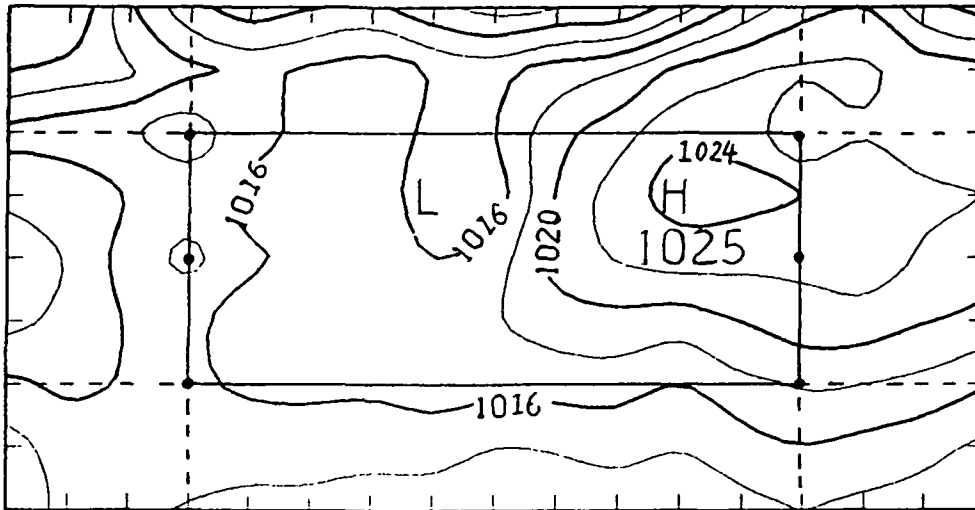


Fig. 21a

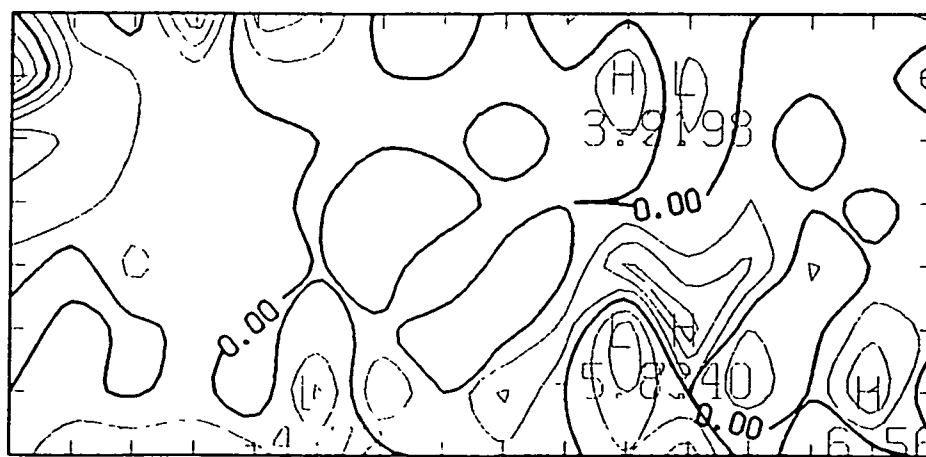
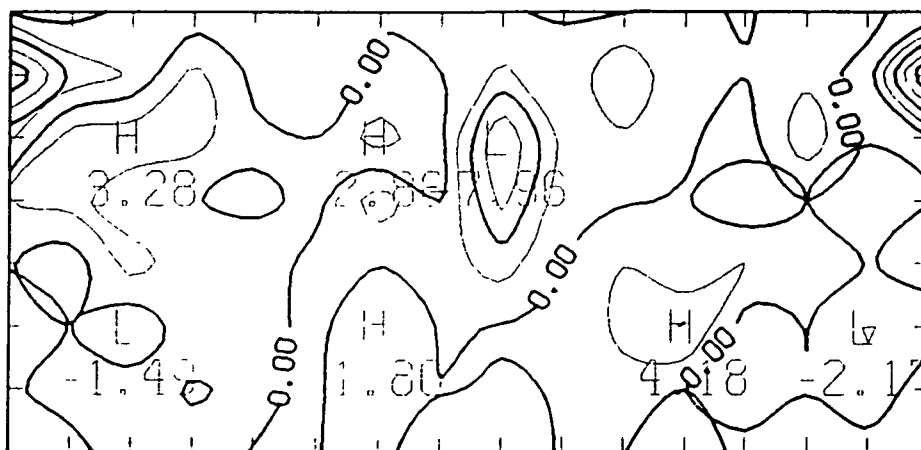
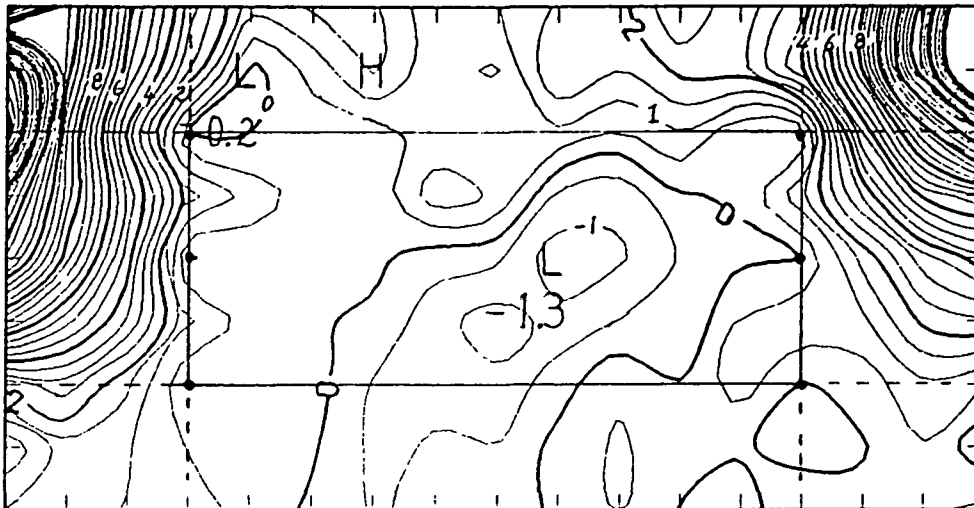


Fig. 21b

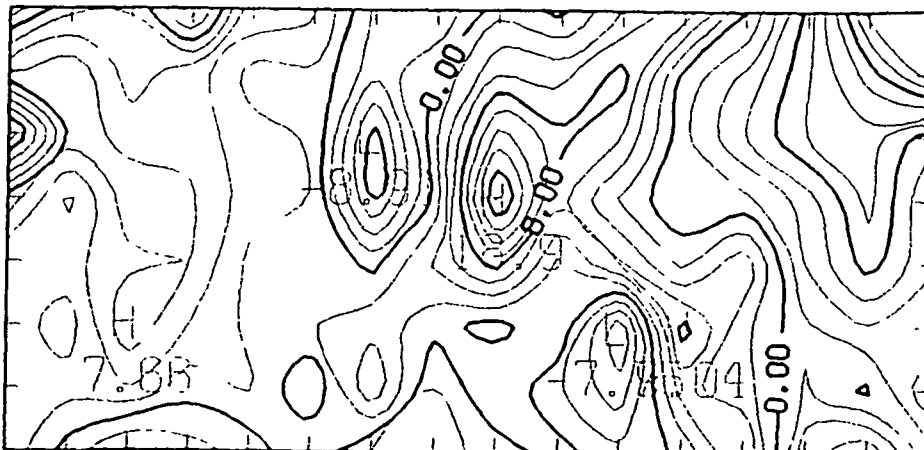
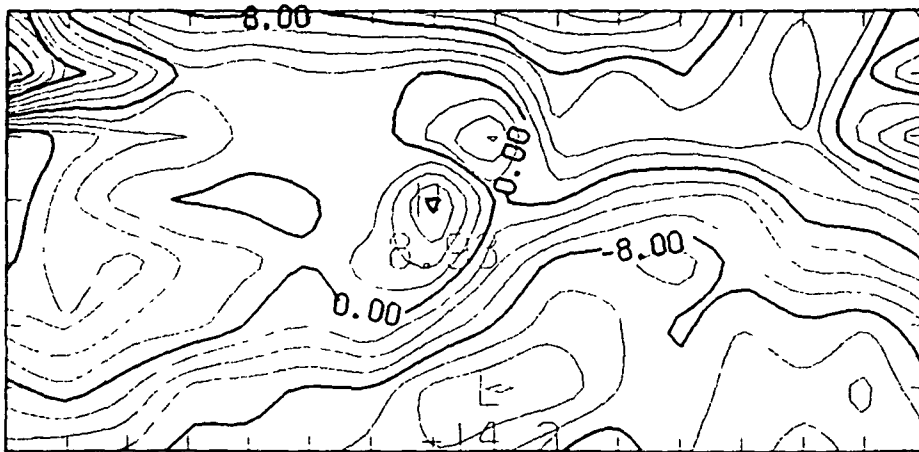
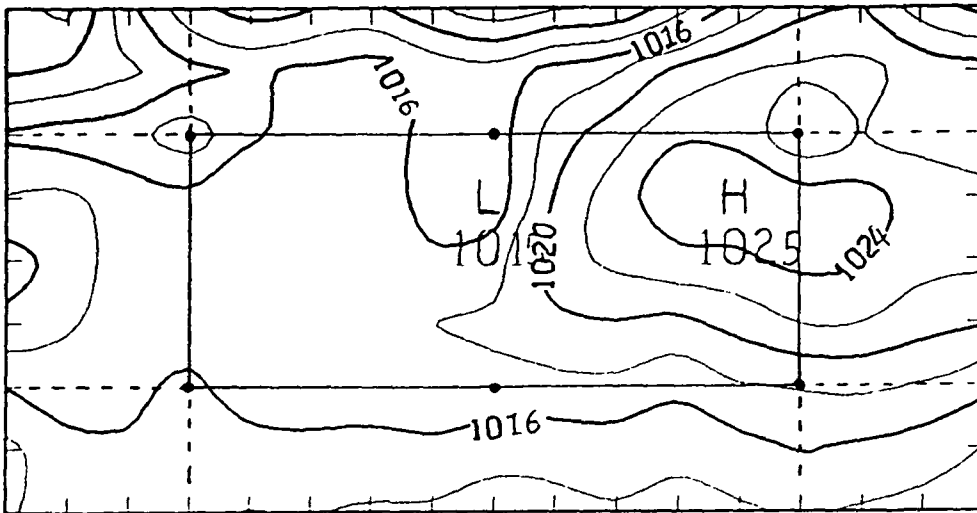


Fig. 22a

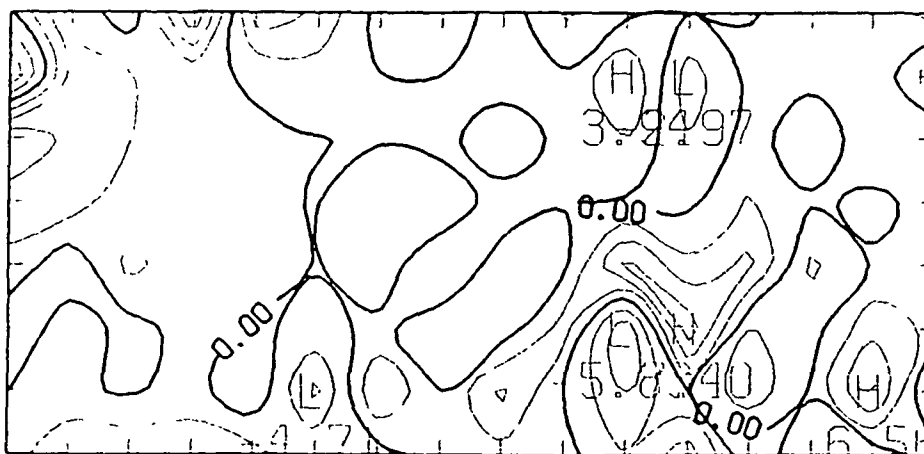
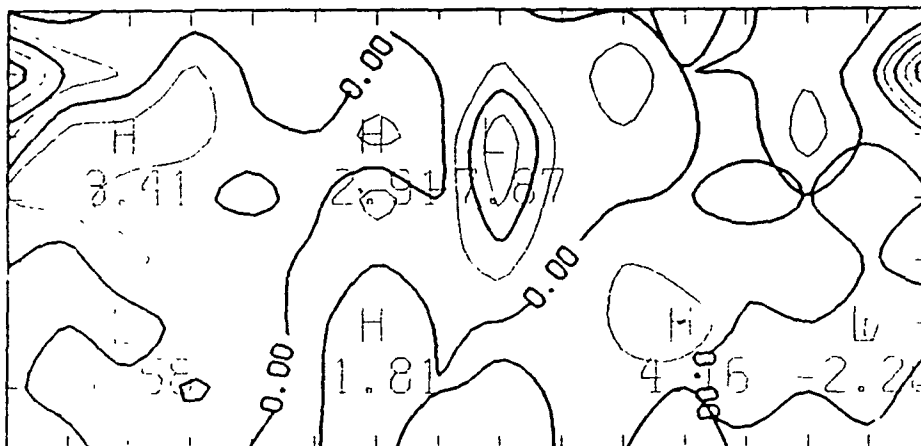
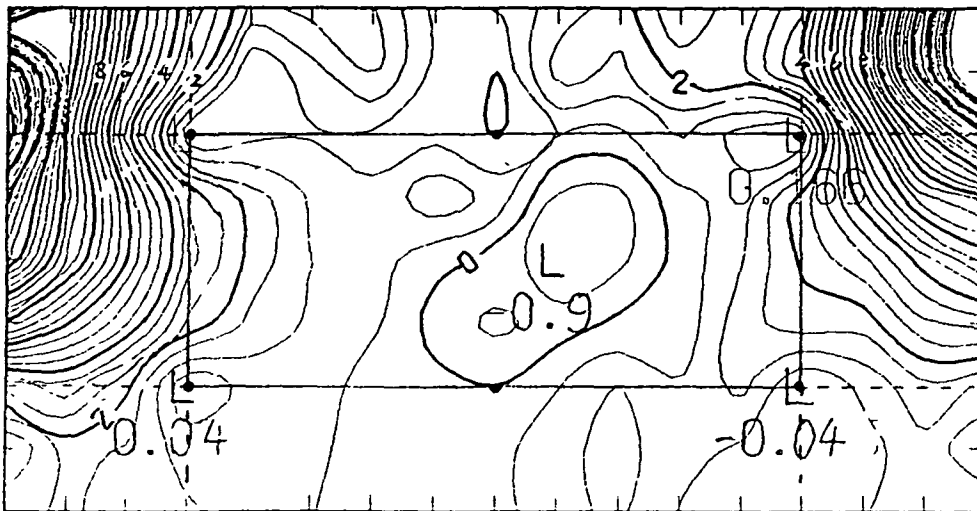


Fig. 22b

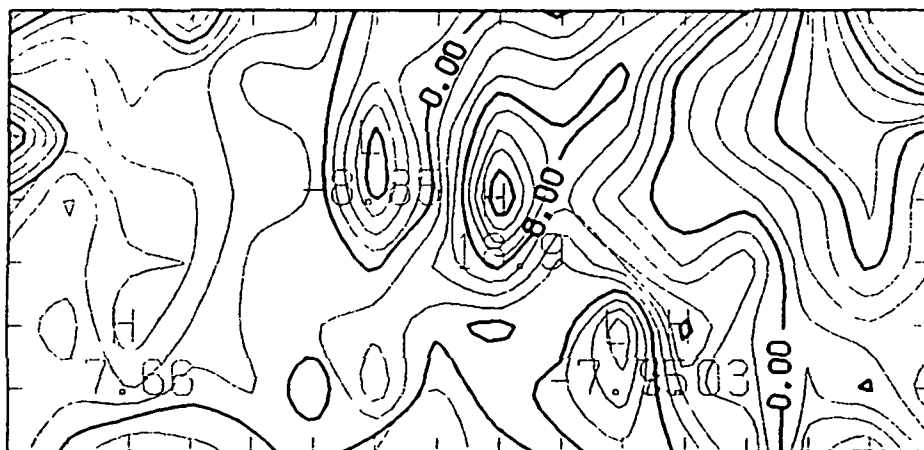
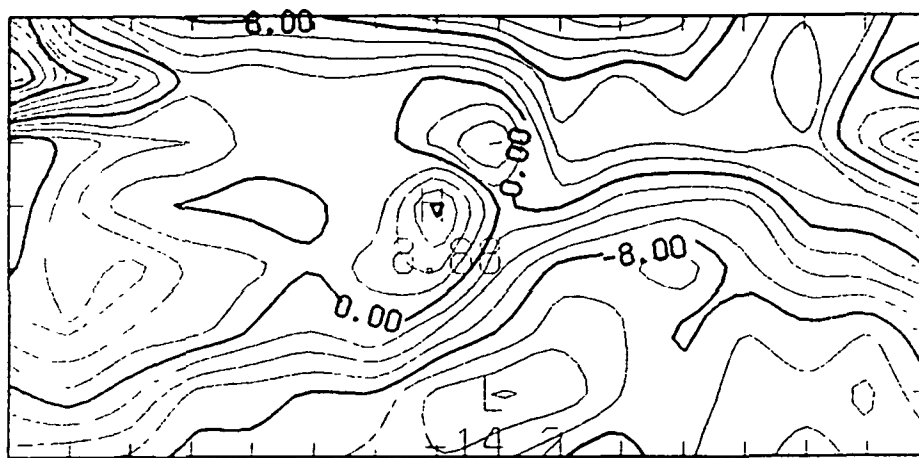
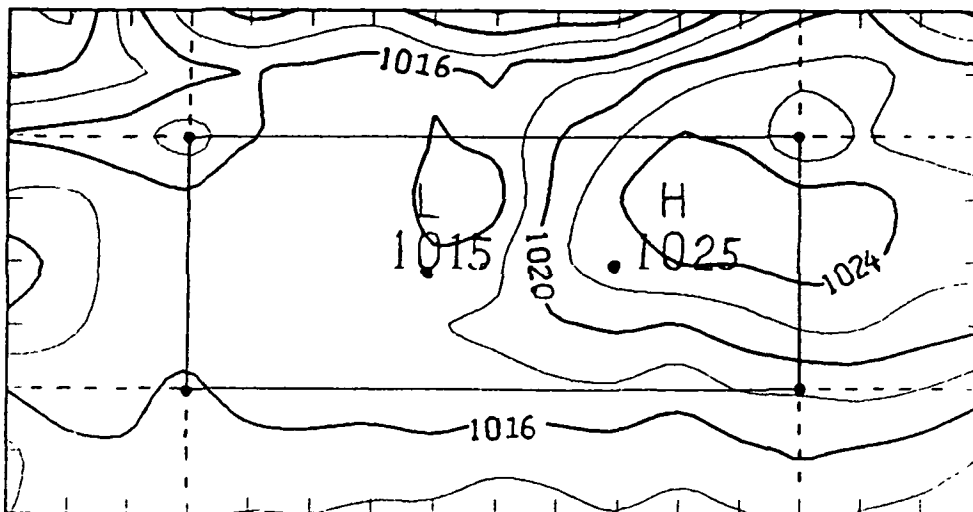


Fig. 23a

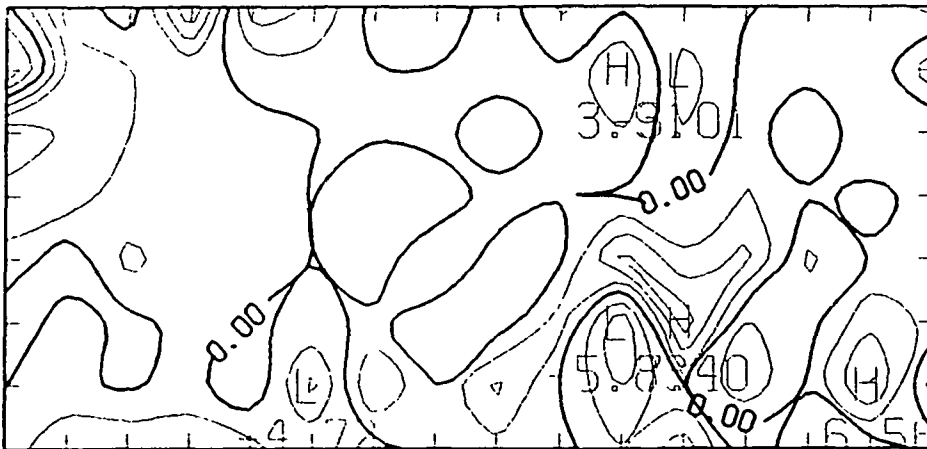
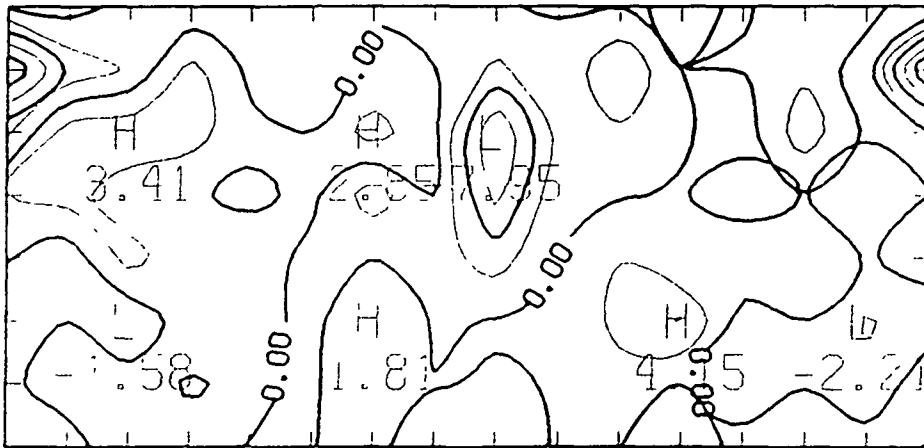
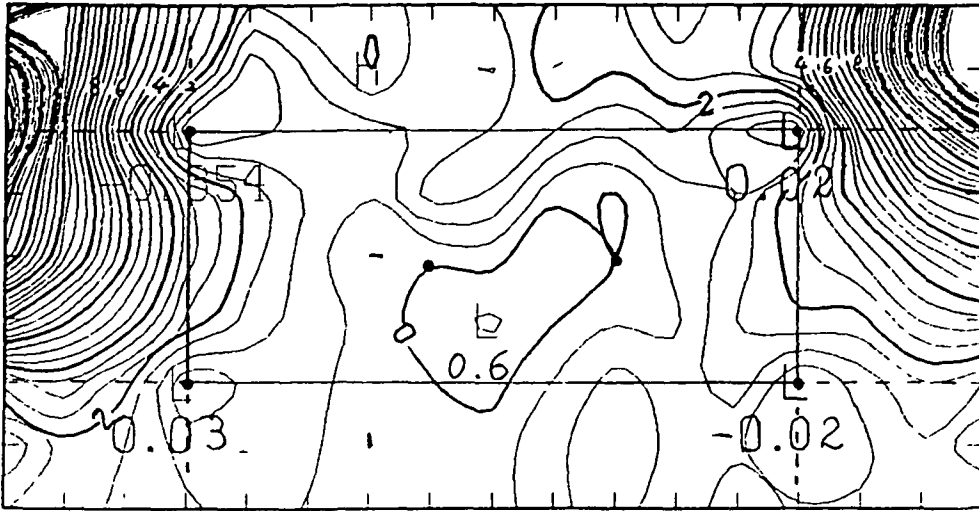


Fig. 23b

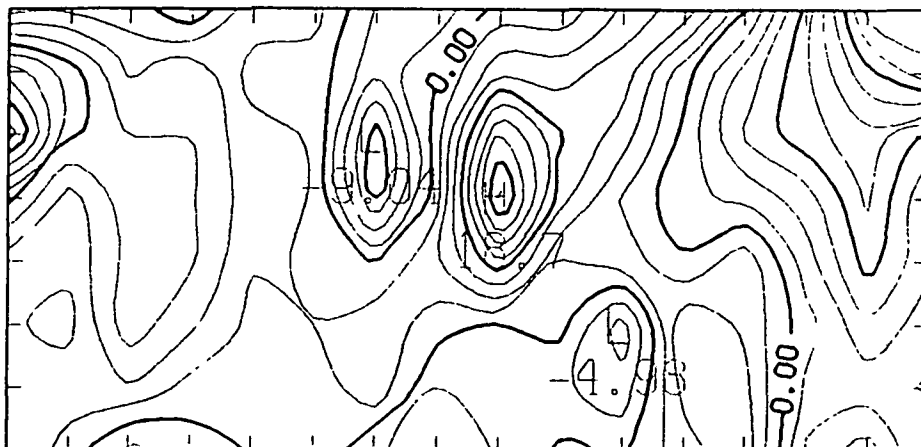
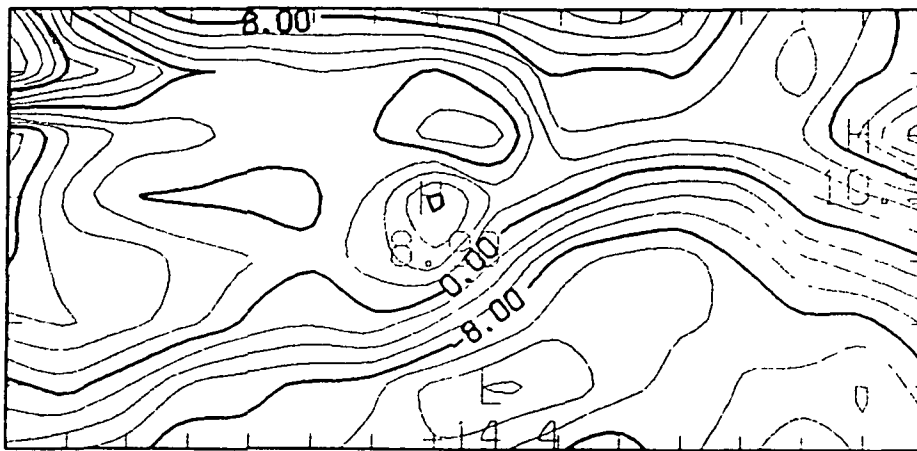
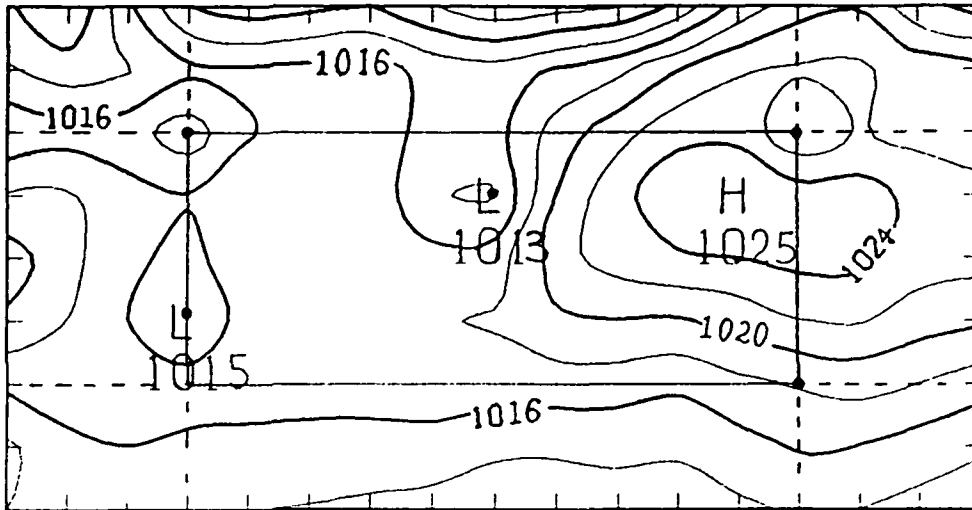


Fig 24a

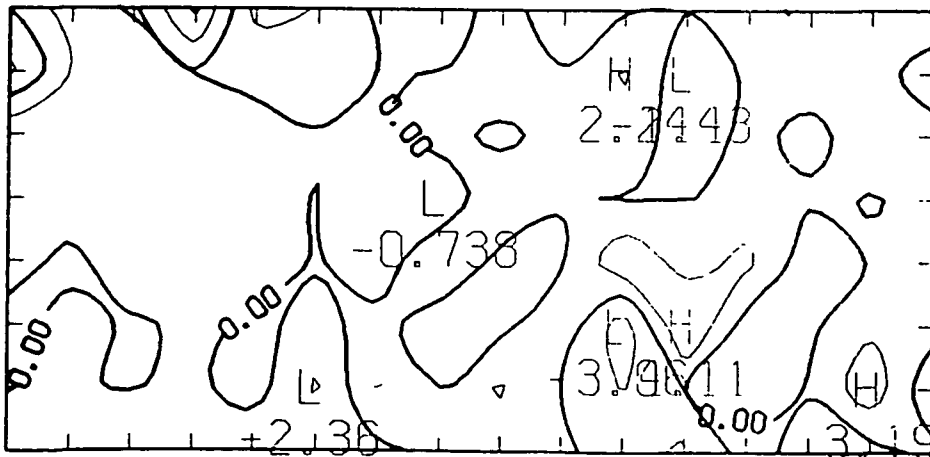
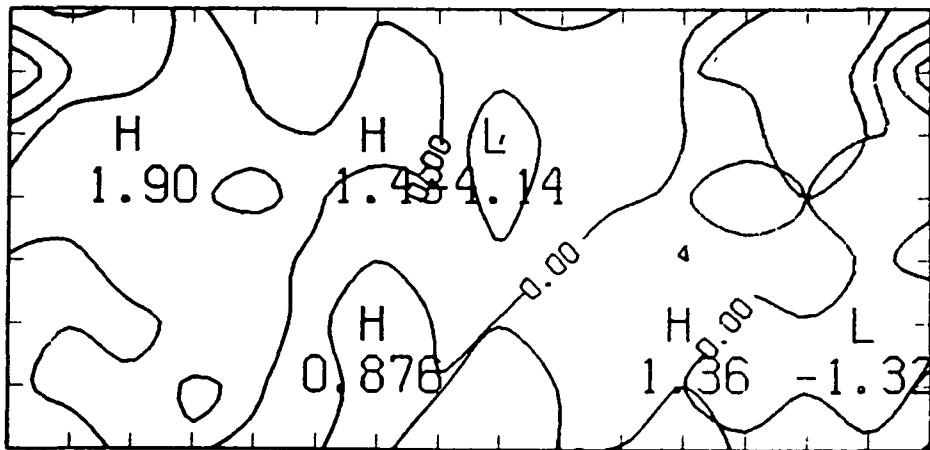
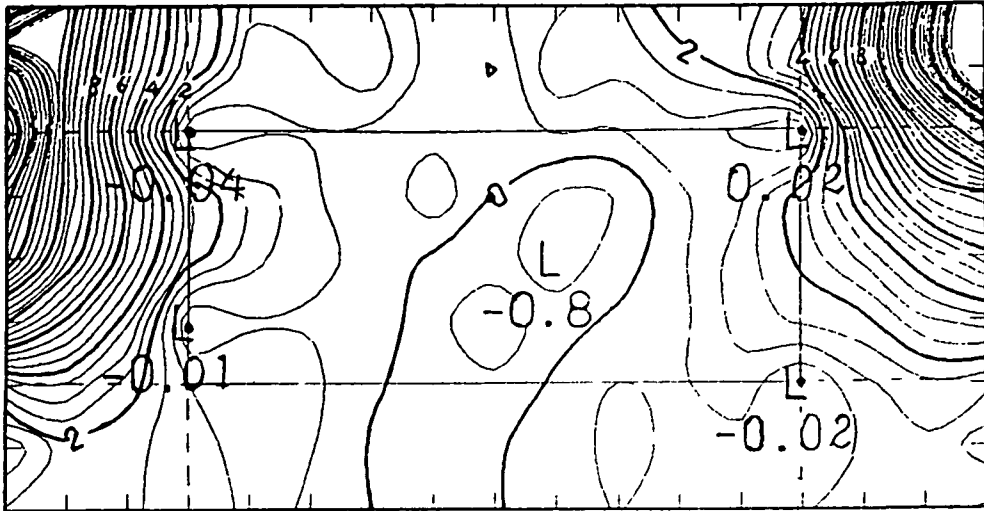


Fig. 24b

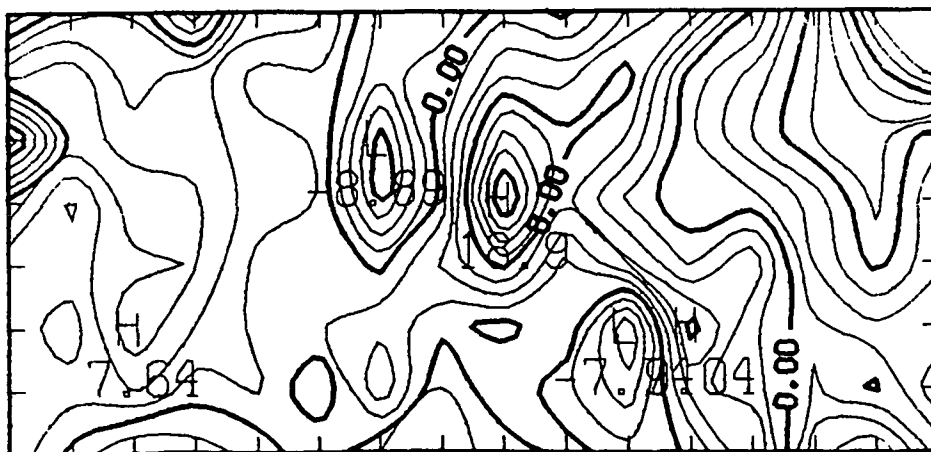
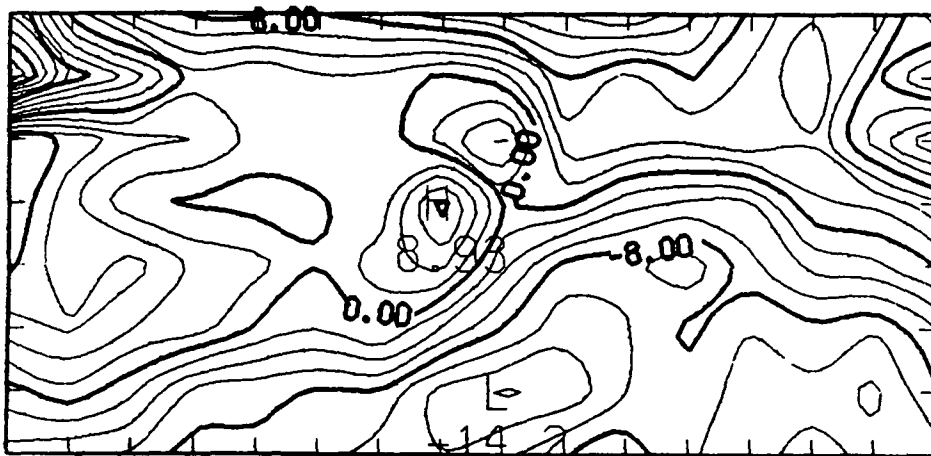
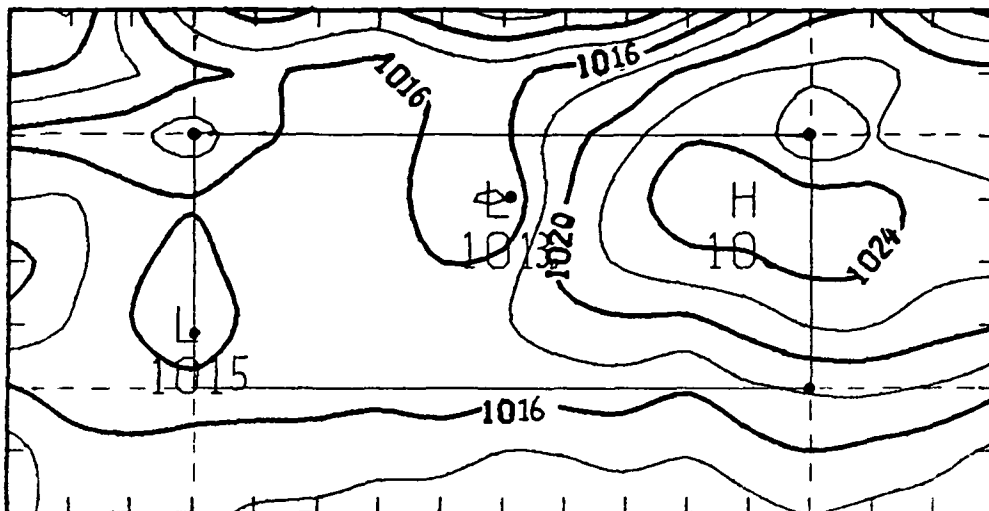


Fig. 25a

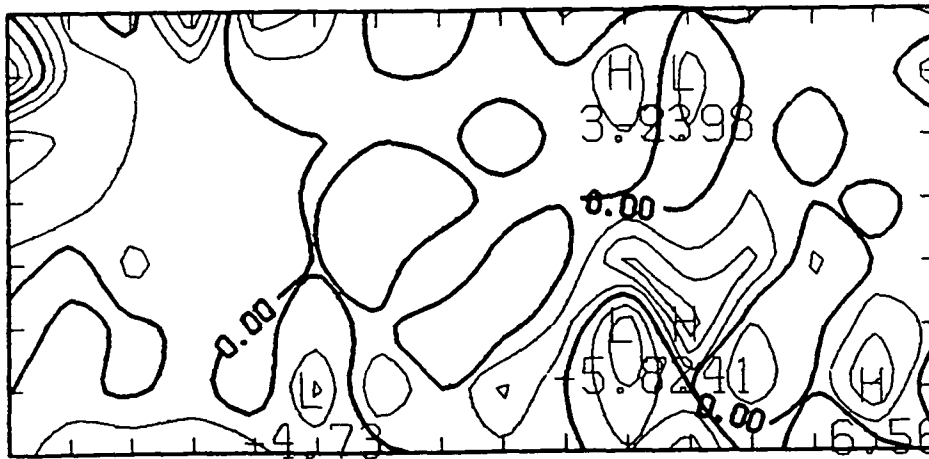
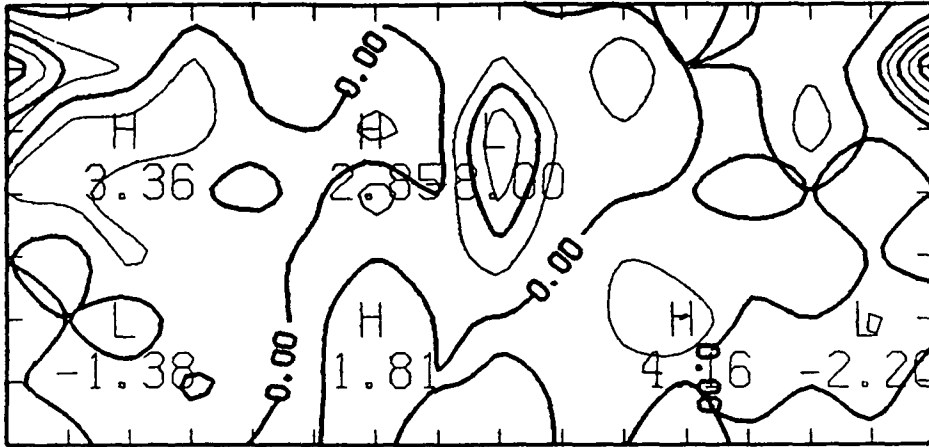
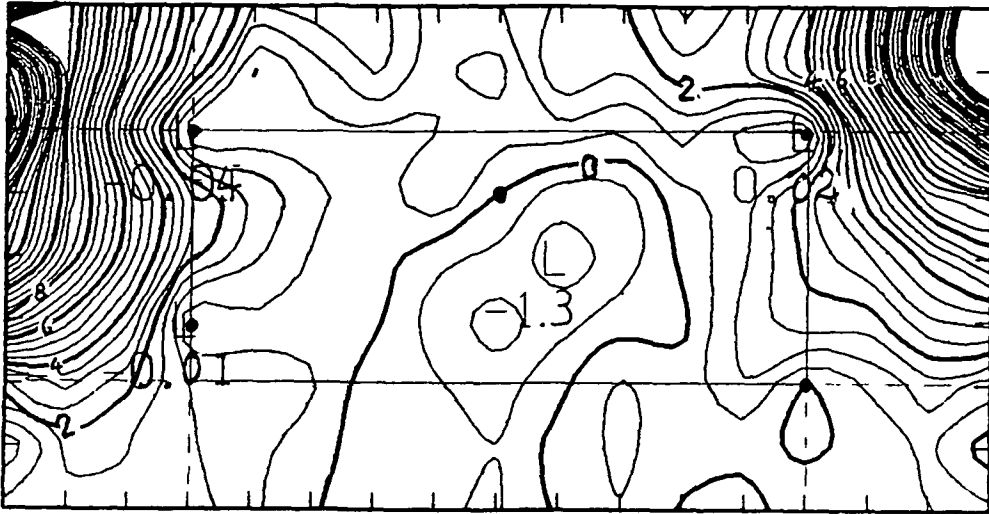


Fig 25b

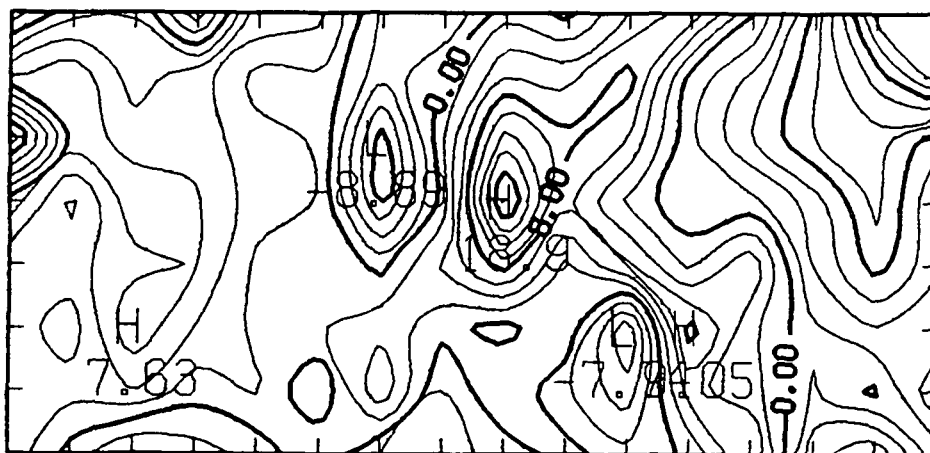
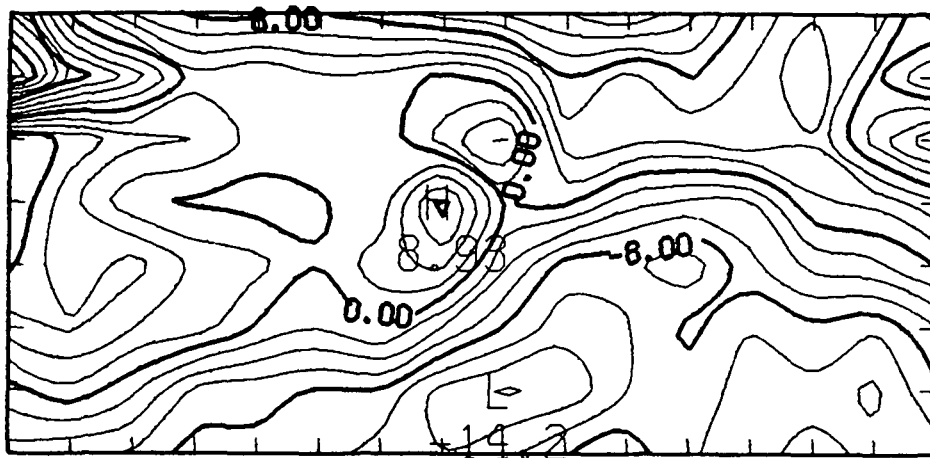
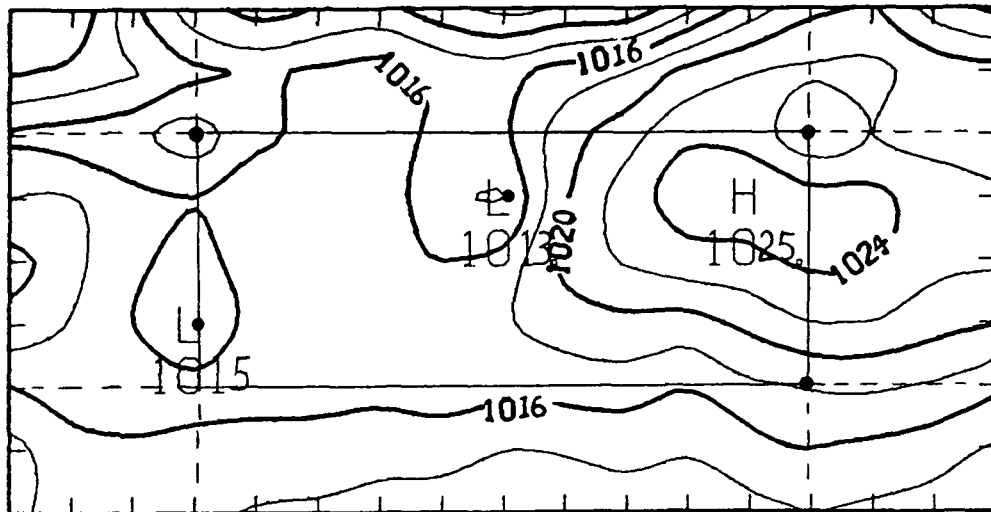


Fig. 26a

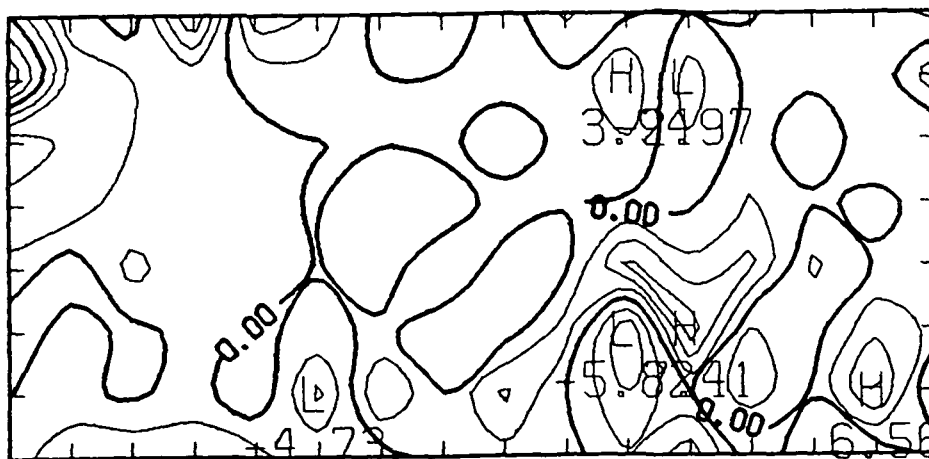
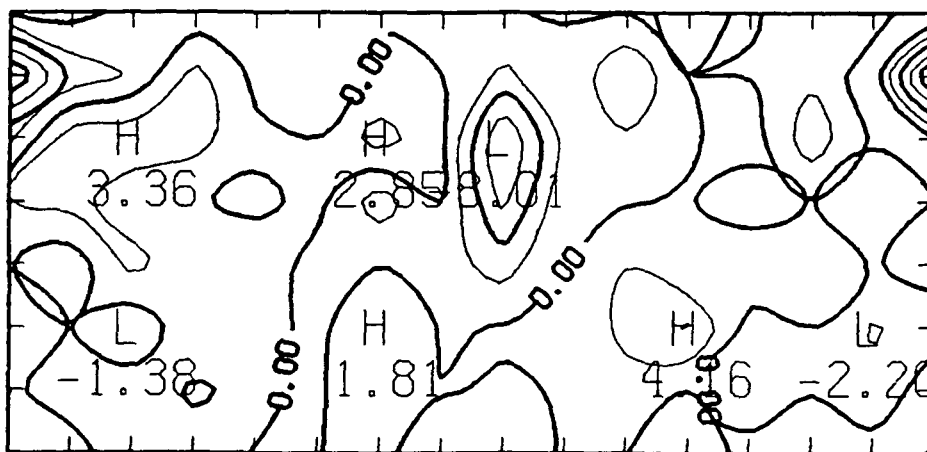
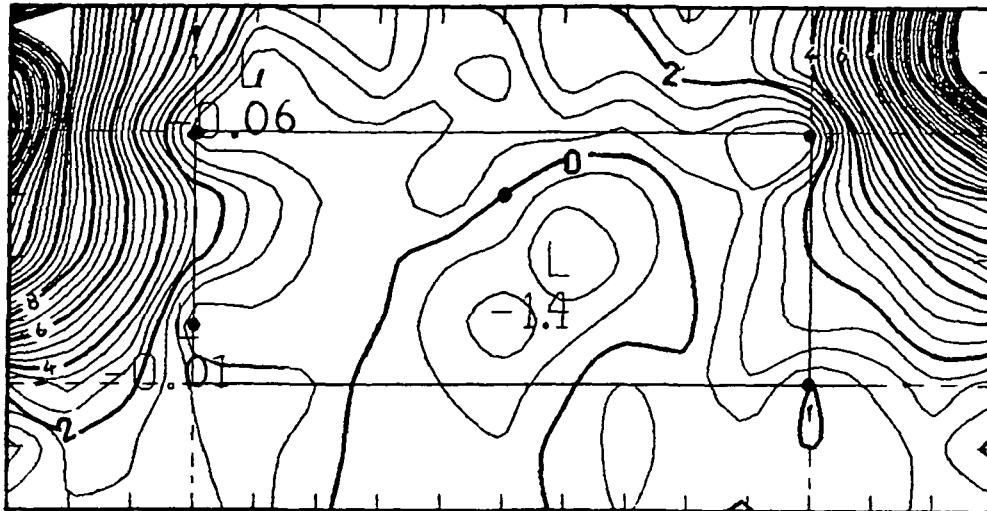


Fig. 26b

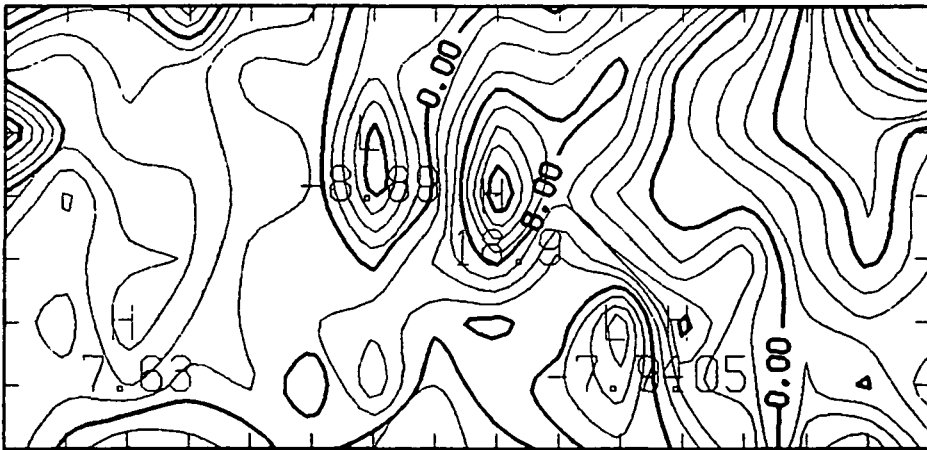
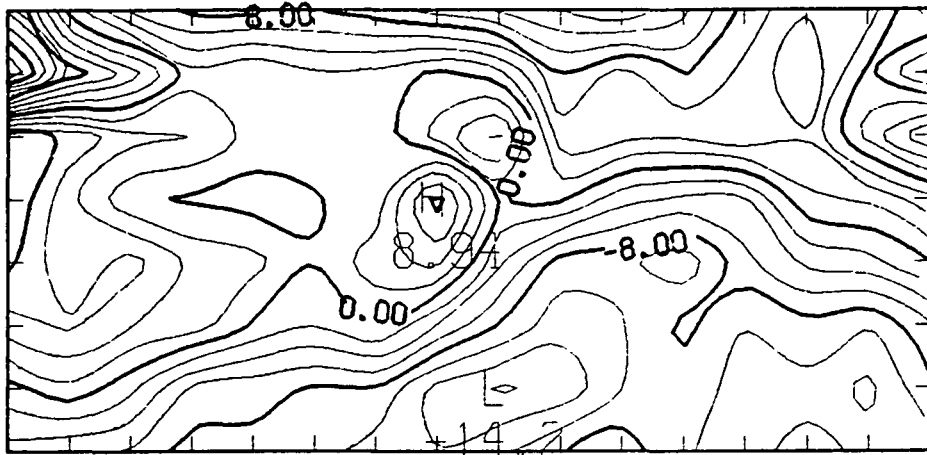
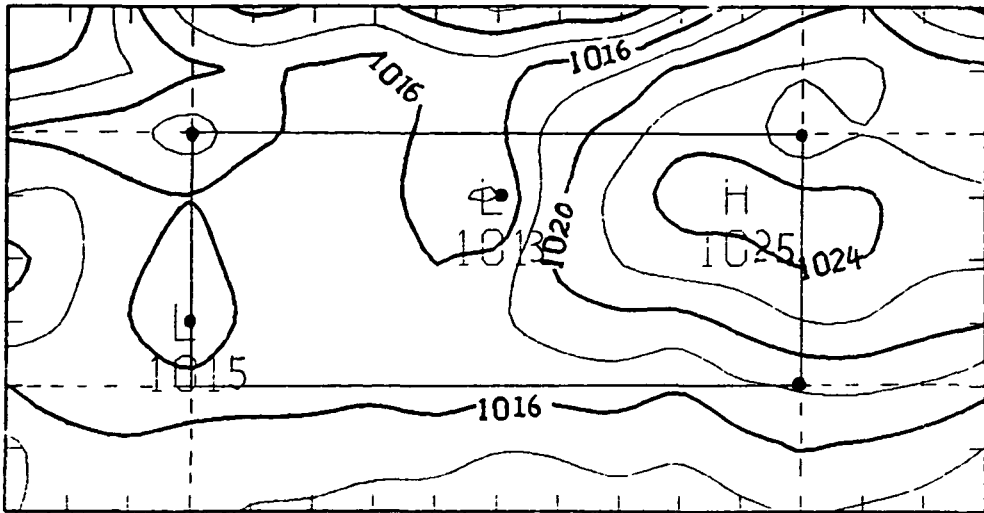


Fig. 27a

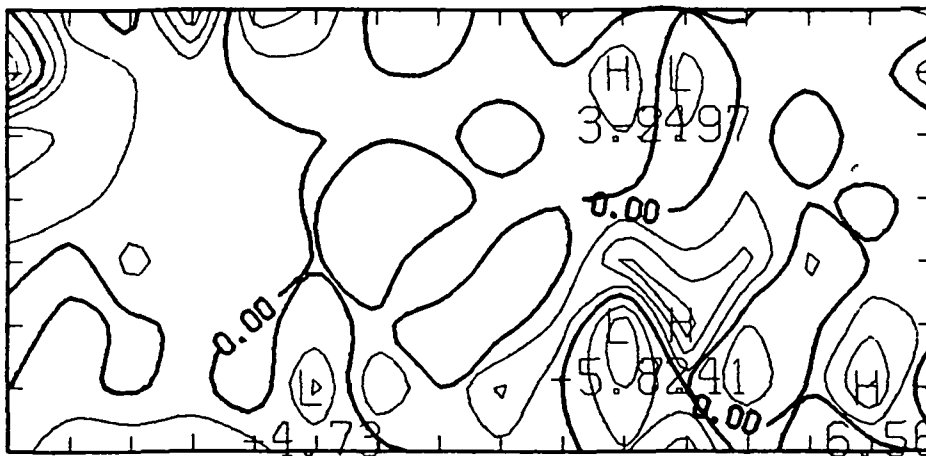
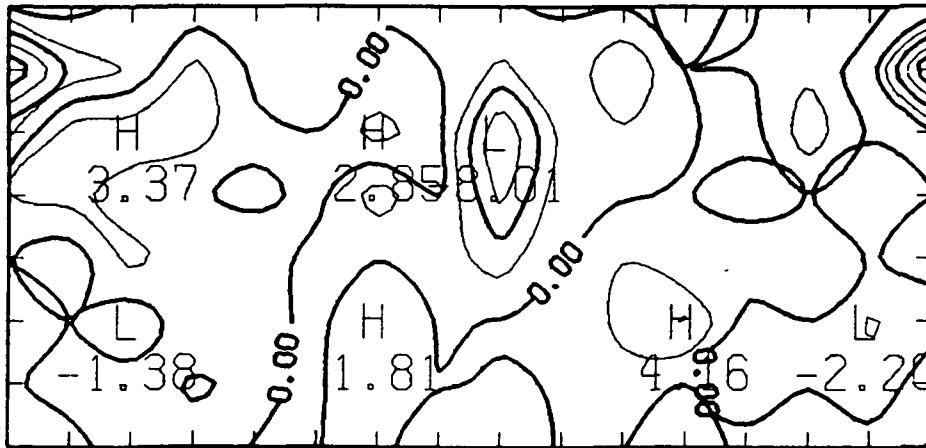
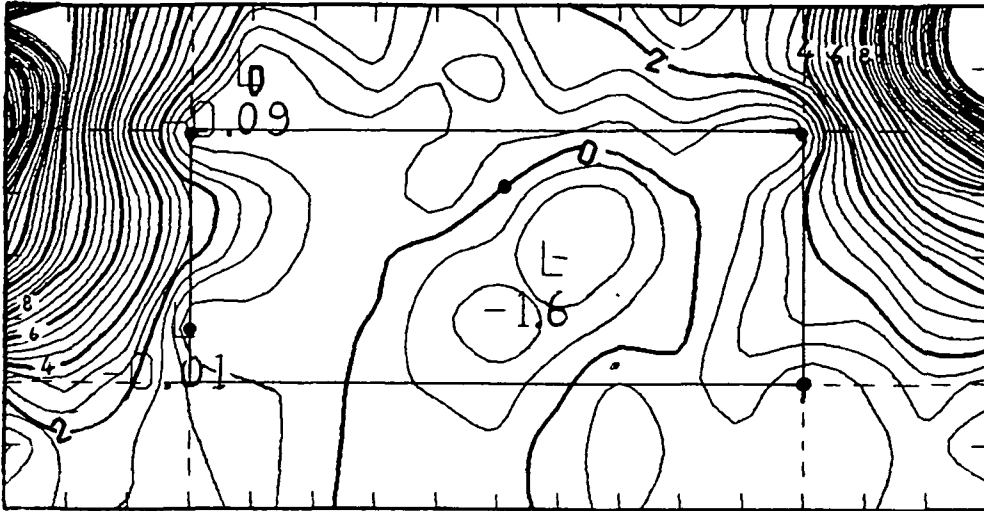


Fig. 27b

REFERENCES

- Blackadar, A.K., and H. Tennekes, 1968: Asymptotic similarity in neutral barotropic atmospheric boundary layers. *J. Atmos. Sci.*, **25**, 1015-1020.
- Brown, R.A., and W.T. Liu, 1982: An operational large-scale marine planetary boundary layer model. *J. Appl. Meteor.*, **21**, 261-269.
- _____, V.J. Cardone, T. Guymer, J. Hawkins, J.E. Overland, W.J. Pierson, S. Peteherych, J.C. Wilkerson, P.M. Woiceshyn, and M. Wurtele, 1982: Surface wind analyses for SEASAT. *J. Geophys. Res.*, **8**, 3355-3364.
- Businger, J.A., et al., 1971: Flux-profile relationships in the atmospheric surface layer. *J. Atmos. Sci.*, **28**, 181-189.
- Dome, G.J., A.K. Fung, and R.K. Moore, 1977: An empirical model for ocean radar backscatter and its application in inversion routine to estimate winds speed and direction effects. Paper presented at Proceedings URSI Commission F., La Baule, France, April 28 to May 6, 1977.
- Garratt, J.R., 1977: Review of drag coefficients over oceans and continents. *Mon. Wea. Rev.*, **105**, 915-929.
- Gray, W.M., 1972: A diagnostic study of the planetary boundary layer over the oceans. Atmos. Sci. Paper No. 179, Colorado State University, 95 pp.
- Jones, W.L., F.J. Wentz, and L.C. Schroeder, 1978: Algorithm for inferring winds stress from SEASAT-A. *AIAA J. Spacecraft Rockets*, **15**, 368-374.
- _____, L.C. Schroeder, D.H. Boggs, E.M. Bracalente, R.A. Brown, G.J. Dome, W.J. Pierson, and F.J. Wentz, 1982: The SEASAT-A satellite scatterometer: The geophysical evaluation of remotely sensed wind vectors over the ocean. *J. Geophys. Res.*, **87**, 3297-3317.
- Moore, R.K., and A.K. Fung, 1979: Radar determination of winds at sea, *Proc. IEEE*, **67**, 1504-1521.
- Pierson, W.J., V.J. Cardone, and J.A. Greenwood, 1974: The applications of SEASAT-A to meteorology. Tech. Report, City University of New York.
- Schroeder, L.C., D.H. Boggs, G. Dome, I.M. Halberstam, W.L. Jones, W.J. Pierson, and F.J. Wentz, 1982: The relationship between wind vector and normalized radar cross section used to derive SEASAT-A satellite scatterometer winds. *J. Geophys. Res.*, **87**, 3318-3336.
- Tennekes, H., 1973: Similarity laws and scale relations in planetary boundary layers. *Workshop on Micrometeorology*, A.M.S., Boston, 177-216.
- Wright, J.W., 1966: Backscattering from capillary waves with application to sea clutter. *IEEE Trans. Antennas Propagat.*, **AP-14**, 749-754.